DOCTORAL THESIS
2015

COMPLEX DYNAMICS IN PHOTONIC DELAY SYSTEMS: A STORY OF CONSISTENCY AND UNPREDICTABILITY

Neus Oliver Andreu

DOCTORAL THESIS
2015

Doctoral Program of Physics

COMPLEX DYNAMICS OF PHOTONIC DELAY SYSTEMS: A STORY OF CONSISTENCY AND UNPREDICTABILITY

Neus Oliver Andreu

Thesis Supervisor: Ingo Fischer

Tutor: Claudio R. Mirasso

Doctor by the Universitat de les Illes Balears

ii

Complex dynamics in photonic delay systems: a story of consistency and unpredictability

Neus Oliver Andreu

Tesis presentada en el Departamento de Física de la Universitat de les Illes Balears

PhD Thesis

Director: Dr. Ingo Fischer

El Profesor Ingo Fischer, Profesor de Investigación del Consejo Superior de Investigaciones Científicas (CSIC) y el Profesor Claudio Mirasso, Catedrático de Universidad (UIB),

HACEN CONSTAR

que esta tesis doctoral ha sido realizada por la Sra. *Neus Oliver Andreu* bajo su dirección en el Instituto de Física Interdisciplinar y Sistemes Complejos (UIB-CSIC) y, para dejar constancia, firma la misma.

Palma, 12 de noviembre de 2015

Ingo Fischer   Claudio Mirasso
Director   Ponente

Neus Oliver Andreu
Doctorando

When you come out of the storm you won't be the same person that walked in. That's what the storm is all about. - Haruki Murakami.

Resumen

El campo de la fotónica está revolucionado nuestra industria y sociedad actuales. Sus usos no se limitan a ciencia avanzada y muchas de sus aplicaciones están integradas en nuestra vida diaria: internet depende de las comunicaciones ópticas por fibra, los láseres son una herramienta más en cirujía médica y fabricación industrial, y el uso de la luz ha facilitado el desarrollo de técnicas de metrología, entre otros.

La fenomenología en fotónica hace de ella un campo lleno de posibilidades y potencial por explorar. Dos de las áreas más prometedoras son el procesamiento de información y comunicaciones ópticas seguras. Contribuyendo a dichas áreas, esta tesis estudia el comportamiento complejo y emergente en un sistema fotónico concreto: el láser de semiconductor con retroalimentación. Este sencillo sistema es capaz de generar gran variedad de regímenes dinámicos, como caos determinista. Con él, abarcamos las propiedades de consistencia para el procesamiento de la información, y la generación de números aleatorios, escribiendo una historia de consistencia e impredecibilidad.

Sobre consistencia o cómo procesar información por medios fotónicos

Nuestro cerebro es un órgano eficiente, capaz de realizar de manera fiable tareas complicadas como el reconocimiento de caras. Inspirándose en el cerebro, se han desarrollado nuevos métodos para imitar el procesamiento de la información en redes neuronales, entre ellos "Reservoir Computing". En esta técnica, un sistema fotónico no lineal es capaz de efectuar tareas computacionalmente arduas al proporcionar respuestas consistentes a señales de entrada.

La capacidad de un sistema de responder de manera similar a estímulos similares, o consistencia, es una cualidad natural que, sorprendentemente, no está asegurada. Su cuantificación y mecanismos causantes son temas por investigar y los láseres de semiconductor con retroalimentación representan una plataforma excelente para ello.

Por medio de tres experimentos investigamos, caracterizamos y cuantificamos las propiedades de consistencia en esquemas ópticos y optoelectrónicos. Los experimentos ilustran transiciones entre respuestas consistentes e inconsistentes, así como su dependencia con respecto al tipo y naturaleza de la señal de entrada. Más allá del mundo de la fotónica, la consistencia es un concepto relevante en ciencia y tecnología. Las propiedades y métodos desarrollados en esta tesis representan un avance para futuras investigaciones y aplicaciones.

Sobre impredecibilidad o cómo implementar un generador de números aleatorios óptico

Los números (bits) aleatorios, son cruciales para transmisión de información segura, juegos online, simulaciones numéricas o criptografía. Su ubicuidad ha provocado la aparición de generadores de números aleatorios (RNGs) basados en componentes fotónicos con claras ventajas: pueden integrarse fácilmente en sistemas de telecomunicaciones actuales y permiten la generación a velocidades altas (Gbit/s). Aunque se han implementado algunos RNGs ópticos exitósamente, quedan cuestiones por resolver: ¿Es posible emplear esquemas más sencillos para generar números aleatorios? ¿Estamos empleando los RNGs de manera óptima? ¿Cuál es el ritmo máximo de generación posible? ¿Podemos conocerlo de antemano? Esta tesis contribuye a responderlas. Proponemos un experimento simple basado en un láser de semiconductor con retroalimentación, aprovechando la impredecibilidad de su dinámica caótica. Sin embargo, la dinámica es condición necesaria pero no suficiente para obtener números aleatorios. En la comprensión de los factores determinantes en la generación de números aleatorios y las altas velocidades de generación reside la relevancia de este trabajo.

Summary

The field of photonics is revolutionizing the current industry and society, analogously to what electronics did during the 20th century. The uses of photonics seem endless and are not restricted to advanced science. Some of its applications have already become mature technologies, and belong now to our everyday life: internet relies on optical fiber communications, lasers are an integrated tool in medical surgery and industrial manufacturing, and the use of light has facilitated the measurement techniques in metrology, among many others.

The rich phenomenology in photonics makes it an emerging field with open perspectives, whose full capabilities are still to be exploited. Specifically, two of the promising areas for photonics are information processing and secure optical communications. Complex phenomena in photonics can serve as a backbone for both applications. This Thesis comprises the study of the emerging complex behavior in a concrete photonic system: a semiconductor laser with delayed feedback. This simple system can generate an interesting variety of dynamical regimes, like deterministic chaos and, therefore, we use it to contribute to the above mentioned areas. More precisely, we address the consistency properties for bio-inspired photonic information processing and the optical generation of random numbers, thereby telling a story of consistency and unpredictability.

On consistency or how to perform reliably photonic information processing

Our brain is a fast and efficient organ, capable of performing reliably tasks that for any computer would be rather hard, such as face recognition. Inspired by our brain, technical systems have been introduced to mimic information processing in neural networks. Understanding how these systems process information can lead to faster, low-energy demanding computing. A recent technique for photonic information processing is Reservoir Computing. In Reservoir Computing, a nonlinear system performs computationally hard tasks, like spoken digit recognition. Its operation is based on providing a consistent nonlinear response with respect to an input signal, exactly as neurons do: they respond reliably to electrical and chemical signals when processing information.

Consistency, as the ability of the system to respond in a similar way to similar inputs, is therefore a key-ingredient to be studied. Surprisingly, consistency in nature is not always a given, and a system might change from a consistent response to an inconsistent one. The mechanisms underlying consistency as well as its quantification are thus pertinent proper questions. Semiconductor lasers with feedback represent again an excellent platform for its investigation.

We approach these aspects by designing three experiments to investigate and characterize the consistency properties of semiconductor laser with delayed optical and opto-electronic feedback. The high quality of the experiments allow us to illustrate the occurrence of transitions between consistent and inconsistent responses in the laser, and characterize their dependence on the drive signal. Thus, we utilize various drive signals, both optical and electrical, and present different ways to quantify consistency, including correlations and a direct measure for the sub-Lyapunov exponent. Beyond photonics, consistency in driven systems is a fundamental and far-reaching concept, present in nature and technology. Therefore, the fundamental properties and the developed method represent valuable findings for further fundamental investigations and applications.

On unpredictability or how to implement an optical random number generator

Random numbers (or random bits) are crucial for information security, online-gaming, complex numerical simulations and cryptography. Their ubiquity has led to the emergence of random number generators (RNGs) based on photonic components, given the intrinsic advantages of photonics: first, an optical RNG is easy to integrate into telecommunication systems; and second, a photonic approach to random number generation allows for high generation speeds of order of gigabits per second (Gbit/s), a key demand of current random number generators. Although some optical approaches to random bit generation had been successfully put forward, open questions still remained: Is it possible to employ simpler schemes to generate random numbers? Are we using the RNG optimally or can its performance be enhanced? What is the maximum bit rate attainable with a given RNG? Can we know it in advance? In this Thesis, we contribute significantly to answer these questions. We propose a strikingly simple experimental setup based on a single semiconductor laser with optical feedback, benefiting from the unpredictability and randomness of the chaotic output of the laser. Nevertheless, chaotic dynamics is only a necessary but not a sufficient condition to obtain random numbers. We present guidelines on the interplay between dynamics, acquisition procedures and post-processing, and predict the potential of any RNG by using Information Theory to estimate the maximum achievable bit rate.

The relevance of this work relies not only on the high speed of the bit rate, up to 160Gbit/s, but also on the understanding of the factors involved in the random bit generation process to guarantee the optimal operation of any laser-based generator.

Acknowledgements

If someone had told me ten years ago that I would be writing these lines today, I wouldn't had believed them. At that time I was convinced that Physics was cool, but not for me. And here I am with a PhD Thesis that has my name on it. Certainly, I could not have done this work without the help and contribution of so many people throughout these years.

I would like to express my deep gratitude to Prof. Ingo Fischer. His patience, support, respect, perseverance, passion towards science and motivation were the constant attributes of his wise guidance. Discussions with him were always a source of inspiration, and despite my atelophobia, he kept encouraging me every time I felt hopeless. From him, I learnt that failure is only part of success and that giving up is never a choice. I feel very lucky to have had as an advisor a person I admire so much, as a scientist and as a human being.

I cannot forget the person responsible of my first steps into research and the first to believe I was capable of pursuing a PhD: Prof. Maxi San Miguel. Thanks for trusting in me. I am also very grateful to Prof. Claudio Mirasso for his advice and for being so supportive and caring during these years. With the doors of his office wide open at any time, he always had encouraging words for me and I can never thank him enough for his kindheartedness.

I would also like to thank all the collaborators and colleagues that I got to meet and from whom I learnt so much: Dr. Miguel C. Soriano for guiding me into the world of experimental photonics, Dr. David Sukow for his kindness, constant support and pleasant emails, Dr. Fan-Yi Lin for his hospitality when I did the research training in Taiwan and Dr. Laurent Larger for welcoming me in his labs and introducing me to the optoelectronic oscillator. I also thank Dr. Daniel Brunner for his willingness to help at any time and always with a smile on his face. I also want to give credit to Dr. Thomas Jüngling. His mentoring, excellent work and, above all, friendship, have meant a lot to me. I also want to thank Dr. Jordi García-Ojalvo, Antonio Pons, Javier Buldú, Maria del Carme Torrent and Jordi Tiana-Alsina.

I am also grateful to each and every person at IFISC, for the inspiring atmosphere they create and the good memories that I will take with me. I am particularly thankful to all the members of the Nonlinear Photonics Lab, specially to my dudes Xavier Porte and Konstantin Hicke. I also want to thank Dr. Pere Colet and Dr. Roberta Zambrini for the nice interactions along these years, and all the current and former students at the S07. I want to express my gratitude to the technical and administrative staff: Marta Ozonas, Inma Carbonell, Rosa María Rodríguez, Rosa Campomar, Rubén Tolosa, Edu Herraiz, Antònia Tugores, Pep Canyelles, Daniel Palou and Edu Solivellas.

As a PhD student I got to meet a lot of amazing colleagues from around the globe. I

am thankful to all the nice people at the National Tsing Hua University in Taiwan, specially Chih-Hao Cheng, Jack Wu and Yi-Huan Liao. To all the scientists I met at FEMTO-ST, particularly to Jacques Chrétien, Bicky A. Márquez, Guoping Lin, Shanti Toenger, Antonio Baylon, Xavier Romain, Tintu Kuriakose, Bogdan Penkovsky and Ignacio Zaldivar. I would also like to mention Dr. Anbang Wang, Dr. Yun-cai Wang and Dr. Alan Shore for the nice time in China.

The best thing about this time as PhD student is to have had colleagues that ended up being real friends. I am happy to have shared so many good times with Marina Diakonova, Antònia Tugores and Thomas Jüngling. Thank you for being by my side and for accepting my craziness with no judgements. I look forward to our next adventures together. I am also deeply grateful to Valérie Moliere, for her tremendous support in my joys and struggles. To my friend Tawnee Hensel, because even though we don't see each other as much as we would like to, we still can count on each other.

Last but not least, I want to thank my parents and my brother. Aunque no seamos la familia más convencional, soy muy feliz de teneros a mi lado. Gracias por apoyarme aún sin saber muy bien qué he estado haciendo. And above all, I want to thank Toni Buades, for being a partner, a friend and a fellow traveler; for his patience, limitless understanding, and for embracing the mess that I am. Thanks for sharing your life with me.

List of Publications

- Neus Oliver, Miguel C. Soriano, David W. Sukow and Ingo Fischer. *Dynamics of a semiconductor laser with polarization-rotated feedback and its utilization for random bit generation.* Optics Letters, **36**, 23, 4632, (2011).

- Neus Oliver, Miguel C. Soriano, David W. Sukow and Ingo Fischer. *Fast random bit generation using a chaotic laser: approaching the information theoretic limit.* Journal of Quantum Electronics, **49**, 11, 910, (2013).

- Neus Oliver, Thomas Jüngling and Ingo Fischer. *Consistency properties of a chaotic semiconductor laser driven by optical feedback.* Physical Review Letters, **114**, 12, 123902, (2015).

Manuscripts in preparation

- Neus Oliver, Javier M. Buldú, Antonio J. Pons, Jordi Tiana-Alsina, M. Carme Torrent, Ingo Fischer and Jordi García-Ojalvo. *Consistency through transient dynamics.* To be submitted, PNAS.

- Neus Oliver, Bicky A. Márquez, Laurent Larger and Ingo Fischer *Forms of consistency in a multistable driven system: the Ikeda oscillator case.*

Conference contributions

- M. C. Soriano, N. Oliver, X. Porte, R. Vicente, I. Fischer and C. R. Mirasso. *Delay Coupled Semiconductor Lasers: Dynamics and Applications.* VII Reunin Iberoamericana de ptica (RIAO). X Encuentro Latinoamericano de ptica, Lseres y Aplicaciones (OPTILAS), Lima, Peru, 2010. **Invited Talk**.

- N. Oliver, M. C. Soriano, D. W. Sukow and I. Fischer. *Dynamics of semiconductor lasers with polarization rotated feedback and its applications for fast random bit generation.* European Conference on Lasers and ElectroOptics (CLEO Europe) and the XIIth European Quantum Electronics Conference, Munich, Germany, 2011. **Talk**.

- N. Oliver, M. C. Soriano, D. W. Sukow and I. Fischer. *Dynamics of semiconductor lasers with delayed polarization rotated feedback and its applications for fast random bit generation.* Combined DPG Spring Meeting, Berlin, Germany, 2012. **Talk**.

- N. Oliver, M. C. Soriano, D. W. Sukow and I. Fischer. *Dynamics of semiconductor lasers with delayed feedback and its applications for fast random bit generation.* International Conference on Delayed Complex Systems (DCS12), Palma de Mallorca, Spain, 2012. **Poster**.

- N. Oliver, M. C. Soriano, D. W. Sukow and I. Fischer. *Experimental Criteria for high-speed random bit generation using a chaotic semiconductor laser.* European Conference on Lasers and Electro-Optics (CLEO Europe) and the XIIIth European Quantum Electronics Conference, Munich, Germany, 2013. **Talk**.

- N. Oliver and I. Fischer. *Exploring chaotic semiconductor lasers for high speed random bit generation: practical and information theoretic limitations.* The 6th International Workshop on Chaos Fractals Theories and Applications, Shanxi, China, 2013. **Invited Keynote**.

- N. Oliver, T. Jüngling, D. Brunner, A. J. Pons, J. Tiana-Alsina, J. Buldú, M. C. Torrent, J. García-Ojalvo and I. Fischer. *Consistency Properties of a Chaotic Laser to Input Pulse Trains.* European Conference on Lasers and Electro-Optics and the European Quantum Electronics Conference, Munich, Germany, 2015. **Poster**.

Contents

Introduction

> It doesn't matter how beautiful
> your theory is, it doesn't matter
> how smart you are. If it doesn't
> agree with experiment, it's
> wrong.
>
> ___
>
> Richard P. Feynman, Physicist.

In this Thesis, and as its title suggests, the complex dynamics originating from photonic delay systems is explored, putting special emphasis on two emerging properties: consistency and unpredictability.

Semiconductor lasers with delayed feedback are employed to exemplify how a nonlinear system can display these two features. The property of consistency describes the ability of a system to produce complex but still reproducible dynamics in response to a repeated input. This definition already reveals the necessity of a drive-response scheme, in which the laser with delayed feedback acts as the response system. A consistent behavior, when similar drive signals lead to similar outputs, can thus be seen as predictable. Nevertheless, semiconductor laser systems with delay are known to exhibit complex phenomena such as deterministic chaos, with randomness-like features that makes the dynamics unpredictable. These two opposed properties, consistency and unpredictability, can be achieved with robustness in such systems by just tuning the laser parameters, and their controllability enriches even more the variety of current applications of photonic delay systems. Consistency is of key importance for the understanding and harnessing of any implementation of information processing, while unpredictability is the foundation for any cryptographic application.

Consistency is investigated through the analysis of the responses from three different laser systems with delay subjected to a drive. The transitions between inconsistent and consistent behavior as a function of parameters is illustrated, and different methods to evaluate the degree of consistency are introduced. The property of unpredictability is also studied by means of a semiconductor laser with delayed feedback, only that here, no input signals are used. Tailoring the optimum conditions, we exploit the unpredictability of the system for the application of random bit generation.

In this introductory Chapter, the basics for the understanding of the Thesis are reviewed, introducing delay systems and emphasizing the role of photonic systems for the investigation of complex dynamics. The concept of consistency in nonlinear delay systems is explained together with the property of unpredictability resulting from the chaotic dynamics, and relate it to the application of random bit generation. In this way, the reader will be prepared for the following chapters and the results they contain. The mathematical methods to quantify consistency and unpredictability can be found in Chapter 2.

1.1
Delay systems

The presence of delay in dynamical processes in real life is undeniable [1]. Time delays are, in our reaction times, determined by the time our brain requires to process information and send an order to our muscles [2]. Examples abound, such as in traffic dynamics, where cars are followed by other cars and drivers have to adjust their speeds accordingly [3], or in heating systems where one needs to set a given water temperature [4], and even in more sophisticated structures like the airport networks where delays are propagating around the globe [5].

The appearance of a delay time in a simple dynamical system often results in a completely new phenomenology. It has been shown that delay induces instabilities that can alter the dynamical behavior by exhibiting oscillations or even chaos [1]. These delay-induced instabilities can be considered an inconvenience to be avoided in engineering applications. Nevertheless, delay is something of a double-edged sword. There are situations in which the delay plays a stabilizing role and can be used to non-invasively control unstable states [6, 7]. Such interesting aspects of delay systems stimulated the study of the induced phenomena in physical systems which benefited from the cross-fertilization between theory and experiments, and the possibility to use the gained knowledge in novel applications.

From a mathematical point of view, systems with discrete delay are described by delay differential equations of the form:

$$\dot{\mathbf{x}}(t) = F(\mathbf{x}(t), \mathbf{x}(t - \tau)) \qquad \mathbf{x}(t) \in \Re^N. \tag{1.1}$$

Where x is the state of the system given by its N degrees of freedom, F is any linear or nonlinear function, and $\tau > 0$ is the delay time. The appearance of a delayed term in a differential equation leads to drastic changes in the analysis. This is due to fact that the solution is no longer uniquely defined by a single initial condition but, at any time t_0, the solution profile of the variables within the interval $[t_0\text{-}\tau, t_0]$ is needed to define the state of the system. This implies that the initial condition is the equivalent to a vector in phase space, and that the phase space becomes formally infinite dimensional, allowing the existence of attractors with high dimensions. Nevertheless, the dimensionality of the delay dynamics remains finite in practice.

1.2

Photonic delay systems

Despite the ubiquity of delay systems, a large contribution to the study of delay dynamics have been made through semiconductor laser systems. The versatility, compactness and robustness of their performance made semiconductor lasers ideal test-beds for the study of nonlinear dynamics, and in particular, good representatives for the study of delay systems. Since the invention of semiconductor lasers in 1962 [8, 9, 10], their use has been expanding to endless applications and technological advances, making the research in the field of photonics a continuing emerging area with a substantial economic impact. Semiconductor lasers are characterized by a strong sensitivity to delayed feedback or delayed coupling, meaning that, even when a tiny fraction of light reenters into the cavity of the laser, the emission properties are significantly perturbed [11, 12, 13, 14]. The feedback induced instabilities result in the emergence of complex dynamical scenarios, far from the stable steady emission expected from a laser. Such complex dynamics have been investigated extensively [15, 16, 17, 18]. Nevertheless, the original motivation for its study was to get rid of most of the delay-induced dynamics, since their presence implies the degradation of the performance in real-world applications like the CD/DVD players or in telecom modules. It was in the early 1990s that their advantageous attributes started to be recognized, mainly in the field of chaos applications [17, 19]. With the fast time scales of the chaotic oscillations over frequencies of gigahertz, the instabilities in semiconductor lasers turned out to be an important attribute for modern chaos communications [20] or chaos encryption [21, 22], but also as low-coherence sources for rainbow refractometry [23], remote position sensors, lidars [24], random bit generators [25] or information processing [26], among many others.

It is worth mentioning that complex dynamics is here understood as all nonlinear dynamical phenomena emerging from the delayed feedback [27, 28, 29, 30, 31]. Periodic oscillations [32, 33] and period-doubling [34, 35], quasi-periodicity [36], deterministic chaos [37, 38, 39, 40, 41, 42, 43, 44, 45, 46], multistability [38], bifurcation cascades [47, 48, 49], intermittency [50], and chaos synchronization [51, 52, 53] are some of the nonlinear behaviors observed in photonic delay systems.

1.2.1 Photonic delay systems in the drive-response scheme

Semiconductor lasers are not only sensitive to their own delayed feedback but the addition of an external driving signal to the laser also perturbs the emission properties. Photonic delay systems represent a good platform for the investigation of drive-response schemes. In such schemes, the drive system generates an output signal that is sent to the response system, which in this case is a system with delay (see Fig. 1.1 (a)). Then, the reactions of the response system to the drive are analyzed. The drive is usually a direct parametric modulation of the laser pump current, but more elaborated drives can be utilized. A delay system can also act as a drive when its output is injected into a response system (which can be a delay system or not), as illustrated in Fig. 1.1 (b). One could even think of a single laser with delay feedback

as self response system, where the output signal x(t) is the response to the drive x(t-τ) like in Fig. 1.1 (c). In a more elaborated setup, a single delay system with multiple feedback loops could serve as a drive and response system at the same time (see Fig. 1.1 (d))). While the use of an external driving signal restricts the origin of the drive to electrical scalar recorded waveforms, the possibility to use photonic delay systems also as drives (Fig. 1.1 (b), Fig. 1.1(c) and 1.1(d)) permits the utilization of complex continuous vector-state optical drives. Along this Thesis, different schemes of drive-response systems are used.

The drive-response configuration represents a prominent base for the investigation of a crucial property of nonlinear systems: consistency.
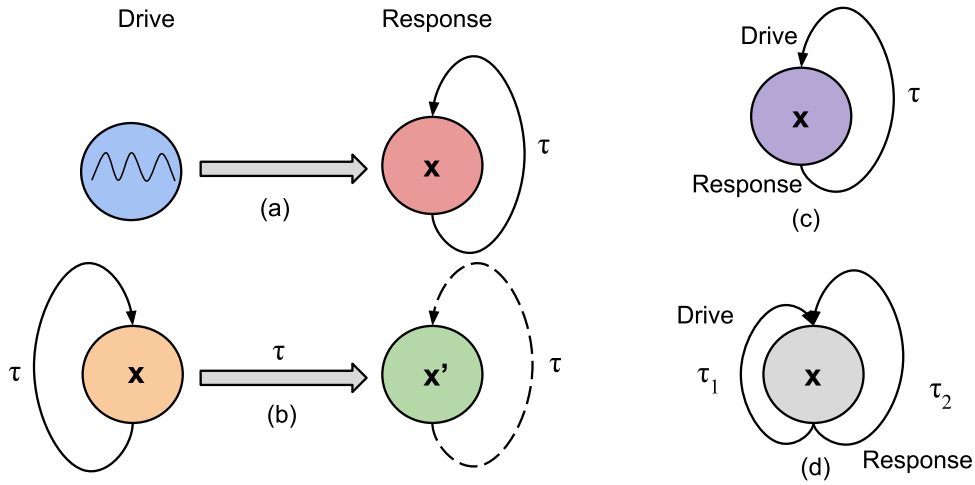
Figure 1.1: Illustration of four possible schemes employed for the investigation of drive-response systems. The delay system is used as response system. (a) Any arbitrary signal can be used as a drive. (b) The output of a delay system serves as the drive of a response system, which can be a delay system or not. (c) A single laser as self response system. (d) A delay system with two feedback loops.

1.3
About Consistency

In real life applications, it is an obvious requirement to have a reliable operation of a given system. This means assuring the same (or very similar) performance of the system when tested repeatedly. In nonlinear dynamical systems, we call this property consistency. Consistency is defined as the ability of a nonlinear system to respond in a similar manner to similar inputs [19]. This definition can be easily interpreted in terms of drive-response schemes, so that similar drives lead to similar responses, without imposing any restriction on the types of drive signals used. The nature of the drive signals can be optical or electrical, and their

origin can come from real recorded time traces of the system, from noise, from artificially generated waveforms with an Arbitrary Waveform Generator, or any other source. Consistency is, therefore, a non-trivial property of the response system that depends on the drive. For a certain input, a system might provide a consistent response, whereas the same system can exhibit inconsistent behavior for another drive. This is illustrated in Figure 1.2.
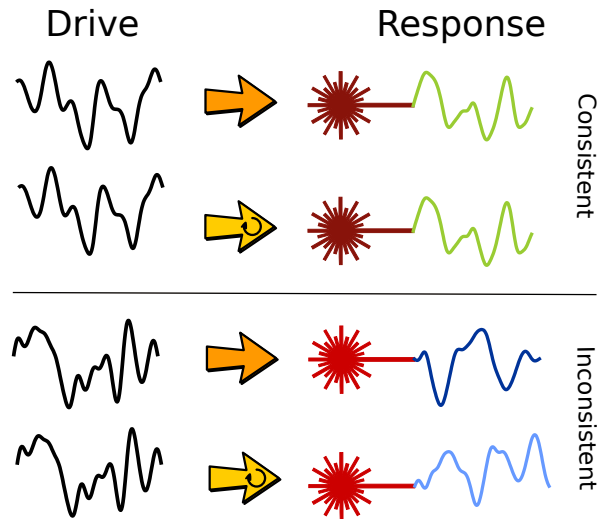
Figure 1.2: Illustration of the concept of consistency. The same system can exhibit consistent or inconsistent responses depending on the drive. When repetitions of the same drive lead to a similar response, there is a consistent behavior of the system. But if repetitions of a drive signal lead to significantly different responses, the system is inconsistent.

The boundaries between consistent and inconsistent behavior are not well defined, and the responses of a dynamical system can be classified into a certain degree of consistency. Responses that are structurally similar but not identical can still be considered consistent. But in a more restrictive scenario, we can distinguish *complete* consistency as the case in which the same input leads to the exact same output of the system. Consistency has also been referred to as reliability and often investigated under the terms of generalized synchronization or noise synchronization [54]. In Chapter 2, the concept of consistency with the notion of generalized synchronization is discussed.

1.3.1 Applications of consistency

There is a clear connection between consistency and the analysis of brain dynamics. The brain, although a complex system, exhibits various degrees of consistency in the neuronal functionality in response to repetitions of input signals and stimuli [55]. This phenomenon has commonly been referred under the term reliability. Consistency also partakes in the formation of spatio-temporal patterns in motor learning [56]. The investigation of the fun-

damental mechanisms behind the achievement of consistency can be useful to understand brain dynamics and the process of learning in the brain. Neuronal systems and photonic delay systems share some common phenomena that make the latter good candidates for such investigations. Both systems can exhibit zero-lag synchronization despite their delays in propagation, and the topology of the configuration is also crucial in both systems for the achievement of synchronization dynamics. The many similarities between the dynamical properties of neuronal networks and photonic delay systems have also led to the development of a bio-inspired information processing concept, the so called Reservoir Computing, whose performance strongly depends on the consistency properties."

In Reservoir Computing, a nonlinear delay system has been proposed and demonstrated successful for the performance of complex tasks such as speech recognition [26, 57]. The method uses the scheme of drive-response system, and a consistent (or reliable) response output with respect to a drive signal is required for the successful implementation of this machine-learning tasks. However, the uses of consistency surpass the processing of information.

Consistency is a concept that shows up in many other fields where the scheme drive-response is present. The success of many practical applications relies on the reproducibility of the dynamical behavior to guarantee the robustness of the system. In biology, the response of biomolecules to external inputs can be tested and used to identify severe changes in the system. In engineering, a consistent behavior is a basic requirement for the development of new materials when assessing their mechanical properties. It is also essential in cryptography for the generation of secure tokens, where the drive-response relation must be complex and at, the same time, reproducible [19].

So far, we have introduced the property of consistency in nonlinear systems. A semiconductor laser system with delay can display a complex yet reproducible behavior and, thus, predictable. Interestingly, and as explained in the next section, the same system can also act as a source of unpredictable dynamics, broadening the uses of photonic delay systems.

1.4

About Unpredictability

Among the different dynamics generated by photonic delay systems, deterministic chaos is one of the most prominent and investigated behaviors. Chaos is a phenomenon characterized by irregular oscillations in a nonlinear system with a strong dependence on initial conditions [58]. This means that any two trajectories that start close to each other will separate exponentially with time, Figure 1.3. Nevertheless, chaos is deterministic which means that, if the initial conditions are known with infinite precision, the irregular behavior can be reproduced. Knowing the initial conditions without error is an inherently unrealistic abstraction in continuous dynamical systems but, still, chaos should not be taken as a synonym for randomness or stochasticity.
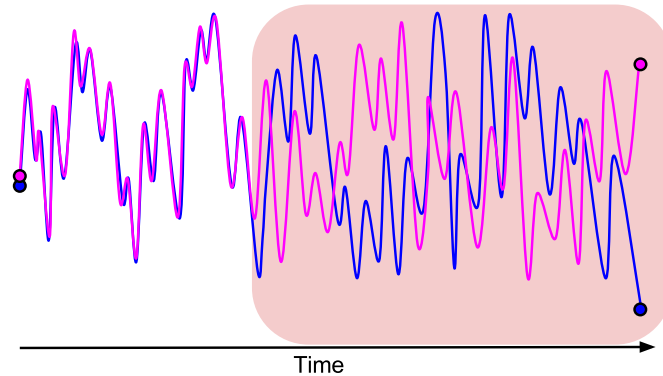
Figure 1.3: Sensitivity to initial conditions: two trajectories that begin close to each other separate exponentially with time.

In practice, the distinction between a random and a chaotic process from experimental data can be a hard task to achieve. Often, the methods rely on tracking the evolution of two nearby trajectories but the identification of close states in high dimensional systems demands big amounts of data and computations.

In photonic systems, semiconductor lasers with time delayed feedback produce fast dynamical instabilities that can lead to deterministic chaos. Semiconductor lasers with delayed feedback, as real chaotic systems, also exhibit a stochastic contribution in their dynamics. Noise additions from the spontaneous noise emission of the laser, and also from the experimental devices that form the setup, are unavoidable. The noise is amplified due to the inherent nonlinearity of the system giving rise to random-like dynamics. Therefore, it is the actual interplay of chaos and noise that makes these systems an outstanding implement for unpredictable behavior.

1.4.1 Applications of unpredictable dynamics

In a world in which digital technologies are established in our everyday lifes, the demands for security in network communications and data transmission have led to the development of new encryption protocols. The use of the chaotic dynamics of semiconductor lasers represents a good approach, given the possibility to operate at high speeds and their easy implementation in current optical communication channels.

One current application that benefits from the combination of chaotic dynamics with inherent noise is random bit generation [25]. The chaotic output of a semiconductor laser is sampled with a fast oscilloscope, converted into a stream of binary numbers and post-processed, resulting in random bits that can pass sophisticated tests of randomness. We elaborate on this application in Chapter 6, in which a practical implementation of a fast random bit generator based on a laser with polarization rotated feedback is demonstrated.

Another important application is chaotic secure communications based on chaos synchronization between two nonlinear systems [22, 59, 60]. Two independent chaotic laser systems

exhibit different autonomous dynamics due to the uncertainty in their initial conditions. However, the two systems can synchronize when coupled, that is, when a small portion of the chaotic output from one system is injected in to the other. This principle serves as the key for chaotic encryption and decryption of messages and secure exchange of a private key through a public channel [61, 62].

Other uses of chaotic lasers in optical sensing include the correlation or chaotic radar (CRADAR) based on chaotic pulse trains with high pulse repetition frequencies that allow for high precision range measurements [63, 64]. In the field of computing, optical logic gates have been implemented via the synchronization properties of two chaotic lasers [65]. These applications are only a few examples of the possibilities of chaotic photonic systems. New exciting developments of chaotic dynamics in semiconductor lasers are yet to come.

1.5
Overview of this Thesis

The work in this Thesis is devoted to the study of photonic delay systems as a source of a great variety of complex dynamics that can ensure reliable behavior as well as unpredictability. The property of consistency is investigated from a fundamental point of view with the characterization of the responses from different laser systems and driving sources. The unpredictability property is exploited in the cryptographic application of random bit generation.

- In Chapter 2, we present the methods and tools used to quantify consistency and unpredictability, and discuss the relation between consistency and generalized synchronization.

- In Chapter 3, we investigate the consistency properties of a semiconductor laser system to its own time-delayed signal. A scheme with two different feedback loops is utilized to store a copy of the dynamical features with high precision and inject it at a later time. The consistency is quantified in terms of correlations and, for the first time in experiments, with a measure proportional to the sub-Lyapunov exponent, the σ value.

- In Chapter 4, a laser with delayed feedback, operating in the regime of Low Frequency Fluctuations, is employed for the characterization of consistency to an external drive in the form of short pulses. The feasibility of induced intensity dropouts in the dynamics is analyzed with different pulse distributions. The inter- and intra-correlations are calculated to demonstrate the role of the drive pattern.

- Chapter 5 covers the use of an opto-electronic intensity oscillator to explore its consistent behavior when different external drives are applied. As a scalar system with multistability, new dynamical features emerge under the influence of a drive. Harmonic signals, pseudo-random pulses and time-traces originating from the system are used as modulation. The correlations indicate a significant level of consistency even in a global chaos regime.

- Chapter 6 focuses on the exploration of unpredictable dynamics from a laser system to the application of random bit generation. Optimum operating conditions are identified, and guidelines on the interplay between dynamics, acquisition process and postprocessing procedures are discussed to guarantee the randomness of the bits.

- The last Chapter of this Thesis includes a summary of the achievements, and an outlook and perspectives for future work.

CHAPTER 2

Concepts and tools

It is a recurring experience of scientific progress that what was yesterday an object of study, of interest in its own right, becomes today something to be taken for granted, something understood and reliable, something known and familiar − a tool for further research and discovery.

J. Robert Oppenheimer,
Physicist

This Chapter covers the mathematical tools employed to quantify consistency and unpredictability throughout the Thesis. Regarding the concepts, a discussion on the equivalence between consistency and generalized synchronization, two closely related terms, is also included. To measure consistency, we introduce the sub-Lyapunov exponent, used in Chapter 3, and the inter- and intra-correlations, employed in Chapters 4 and 5. These two quantities provide different and valuable information about the responses of a driven system. In the last section, we review the well-established tools available to quantify unpredictability, like entropy or autocorrelation function, and we discuss other indicators of the randomness of a time series.

2.1
Consistency and Generalized Synchronization

Consistency is often put in context with generalized synchronization [66, 67, 68]. It should be noted that differences between the interpretations of consistency and generalized synchronization need to be taken into account, and the two terms cannot be utilized synonymously. Generalized synchronization in driven systems is understood as the existence of a functional relationship between the state of the driven system y with another dynamical system x that
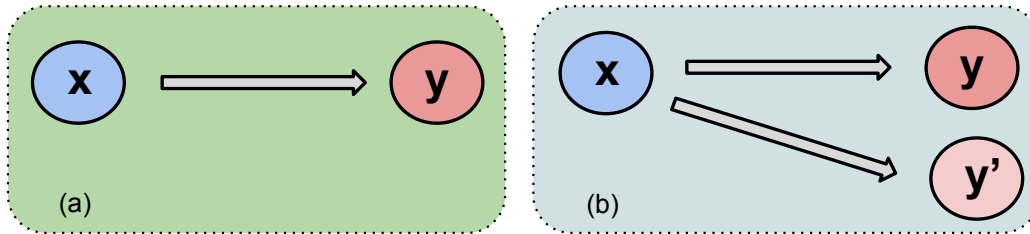
acts as the arbitrary drive (Fig. 2.1 (a)).

Figure 2.1: (a) Drive-response scheme for generalized synchronization. (b) Scheme for the extended generalized synchronization with a replica system y'.

Consistency and generalized synchronization already present a major dissimilarity in the point of view: generalized synchronization describes a property of the relationship between coupled systems while consistency is a property of the response system. The fact that the definition of consistency is based on the "similarity" of the responses makes it a difficult concept to be described and quantified mathematically. Whereas consistency implies a broad set of possible outcomes, ranging from inconsistent to complete consistent responses, generalized synchronization only contemplates a subset of consistency: complete consistency. In the drive-response scheme like the one depicted in 2.1 (a), complete consistency and generalized synchronization are indeed equivalent. If the drive and response systems are in a state of generalized synchronization, in which stability is implied, the responses to the drive will have complete consistency and viceversa. Nevertheless, if the responses are not completely consistent, but have a high degree of consistency, the system will not exhibit generalized synchronization. This could be the case, for instance, when the responses are not identical but are still narrowly bounded.

If we extend the concept of generalized synchronization, as in the Abarbanel test [67], we can denote as extended generalized synchronization the situation in which a copy of the system y' subject to an arbitrary drive x receives the same input and, thus, exhibits complete synchronization with the original y, as depicted in Fig. 2.1 (b). With this scheme, the replica system y' serves to test the repetition of the input x. Again, the three properties (generalized synchronization between x and y, complete synchronization between y and y', and complete consistency of y) would be equivalent. However, as soon as we leave the unidirectional scheme $x \Rightarrow y$ to other arbitrary schemes, the equivalence between properties becomes non-trivial. For example, a mutually coupled scheme $x \Leftrightarrow y$ can already alter the possible outcomes. The functional relationship between the states of drive and response may be undefined, but x and y may still be consistent when the replicas are attached, and viceversa.

To summarize, the extended generalized synchronization is equivalent to complete consistency as a local property of a driven system, no matter the origin of the drive. When the scheme is not a unidirectional drive-response setup, the equivalence between the two concepts

does not apply anymore, and the presence of a generalized synchronization manifold does not imply consistency.

Tools to measure consistency

There are different ways to measure consistency that take into account the type of drive. Here, we introduce two different tools to quantify the degree of consistency. One is based on the calculation of the sub-Lyapunov exponent, and the other is based on the calculation of correlations. The sub-Lyapunov exponent characterizes the response of a driven system in terms of stability and requires the access to the error between the two response signals. The sensitiveness to mismatches between the two responses makes this method more oriented to non-scalar high optical bandwidth drives that can be repeated with high accuracy. The calculation of the correlation coefficient between responses is a practical method that can directly quantify the level of consistency. Their fast computation times and the possibility to use them to identify patterns in the responses makes it more suited for external scalar drive signals that are reinjected multiple times.

2.2.1 The sub-Lyapunov exponent

In dynamical systems, and particularly in chaotic systems, the sensitivity to the initial conditions is often described by the Lyapunov exponent λ, which measures the mean rate of the separation between two nearby trajectories. For a given dynamical system with a state vector $\mathbf{x}(t)$ evolving like in Eq. 2.1:

$$\dot{\mathbf{x}}(t) = f(\mathbf{x}(t)) \qquad \mathbf{x}(t) \in \Re^d \tag{2.1}$$

we can linearize the temporal evolution of a small separation (or perturbation) $\delta\mathbf{x}(t)$:

$$\dot{\delta\mathbf{x}}(t) = Df(\mathbf{x}(t)) \cdot \delta\mathbf{x}(t) \tag{2.2}$$

so that for a given trajectory $\mathbf{x}(t)$, the maximal Lyapunov exponent is defined by:

$$\lambda = \lim_{t \to \infty} \frac{1}{t} \ln\{\frac{||\delta\mathbf{x}(t)||}{||\delta\mathbf{x}(t_0)||}\}. \tag{2.3}$$

There is a whole spectrum of Lyapunov exponents, which in the case of an autonomous system, equals the dimensionality of the phase space (or in other words, same number of Lyapunov exponents as system variables). In delay systems though, the spectrum of Lyapunov exponents is formally infinite. However, we focus on the maximum Lyapunov exponent,

which gives a notion of the predictability of the system and connects the local stability with the global dynamics. A positive maximal Lyapunov exponent indicates chaotic dynamics. A negative maximal Lyapunov exponent is associated with a steady state dynamics, and a $\lambda=0$ could indicate a periodic or quasi periodic orbit in phase space.

The Lyapunov exponents are a property of the system, which allow for other derived measures like the Kolmogorov-Sinai entropy or the Kaplan-Yorke dimension, related to the complexity and dimensionality of the system.

Pecora and Carroll [51] introduced the concept of the sub-Lyapunov exponent as a property of a subsystem belonging to a chaotic system. To investigate the synchronization properties of chaotic coupled systems, they considered an autonomous system with phase space vector $\mathbf{u}$ and divided it into two subsystems $\mathbf{v}$, $\mathbf{w}$. The subsystems obey the equations of motion:

$$\begin{aligned} \dot{\mathbf{v}}(t) &= g(\mathbf{v}(t), \mathbf{w}(t)) \\ \dot{\mathbf{w}}(t) &= h(\mathbf{v}(t), \mathbf{w}(t)) \end{aligned} \tag{2.4}$$

They observed that, under certain conditions, a copy of $\mathbf{w}$, $\mathbf{w}'$, can be made to synchronize with the original $\mathbf{w}$ if both receive the same signal. To prove it, they followed a similar approach, linearizing with respect to $\mathbf{w}$ and writing the equations for a small perturbation of the synchronized state $\xi(t)$:

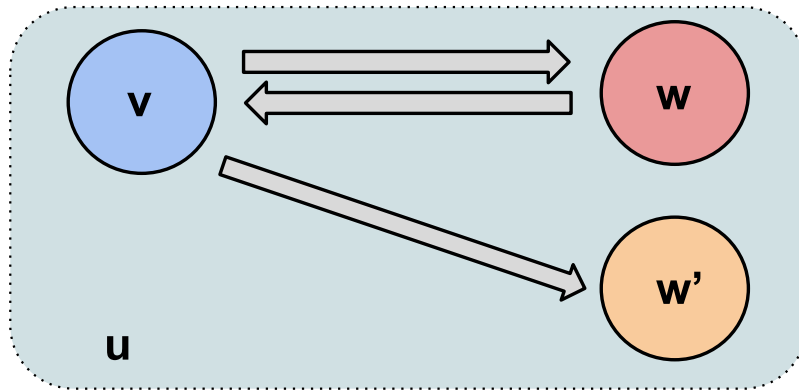Figure 2.2: An autonomous system $\mathbf{u}$ is divided into two subsystems $\mathbf{u} = \mathbf{u}, \mathbf{w}$ and a copy $\mathbf{w}'$ is created to test the synchronization properties.

$$\dot{\xi}(t) = D_w h(\mathbf{v}(t), \mathbf{w}(t)) \cdot \xi(t). \tag{2.5}$$

From this equation, the maximal Lyapunov exponent of the subsystem can be obtained, also known as sub-Lyapunov exponent λ_0:

$$\lambda_0 = \lim_{t \to \infty} \frac{1}{t} \ln\{\frac{||\xi(t)||}{||\xi(t_0)||}\}. \tag{2.6}$$

When λ_0 is negative, there is complete synchronization between $\mathbf{w}$ and $\mathbf{w}'$. There are as many sub-Lyapunov exponents as dimensions of the subsystem $\mathbf{w}$. One can identify this system as a drive-response scheme, in which an autonomous subsystem acts as the drive of another subsystem, the driven system. For the latter, the maximal sub-Lyapunov exponent can be defined, and measures the convergence of the response states to a function of the drive.

In this Thesis, all the schemes investigated are delay systems, with a temporal evolution given by Equation 1.1. The sub-Lyapunov exponent of delay laser systems quantifies the consistency with respect to small perturbations in the response of a semiconductor laser subject to its own time delayed feedback. The sign of the sub-Lyapunov exponent determines whether the laser behaves in the same way when the external input is repeatedly applied, so that a negative λ_0 would indicate an exponential decay rate of the small perturbation to the consistent state.

The sub-Lyapunov exponent has been linked to the concept of strong and weak chaos. These two terms refer to two different types of chaos identified in networks of time-continuous systems with time-delayed couplings. Thus, delay instabilities can be categorized depending on the scaling properties of the maximal Lyapunov exponent [69, 70]. In the large delay times, the maximal Lyapunov exponent converges to a nonzero value in the presence of strong chaos but, in the case of weak chaos, the maximal Lyapunov exponent scales with the inverse delay time. From the point of view of delay systems in the drive-response scheme, the sub-Lyapunov exponent represents a direct measurement of the type of chaos. A positive syb-Lyapunov exponent indicates strong chaos dynamics, while a negative sub-Lyapunov exponent implies weak chaos. For synchronization purposes, it has been shown that only networks with weak chaos can synchronize to a chaotic signal. The sub-Lyapunov exponent is also defined outside delay coupled networks, which then emerge as a special case of drive-response systems if the delay couplings are considered as drives for the individual nodes. Using the extended notion of the sub-Lyapunov exponent, an analogue to weak chaos can be identified with the complete consistent response, and strong chaos with a non-completely consistent response. Jüngling [71] developed an algorithm to extract the value of the sub-Lyapunov exponent from stationary chaotic time series of a delay system. In Chapter 3, a method to measure a quantity proportional to the sub-Lyapunov exponent, σ, is explained in detail.

2.2.2 Inter- and intra-correlations

Complementary to the widely used correlation coefficients, in the cases where an external modulation is repeatedly injected to the system, we use the so-called inter-correlation and
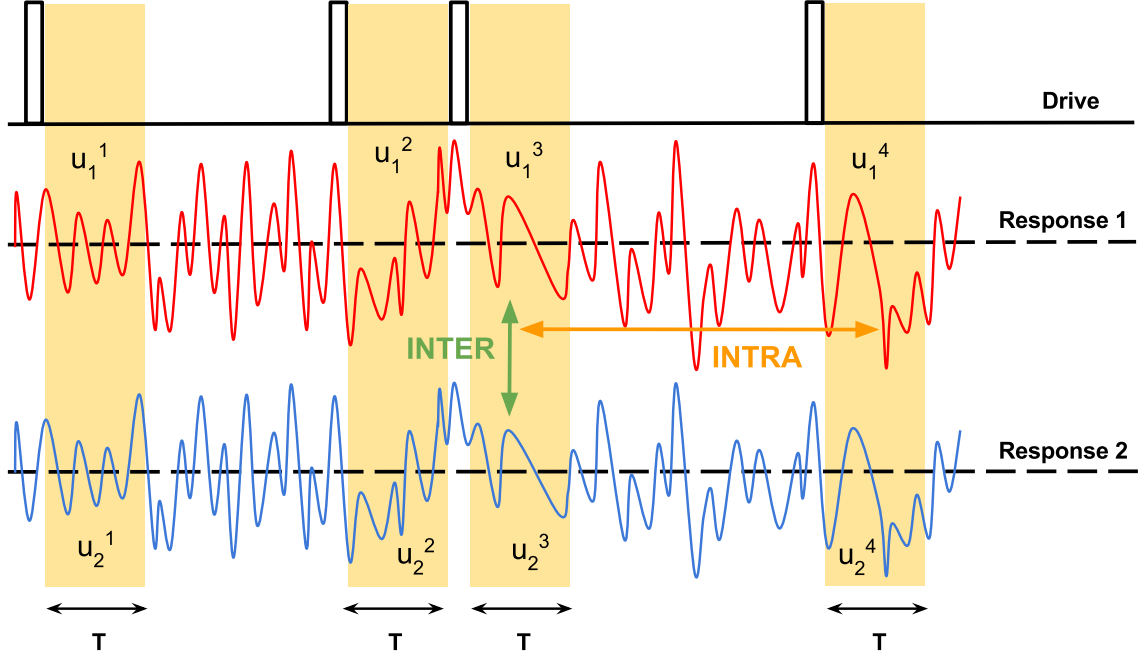
Figure 2.3: Illustration of the concepts of inter- and intra-correlations. Two trajectories are depicted in response to a pulsed drive. 4 responses $u_i^j(t)$ of duration T are compared within the same time trace (intra-correlation) and among the two repetitions (inter-correlation).

intra-correlation measures. The input drive can be an harmonic function, a random distribution of pulses or even a noisy signal, with or without periodicity. The intra-correlation compares the response trajectories of the system along the same input drive, whereas the inter-correlation compares the responses across multiple repetitions of the same input drive. These two types of correlations, developed by Jordi García-Ojalvo and Javier Buldú, are illustrated in Figure 2.3.

Let the drive be a sequence of N pulses or an harmonic function of N periods, and M the number of time traces corresponding to the repetitions of the modulation sequence. We denote the response of the system to a given pulse or period as $u_i^j(t)$ with $t \in [0, T]$. Here, i indicates the repetition of the sequence, so that $i \in [1, M]$, and $j \in [1, N]$ defines the index of the pulse or period along the sequence, so that NT is equivalent to the total duration of the sequence. The duration of the responses T coincides with the period of the modulation or the minimum spacing between pulses.

To compute the correlations, we altered the original expression of the pairwise-based Pearson coefficient. For two given responses, u_i^j and u_k^l, the Pearson coefficient would be

calculated as:

$$C_{u_i^j, u_k^l} = \frac{\langle (u_i^j - \mu_{u_i^j})(u_k^l - \mu_{u_k^l}) \rangle}{\sigma_{u_i^j} \sigma_{u_k^l}} \tag{2.7}$$

The new expression uses a global mean μ_{global} and variance σ_{global}^2 instead of product of individual standard deviations:

$$C_{u_i^j, u_k^l} = \frac{\langle (u_i^j - \mu_{global})(u_k^l - \mu_{global}) \rangle}{\sigma_{global}^2}, \tag{2.8}$$

where μ_{global} is the mean of the ensemble of all the responses. In this global normalization, all the responses are concatenated into a time series, and then normalized as a whole. In the case of a pulsed drive, it excludes the pulses. This causes a centering around zero that highlights the small differences in the amplitudes of the responses. This new method to compute correlations is capable to highlight subtle changes between responses that, with the locally normalized coefficient, would have remained hidden. An example of this could be two responses characterized by a positive growth of the power intensity but with different slopes. The new global centering would distinguish the two types of responses with a lower correlation value than the Pearson coefficient. Whether for the calculation of μ_{global} and σ_{global}^2 one uses the time traces excluding the pulses, or just the portions of time traces corresponding to the windows used for the correlation, is a free choice. In the following, the results shown correspond to the second case. The final correlation would then be given by the average of all the pairwise calculated values.

We can now define the intra-correlation as the correlation for responses along the same sequence:

$$C_{intra} = \frac{1}{MN(N-1)} \sum_{k=1}^{M} \sum_{i=k}^{M} \sum_{l=1}^{N} \sum_{\substack{j=1 \\ j \neq l}}^{N} \frac{\langle (u_i^j - \mu_{global})(u_k^l - \mu_{global}) \rangle}{\sigma_{global}^2} \tag{2.9}$$

This formula calculates, for every repetition i of the drive, the correlation of each response window with the rest of the responses, excluding the self ones.

The inter-correlation is defined as the correlation for the same response window across different repetitions of the drive:

$$C_{inter} = \frac{1}{MN(M-1)} \sum_{k=1}^{M} \sum_{\substack{i=1 \\ i \neq k}}^{M} \sum_{l=1}^{N} \sum_{j=l}^{N} \frac{\langle (u_i^j - \mu_{global})(u_k^l - \mu_{global}) \rangle}{\sigma_{global}^2}. \tag{2.10}$$

Equation 2.10 calculates the correlation of the same response window l across the multiple repetitions k of the drive, excluding the self ones.

There is another way to compute these correlations with less computational demand based on an ensemble of responses, where the term ensemble refers to the set of all responses. For

that, the ensemble needs to be centered and globally normalized. The normalization should be performed again as if all the responses were concatenated to a new time series. The criteria can be expressed as:

$$\frac{1}{MN} \sum_{i,j} \frac{1}{T} \int_0^T dt \, u_i^j(t) = 0 \qquad (2.11)$$

$$\frac{1}{MN} \sum_{i,j} \frac{1}{T} \int_0^T dt (u_i^j(t))^2 = 1. \qquad (2.12)$$

A well-behaved intra-correlation based on the globally normalized ensemble compares all the individual responses, similar to the pairwise correlation coefficient, and averages over the repetitions.

$$C_{intra} = \frac{1}{(N^2 - N)M^2 T} \sum_{j \neq l} \sum_{i,k} \int_0^T dt u_i^j(t) u_k^l(t) \qquad (2.13)$$

This formula correlates all the individual responses without excluding any particular combination except the self one. Limiting the intra-correlation to calculations within the same sequence would only affect the normalization factor. Analogously to the intra correlation, the globally normalized inter-correlation can be written as:

$$C_{inter} = \frac{1}{(M^2 - M)NT} \sum_{j \neq l} \sum_{i,k} \int_0^T dt u_i^j(t) u_k^l(t). \qquad (2.14)$$

However, another helpful expression can be derived for the calculation of the inter-correlation through the distance of the individual responses to their mean, which gives an idea of the ensemble spread. We can write the ensemble mean $\tilde{u}^j$ that depends on the event j:

$$\tilde{u}^j = \frac{1}{M} \sum_i u_i^j(t). \qquad (2.15)$$

And we can calculate the distance of the individual responses to their ensemble mean as:

$$D_j^2(t) = \frac{1}{M} \sum_i (u_i^j(t) - \tilde{u}^j(t))^2. \qquad (2.16)$$

It can be shown that the distance of a response to the ensemble mean is connected to the inter-correlation like:

$$C_{inter} = 1 - \frac{1}{1 - 1/M} \frac{1}{NT} \sum_j \int\limits_0^T dt D_j^2(t). \tag{2.17}$$

where the normalization factors contemplate the projection of all the responses to a certain event onto each other excluding the self-projection. This is a useful expression that permits to split the correlation into meaningful contributions and distinguish for an event-dependent correlation.

The inter- and intra-correlations are very intuitive measures for consistency. A high correlation value would indicate a consistent response of the system, whereas a low correlation value would suggest an inconsistent response. The inter-correlation is an indicator of the reproducibility of the amplitude pattern for a given response. A correlation of 1 would correspond to a complete consistent response, meaning that the responses would overlap into a narrow line. With a correlation of 0, the ensemble of responses would display an unstructured distribution.

The intra-correlation compares responses to different events. This might be of interest to identify whether consistency depends on the occurrence of a certain event or, on the contrary, the system responds consistently to any sort of perturbation. The first case should translate into a high inter-correlation and lower intra-correlation, while the latter should display similar inter- and intra-correlations. This method also allows for a whole gradient of consistency, and can provide insights into the memory capabilities of the system when the repetitions are compared.

Inter- and intra-correlations also unveil important information on the statistical properties of the nonlinear system. Using a pseudorandom pulsed sequence as example of modulation, every occurrence of a pulse is acting as a trigger for the evaluation of the responses. If one interprets the inter-correlations as an ensemble average of the responses, provided that it uses repetitions from the same trigger, and the intra-correlations are considered a time average between different responses from different trigger points, the inequality between the two quantities would reveal that the system is not ergodic in this sense [72].

Focusing on the intra-responses, their dissimilarity can illustrate the time scales at which the memory effects remain. If the separation between the pulses were long enough, the trajectories would have enough time to reach the attractor after the perturbations, and therefore, we would not expect much difference between the inter- and intra-correlations. But in cases in which the influence of the previous pulses is visible, the time scale of the memory is larger than the intervals between the perturbations, preventing the trajectories to reach the stable attractor. Hence, under such circumstances, the inter-correlation values are higher than the intra-correlations.

2.2.3 Review of the consistency measures

Consistency is a property that lacks a rigorous definition so far and, consequently, of a mathematical framework with clear tools to quantify it. All the measured quantities rely on the

definition of consistency based on the similarity between responses, but no clear boundaries between inconsistent, consistent and complete consistent response have been determined. Depending on the drive-response system, different measures are suited to estimate the degree of consistency. Calculation of correlations in their different forms (Pearson coefficient, distance to a response, autocorrelations or distinguishing inter- and intra-correlations), have been employed to indicate the similarity of the responses. Their use is motivated by the ability to extract these quantities from experimental recorded data, specifically, from time traces of the dynamics.

Their interpretation is also very straightforward. The consistency correlation, understood as the correlation between responses (either inter or intra) to a repeated drive, is a meaningful measure that allows for a whole range of consistency, scaled from zero to one. A Pearson coefficient close to one also indicates that two responses are almost identical, but does not take into account differences in the offset of the responses. In a single system with delayed feedback, in which the delayed signal acts as an external drive, the autocorrelation function can be interpreted as a consistency measure too. The height of the delay echoes imply a high similarity in the trajectories, and thus, a consistent response to the self-delayed input.

All these measures can be good indicators of the consistency properties, although there are situations in which they might fail. For instance, experimental issues, like a poor signal-to-noise ratio, can easily induce inaccurate correlation values. In the case of a behavior, which in an ideal system would be completely consistent, the presence of mechanisms that could temporally alter the synchronization of the responses, such as bubbling, could lead to low correlation values, which would then be interpreted as not complete consistency or even inconsistency.

The sub-Lyapunov exponent is the quantity at the core of complete consistency, characteristic for the drive-response schemes. It affects the consistency properties of the response system and, in the case of delayed feedback systems, connects them directly with strong and weak chaos. In other words, the sub-Lyapunov exponent describes the conditional stability of the response of a dynamical system with respect to a certain drive. When the drive is a delayed feedback signal, a negative λ_0 indicates the presence of weak chaos. Under such circumstances, the response of the driven system is stable and can be consistent. With a positive λ_0, we operate in a regime of strong chaos and the response of the unit is not completely consistent. Yet it is difficult to extract the sub-Lyapunov exponent from experimental time traces.

Testing the consistency properties out of the complete consistency case becomes more intricate. The distinction between a high degree of consistency and inconsistency is not possible from the sub-Lyapunov exponent. Consequently, we recommend, when possible, a combination of both methods to characterize the consistency properties of the laser system. With the extraction of the sub-Lyapunov exponent and the correlation measures a good description of the consistency in a dynamical system can be achieved. Future methods to extract the sub-Lyapunov exponent, as well as the development of new tools to quantify consistency, will improve significantly the characterization of nonlinear systems.

2.3

Tools to measure unpredictability

Unpredictability is commonly measured by entropy rate [73]. In chaotic systems, unpredictability arises from the strong dependence on the initial conditions, so that small perturbations grow exponentially with time, limiting the abitility to predict future states. This sensitivity of the system to initial conditions can be quantified by the Kolmogorov-Sinai entropy, which is bounded by the sum of all positive Lyapunov exponents.

$$h_{KS} \leq \sum_{\lambda_i > 0} \lambda_i \qquad (2.18)$$

Given that any microscopic noise in the chaotic system amplifies the divergence of two nearby trajectories in phase space, chaotic systems can generate random information [74, 75]. In the context of information theory, Shannon's formula for the entropy rate characterizes how quickly the system generates unpredictable information [76]:

$$H(t) = -\sum_{i=0}^{1} P_i(t) \log_2 P_i(t) \qquad (2.19)$$

where $P_i(t)$ is the probability of occurrence of bit i (0,1) at the time t. As time evolves, the Shannon entropy increases, indicating a growth of uncertainty due to the spread of trajectories, and relates to the Kolmogorov-Sinai entropy. From experimental data, one can digitize the signal on one bit, so the chaotic dynamics can ideally generate up to one bit of entropy at a rate determined by the Lyapunov exponent. The time required for the system to reach an entropy value equal (or very close) to 1 is known as the memory time of the system.

By computing these quantities, one can estimate the rate at which random bits can be generated. Entropy calculations have also been used to explore the deterministic and stochastic aspects of a laser system used for random bit generation [74, 75]. Nevertheless, there are other measures that give an account of the unpredictability in the dynamics.

The autocorrelation function has been used to estimate the predictability: if future values of a time series depend on current and past values, the time series is predictable, and the dependence will show up in the autocorrelation function. The autocorrelation between times t and s for a process x is defined as:

$$AC(s) = \frac{< [x(t) - < x(t) >][x(t-s) - < x(t) >] >}{< [x(t) - < x(t) >]^2 >} \qquad (2.20)$$

The autocorrelation function of the output of a semiconductor laser subject to delay feedback will present delay signatures at lags of the delay time τ. The height of the delay echoes serves as an indicator of the existence of repeating patterns in the dynamics, so a complete suppression of the correlation peak is desirable. This property can also be formulated as the

preference to operate in strong chaos conditions. The memory time effects of the system are also contained in the decay of the zeroth autocorrelation peak, providing insights into the independence of successive data points [77]. In addition to the autocorrelation function, the mutual information can be used to measure the uncertainty in the dynamics.

The unpredictability property of chaotic laser systems is mostly used in cryptographic applications, where the output of the laser needs to be chaotic, and to satisfy some noise-like features. The observation of some properties, although it cannot quantify the unpredictability, is key to guarantee a random behavior. The probability distribution functions of time series provide information about the appropriateness of the dynamics for unpredictability. Symmetrical distributions that resemble a Gaussian distribution are more favorable, and considered a good starting point for most chaotic applications. In terms of frequency components, the spectrum of an unpredictable time series should be broad, and have a flat power spectral density, similar to the white noise spectrum [77].

Other methods to estimate the unpredictability include the already mentioned calculation of the maximal Lyapunov exponent, the Kaplan-Yorke dimension or the phase space reconstruction of an attractor using data [19, 74, 75, 78].

Consistency of a semiconductor laser to its own time delayed feedback

"The range of nonlinear
dynamics is often largely
underestimated."

Thomas Jüngling, Physicist.

3.1
Introduction

Consistency in dynamical systems has proven to be a powerful concept due to the ubiquity of drive-response schemes in nature and technology. The ability to respond in a similar way to similar inputs, starting each time from different initial conditions, is a necessary condition for the reliable operation of the systems. Cognitive tasks in neuron dynamics [79] or bio-inspired information processing [26, 57, 80, 81, 82] strongly depend on a consistent behavior. The first experimental work on consistency was introduced in 2004 by Uchida et al.[83]. In their experiment, a laser system is driven repeatedly by the same drive signal in order to describe the reproducibility of the responses. Recent numerical and experimental advances on consistency [84, 85, 86] also comprise the characterization of generalized synchronization properties of laser systems (see Chapter 1) driven by common light sources with fluctuating phase and or amplitude [87, 88, 89, 90, 91].

In this Chapter, we focus on two aspects of consistency that are critical for a controllable application. The first is the development of an experimental scheme providing a high quality repeated drive for fast experimental systems. To extend the investigations on consistency beyond the use of electrical drives, we need to design an experiment that allows to store non-scalar drives, such as optical signals, and inject them again while preserving the high optical and dynamical bandwidths. To achieve this, we employ a configuration of a photonic delay system with multiple feedback loops.

The second is the application and extension of time series analysis methods in order to reveal insights into the mechanisms underlying the consistency, like the extraction of the sub-Lyapunov exponent. Although the sub-Lyapunov exponent is at the core of the consistency property, up to now, it has not been possible to determine it experimentally. Small mismatches between response systems are sufficient to impede from its determination. There are only indirect indications for the transitions between consistent and inconsistent responses like spectral or intensity autocorrelation signatures of the laser dynamics in case of delayed feedback [92] or delay-coupled lasers [93]. However, the information contained in the delay echoes of the autocorrelation function can lead to misinterpretations. A high delay echo implies a similar repetition of the trajectory after a delay time, and can be seen as a consistent response of the system. But the Ikeda system [37] is the counterexample. This delay system has a constant sub-Lyapunov exponent for all the regimes investigated, although the shape of the autocorrelation changes with the parameters [94].

To explore the consistency properties, we employ a semiconductor laser subject to a drive originating from time-delayed optical feedback. It is well-known that delayed optical feedback induces high dimensional chaotic dynamics in semiconductor lasers [30]. Here, we use this mechanism as an ideal generator for complex optical drive signals. Therefore, we adapted the idea of a repeated drive [83] to the case of coherent and high bandwidth optical drive signals. Our scheme is based on two switchable feedback loops with significantly different lengths. This setup allows to store the optical drive in the long fiber loop while the short loop is active, and to replay it while the short loop is blocked. As a novelty, the replay offers all the features of the signal with high accuracy and without practical limitations with respect to optical and dynamical bandwidth. Even the optical phase dynamics is maintained, as long as the self-phase modulation does not become relevant. Moreover, in comparison to an equivalent generalized synchronization scheme using a replica system, we minimize mismatches by construction because the same laser is driven by the repeated signals. The combination of the small mismatches with the high quality of the replay allows for a direct quantification of the consistency properties experimentally with a measure proportional to the sub-Lyapunov exponent.

The results presented in this Chapter have been published as N. Oliver, T. Jüngling and Ingo Fischer, *Consistency Properties of a Semiconductor Chaotic Laser Driven by Optical Feedback*, Phys. Rev. Lett., vol. 114, 123905, March 2015. The experiments were performed by N. Oliver with the help of T. Jüngling. The analytical investigations and numerical simulations of sections 3.3.2 and 3.4 were carried out by T. Jüngling.

3.2

Experimental implementation

Figure 6.2 shows the simplified experimental scheme. The laser diode is an Eblana Discrete Mode Laser lasing at 1.54μm with a threshold current of the solitary laser of $I_{th} = 11.8$mA. The laser light is split to simultaneously enter two optical fiber loops, a short one with a
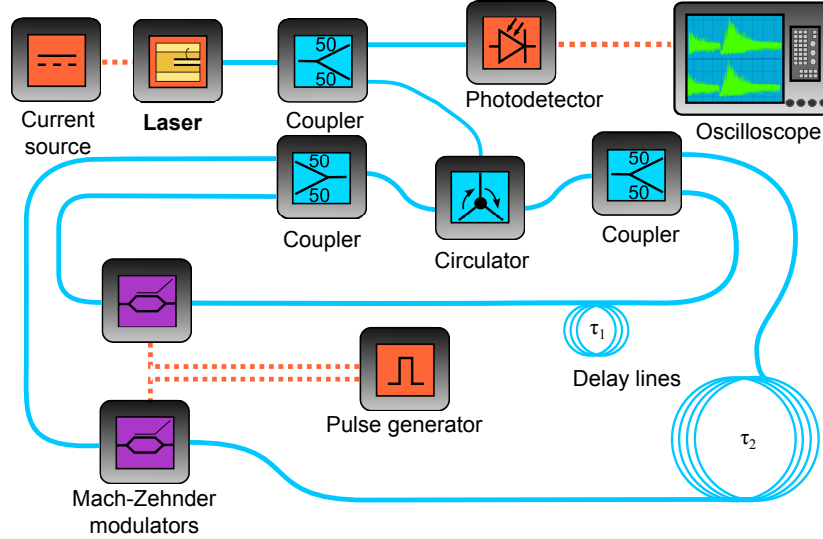
Figure 3.1: Experimental consistency setup. Figure from [86].

roundtrip time of $\tau_1 = 111$ns, and a much longer one with $\tau_2 = 21\mu$s. At the end of each fiber loop, the light passes through a Mach-Zehnder modulator. These electro-optical modulators are controlled by a pulse generator with a 50% duty cycle, such that when one path is closed, the other one is blocked. The period of the modulation is set to 50μs, and the switching time of the pulses is < 200ps. During the first 25μs, the laser receives feedback from the short delay loop, giving rise to the characteristic chaotic delay dynamics. When the short path is open and the long delay loop is active, the laser receives a replay of the optical field it already received a time $\tau_2 - \tau_1$ before.

We carefully designed and adjusted the system to obtain an exact repetition of the previous optical field, although the initial conditions of the laser are not the same. Temperature and pump current of the laser are controlled with an accuracy of ±0.01K and ±0.01mA, respectively. To obtain data of sufficiently high quality for the presented analysis, a strict control over the feedback parameters of the experiment is required. Therefore, other optical components, like polarization controllers and attenuators (not shown in the simplified scheme of Fig. 6.2), are set in the experiment to adjust and control the three following degrees of freedom:

- The first is related to the polarization state of the light. The short loop and the long loop must have the polarization state adjusted relative to each other as well as with respect to the laser output. Three polarization controllers placed along the experiment help in that task. The first one is settled right after the circulator to adjust the polarization of the light from the laser. The second and the third polarization controller are placed in the long delay loop, and in the common feedback loop entering back into the circulator, controlling the polarization of the feedback loops. By tuning the three polarization

controllers subsequently, a perfect match between the polarization state of the light from the feedback loops and the laser output is achieved.

- The second degree of freedom is related to the remaining transparency of the blocked loop. When a loop is active, the feedback light from the other loop needs to be suppressed. In order to achieve this, we added an external modulation to the laser, and monitored the spectrum of the intensity as detected by a photo diode with a realtime spectrum analyzer. We tuned the operating point of the Mach-Zehnder modulators in a way that the frequency signature of the modulation was imperceptible. With this procedure, a suppression of more than 25dB of optical power in the blocked loop can be achieved.

- Finally, short loop and long loop have to be equally transparent when they are active. Therefore, an attenuator in the short loop is used to guarantee the same level of transparency among the two loops with a precision of ±0.01dB.

To facilitate the identification of the short loop and the long loop in the recorded time traces, we add a delay of $10ns$ between the switching process of the modulators. With this delay, every cycle of short-long loop dynamics contains $10ns$ in which both loops are blocked at the same time. The laser output is detected with a photodiode of 12.5GHz bandwidth and a digital oscilloscope with 16GHz analog bandwidth. After removing the transient intervals originating from the switching process, we compare the dynamics induced by the short feedback loop with the corresponding dynamics induced by the replay from the long loop to test consistency of the laser's responses. An illustration of the operation principle of the experiment is shown in Fig. 3.2.

3.2.1 Dynamical performance

The dynamical performance of the experiment can be seen in the spatio-temporal representations [95]. In such plots, the output power of the laser is color-coded, the horizontal axis represents the time up to the roundtrip time τ_1, and the vertical axis displays the 185 repetitions of τ_1 within each cycle. The spatio-temporal plots of the laser intensity output for the short loop cycle and for the long loop cycle are plotted in Fig.3.3(a) and (b) respectively.
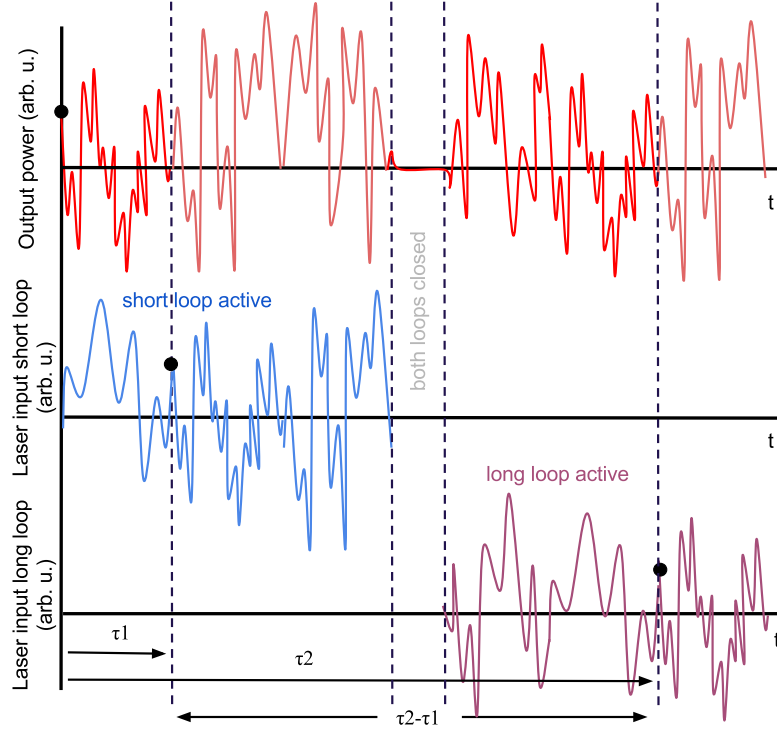
Figure 3.2: Schematic illustration of the operation of the setup. The first panel depicts the output of the laser. The second panel shows the operation of the short loop, which is active for $25\mu s$ (blue) and during that time, the laser evolves to its typical delay chaotic dynamics (red), while the long loop is blocked, serving as optical memory. During $10ns$, both loops are closed. When the long loop is connected (purple), the laser receives a copy of the optical field it received a time $\tau_2 - \tau_1$ before. The output of the laser from the short loop and the long loop with the corrected time deskew (light red) are then compared to test the consistency.
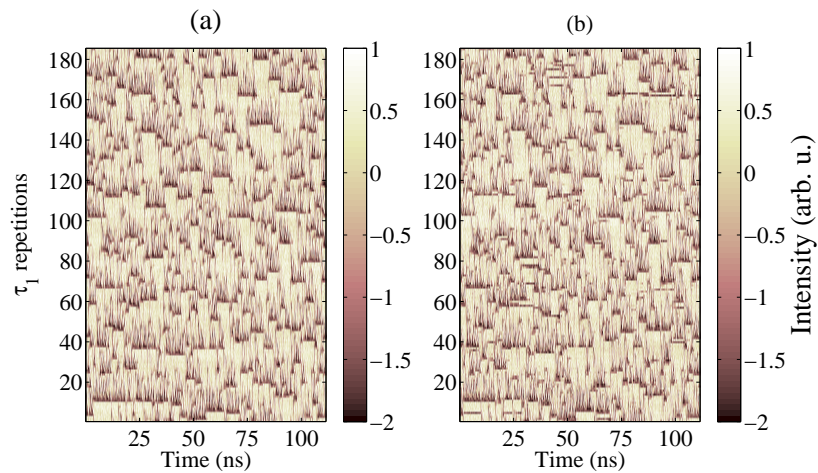

Figure 3.3: Space-time plots of the laser output acquired at $I = 1.0 I_{th}$ for (a) short loop cycle, (b) long loop cycle.
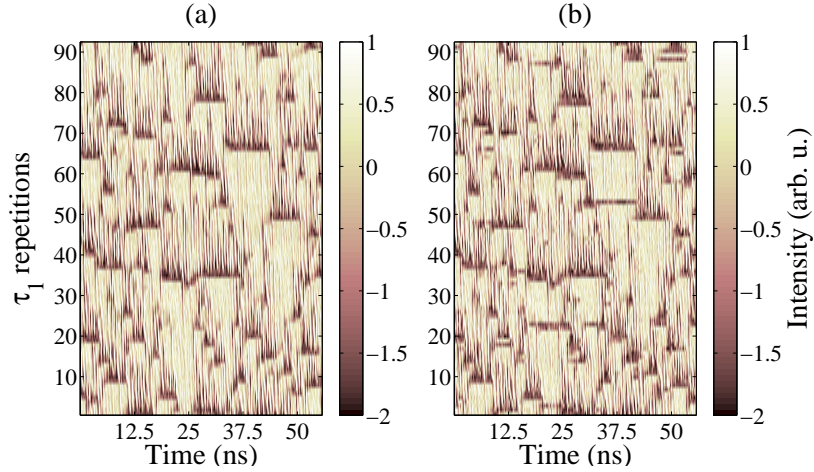
Figure 3.4: Zoom of the space-time plots of the laser output acquired at I $= 1.0 I_{th}$ for (a) short loop cycle, (b) long loop cycle. Figure from [86].

Fig.3.3(a) and (b) shows the spatio-temporal plots of the laser intensity output for the short and long loop respectively, acquired at I$=1.0 I_{th}$. The dynamics is governed by chaotic intensity fluctuations including irregular power dropouts, characteristic of the chaotic feedback regime of Low Frequency Fluctuations (LFFs) [96, 97]. The dynamics in the LFFs regime exhibits a slow increase of the intensity, without reaching a stable level. They also present strong oscillations in the subnanosecond-scales until a dropout occurs. These spontaneous dropouts, represented in dark color, are present after some repetitions of the delay time. The dynamics induced by the short and long feedback loop exhibit the same patterns, illustrating the high accuracy of the replay and the consistency properties for the given conditions. A better visualization of the correspondence between short and long loop can be obtained from a zoom of the space time plots (Fig.3.4). The major differences, displayed as dark horizontal lines in Fig. 3.4(b), correspond to additional noise-induced dropouts occurring during the replay. Given that the short loop acts as the common drive, these dropouts are not maintained after one delay time τ_1, meaning that the system in the long loop cycle catches up to the original patterns and restores consistency. One should not misinterpret these features as impurities or noise effects; they are dynamical phenomena like intermittency or bubbling, which hamper the achievement of a perfect match between the two loops. Although Fig. 3.4 illustrates the good correspondence between the two responses, this is not a general characteristic. It is rather related to the particular dynamical regime which corresponds to a high level of consistency.

In contrast, Fig. 3.5 shows spatio-temporal plots of the laser output for the short (a) and long loop (b) acquired for a different pump current ($I = 1.27 I_{th}$), by which we vary the dynamical properties. The laser dynamics are characterized by fast chaotic fluctuations, which makes the identification of the consistency properties hard on this entire scale. However, we can observe that Fig. 3.5 (a) and (b) are statistically similar, which again proves the high
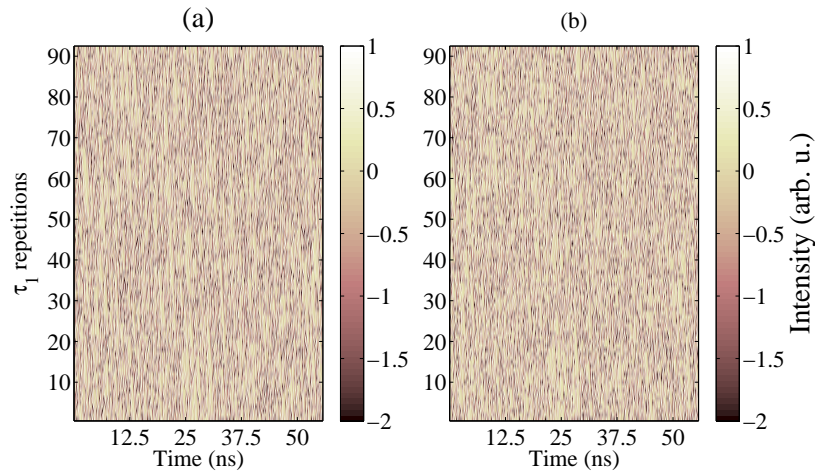
Figure 3.5: Zoom of the space-time plots of the laser output acquired at I = 1.27I_{th} for (a) short loop cycle, (b) long loop cycle.

quality of the replay setup.

Fig 3.6 shows a zoom of the space time plots at I = 1.27I_{th}. Similar structures can be identified in the plots of both loops. Even though the laser received the same drive, there is not a one-to-one correspondence between figures (a) and (b). In particular, the individual structures displayed in the short loop are not captured by the long loop. Again, this is a dynamical feature not related to experimental mismatches between the loops, and means that the response of the laser to its feedback is inconsistent here. These results illustrate the ability of the laser to exhibit different and independent responses to the same drive depending on the dynamical regime, thus indicating different levels of consistency.

3.3

Quantifying consistency from experimental data

3.3.1 Consistency correlation

Consistency of the laser response is directly quantified by the cross-correlation coefficient between power output signals $x_1(t)$ and $x_2(t)$ from the short and the long loop cycle, respectively. We denote it as *consistency correlation*

$$C_c = \langle x_1(t)x_2(t) \rangle \tag{3.1}$$

where each segment is normalized such that $\langle x_i(t) \rangle = 0$ and $\langle x_i^2(t) \rangle = 1$, $i = \{1, 2\}$, and the time arguments have been deskewed by $\tau_2 - \tau_1$. Additionally to this measure, we evaluate the autocorrelation function for each of the cycles, and determine the maximum correlation of the first delay echo [92], which was used as an indicator for strong and weak chaos. We
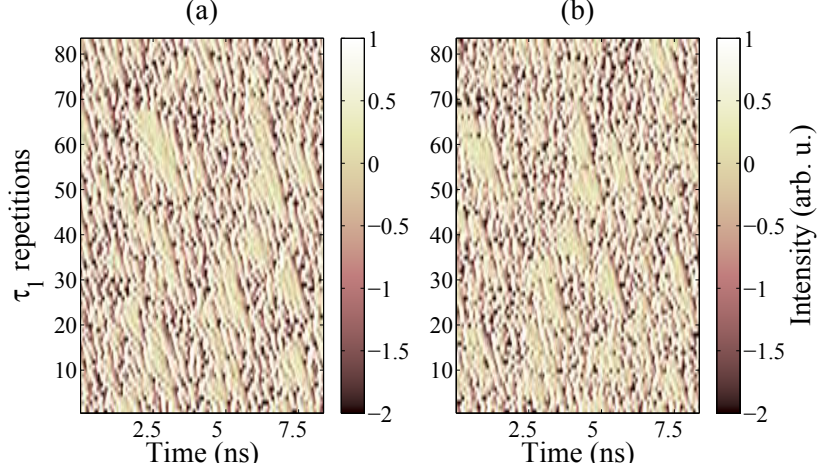
Figure 3.6: Zoom of the space-time plots of the laser output acquired at I = $1.27 I_{th}$ for (a) short loop cycle, (b) long loop cycle. Figure from [86].

calculate

$$C_i = \langle x_i(t) x_i(t - t_i) \rangle, i = \{1, 2\} \tag{3.2}$$

with the same normalization as above, and $t_1 \approx t_2 \approx \tau_1$ being the peak positions close to the short delay for short and long loop cycle, respectively. Figure 3.7 shows these three correlation measures as a function of the pump current.

We observe that all of the selected correlation coefficients follow the same trend by developing a single minimum at moderately low pump currents, and then rising and saturating for higher pump currents. This is a particular feature of the semiconductor laser and might not be the case for other systems. Consistency correlations up to $C_c \approx 0.99$ exemplify the high quality of the replay setup. The minimum of all correlation coefficients around $I = 13$mA indicates a possible region of strong chaos interrupting weak chaos for high and low pump currents. Despite belonging to a region of weak chaos, the correlation coefficients for low pump currents do not reach values close to one due to an insufficient signal to noise ratio. At high pump currents the values of C_1 and C_2 converge, because the signals in cycle 1 and 2 are practically identical. Around the minimum, the discrepancy between C_1 and C_2 is largest. It originates from consistency properties rather than mismatch of the drive signals. Analyzing the entire autocorrelation functions, we find that the difference is only affecting the delay echoes, whereas the zero-peak structure is identical in both cycles.

Figure 3.8 shows a detail of the autocorrelation (AC) function of the intensity dynamics for both loops obtained at $I = 1.27 I_{th} = 15$mA. According to our results, this regime corresponds to an inconsistent response of the system. The resolved AC function around zero time shift is depicted in Fig. 3.8(a). The zeroth AC peaks of both loops coincide and present the same decay, in which correlations are lost after 1ns. Figure 3.8(b) shows the AC functions around the τ_1 peak. Although both delay echoes have an asymmetric shape, the signature
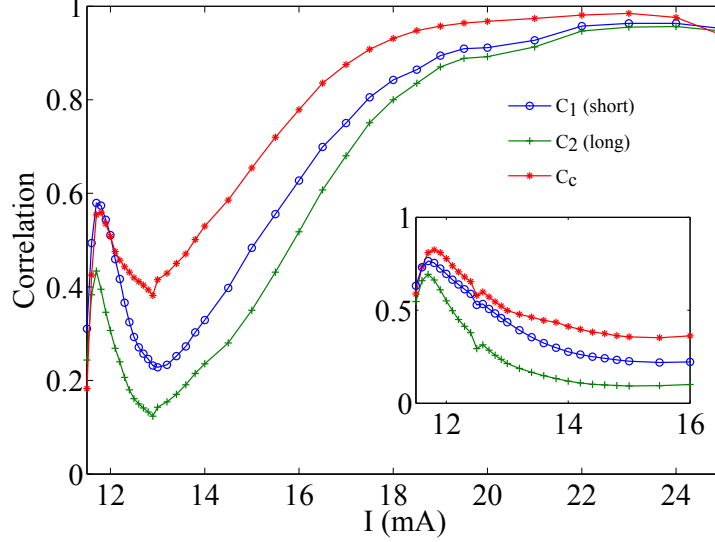
Figure 3.7: Correlation coefficients as a function of the pump current. Blue and green curves show the autocorrelation coefficients for the short and long loop cycle respectively. Red curve represents the consistency correlation. The inset shows the correlation coefficients for higher feedback strength, recorded with amplification of the detected signal. Peak positions t_1 and t_2 are depending on the pump current, and are located close to τ_1 within a margin of 50ps. Figure from [86].

from the long loop is smaller compared to the one from the short loop. The autocorrelation coefficients C_1 and C_2 are the maximum peak values of the corresponding functions in the shown range, which are close to $\tau_1 = 111$ns. In figure 3.8(b), the values of C_1 and C_2 would be different and small, corresponding to a regime of strong chaos. The difference between these signatures leads to the gap between C_1 and C_2. The correlation coefficient C_1 measures the response of the laser to its own τ-delayed signal. In contrast, C_2 measures a different relationship because, due to the inconsistency, the signal $x_2(t-\tau_1)$ is not the input underlying $x_2(t)$, but $x_1(t-\tau_1)$ which is only structurally similar, like a surrogate. The lost information is reflected in the gap between C_1 and C_2 and vanishes with increasing consistency. One could also see C_2 as an indirect indicator of strong and weak chaos.
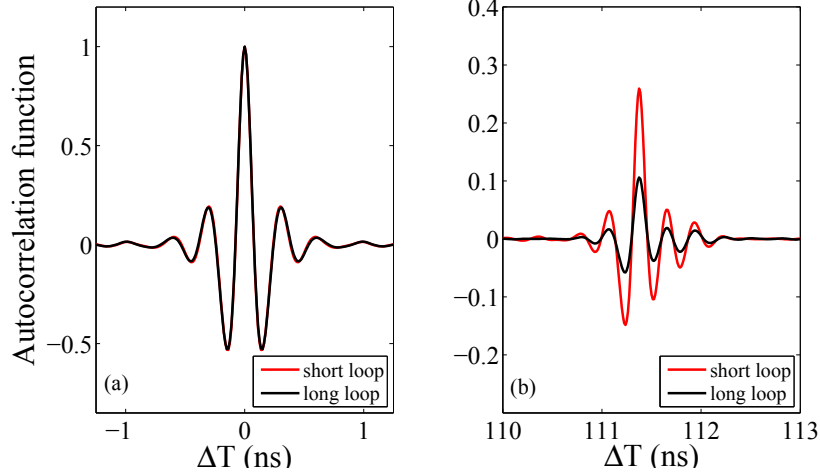
Figure 3.8: Autocorrelation function of the intensity dynamics for short loop (red) and long loop (black): (a) the resolved zeroth AC peak; (b) the resolved τ_1 peak. The curves correspond to the high feedback strength case (inset of Fig. 3.7, in which $\tau_1 = 111.42 \pm 0.05$ ns).

In order to study the transition from weak to strong chaos at low pump currents, we increased the feedback strength by almost a factor 2, changing the coupler located at the laser output for a 90/10 one. A semiconductor optical amplifier is placed in the detection path to overcome the subsequent loss in the detected signal power. The resulting correlation coefficients are shown in the inset of Fig. 3.7. The three correlation measures show a stronger increase for low and moderate pump currents with a maximum around $I = 11.8$mA. The consistency correlation at this point goes beyond $C_c > 0.8$, corroborating the region of weak chaos. For increasing pump current, the correlation functions develop again a minimum.

We have not accessed the curves for high pump currents, although we expect them to agree with the given results of the low feedback condition, so that the consistency recovers to high values. To validate the results from low and high feedback cases, we apply the rescaling procedure presented by Porte et al. [92], which allows for mapping the dynamics from one set of parameters to another. In particular, the dynamics found for a feedback strength κ at a relative pump current $p = I/I_{th}$ is equivalent to the dynamics at another feedback κ', when the current is changed according to a scaling law $(p' - 1)/(p - 1) = (\kappa'/\kappa)^2$. The collapsed curves for the different datasets of the 50/50 coupler and the 90/10 coupler to the pump current are shown in Fig. 3.9 for the consistency correlation. At low currents ($I < 12$mA), there is a difference in the maximum values of the correlation which is related to the level of measurement noise, being in the order of the small oscillation amplitudes close to the lasing threshold. Above 12mA, the two curves almost coincide with the position and the value of the local minimum agreeing as expected. Note that remaining differences can be related to the slightly varying experimental conditions and the different measurement path including an optical amplifier. Given the remarkable accuracy and range of the scaling regime, we

conclude that in an even higher feedback scheme, the same dynamical transitions would be found at correspondingly high currents.
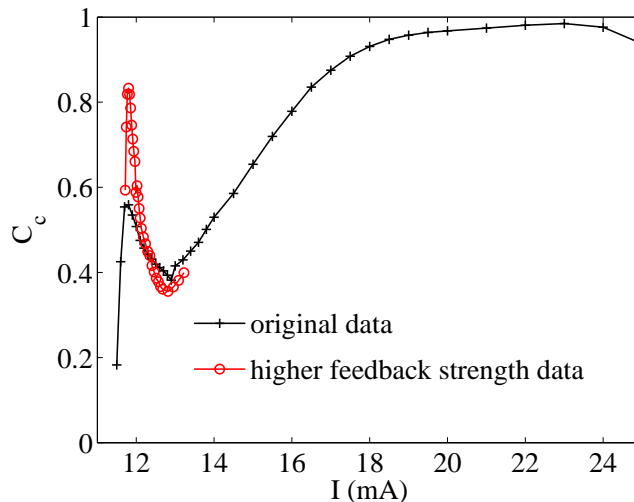

Figure 3.9: Consistency correlations as a function of pump current. Black line shows the consistency correlation for the data acquired with lower feedback strength. Red line shows the consistency correlation for the higher feedback case rescaled with a factor $(\kappa'/\kappa)^2$.

3.3.2 Sub-Lyapunov exponents from transverse distribution functions

Aside from the consistency correlation, the consistency properties can still be characterized with a more direct parameter: the sub-Lyapunov exponent. To obtain it from the experimental data is not a trivial task. Here, we present a method to extract the sub-Lyapunov exponent based on transverse distribution functions.

The transverse signal results from the substraction of signals from the short delay cycle $x_1(t)$ and the long delay cycle $x_2(t)$ deskewed $\tau_2 - \tau_1$.

$$v(t) = x_1(t) - x_2(t). \tag{3.3}$$

The term *transverse* refers to the corresponding generalized synchronization setup, in which $v(t)$ is the synchronization error, i.e., a projection of the phase space components transverse to the synchronization manifold. Thus, in case of high consistency, this transverse signal should be very close to zero. With normalization as above, the variance of the transverse signal $s_v = \langle v^2 \rangle - \langle v \rangle^2$ is directly connected to the consistency correlation by

$$C_c = 1 - \langle s_v^2 \rangle/2 = 1 - \langle v^2 \rangle/2. \tag{3.4}$$

However, additional information can be obtained from the distribution function of $v(t)$, where the sub-Lyapunov exponent leaves a signature. For complete synchronization of coupled dis-

crete maps, it was shown that the transverse component follows a power law distribution [53]

$$p(v) \propto |v|^{\sigma - 1}. \tag{3.5}$$

Here, the transverse component is obtained from the variables, denoting the state of identical maps with discrete time. The power law exponent σ is directly related to the transverse Lyapunov exponent λ_t, such that close to the synchronization threshold holds

$$\sigma \propto \lambda_t. \tag{3.6}$$

Although for continuous systems with vector-valued state variables a complete theory is not yet developed, we show how, in analogy to the case of discrete maps, it is possible to extract a power law exponent σ which is proportional to the sub-LE λ_0. To do so, we need the linearized equations of motion close to the consistency manifold $\mathbf{x}_1(t) \approx \mathbf{x}_2(t)$ where $\mathbf{x}_1, \mathbf{x}_2$ denote the B-dimensional state vectors of the system. We stress that, with the experimental intensity time traces alone, we can only access a scalar projection of such state vectors. The system follows the set of equations of the form:

$$\begin{aligned}
\dot{\mathbf{x}}_1(t) &= \mathbf{f}(\mathbf{x}_1(t)) + \kappa \mathbf{h}(\mathbf{x}_1(t - \tau_1)) \\
\dot{\mathbf{x}}_2(t) &= \mathbf{f}(\mathbf{x}_2(t) + \kappa \mathbf{h}(\mathbf{x}_1(t - \tau_1)).
\end{aligned} \tag{3.7}$$

Here, $\mathbf{x}_1 \in \mathbb{R}^3$ is the state of the drive system receiving delayed feedback by a coupling function $\mathbf{h}$ with strength κ and delay τ. $\mathbf{x}_2 \in \mathbb{R}^3$ is the state of the identical response system driven by the same delayed feedback $\mathbf{x}_1(t - \tau_1)$, so that the setup supports complete synchronization. The transverse state vector is defined as

$$\mathbf{v}(t) = \mathbf{x}_1(t) - \mathbf{x}_2(t). \tag{3.8}$$

Assuming that $\mathbf{v}(t)$ describes a small perturbation governed by linearized equations of motion, the logarithm of the perturbation size, defined as

$$l_v(t) = \ln \|\mathbf{v}(t)\| \tag{3.9}$$

leads to

$$\lambda_0 = \lim_{t \to \infty} \frac{l_v(t) - l_v(0)}{t} = \langle dl_v(t)/dt \rangle_t \tag{3.10}$$

as its average growth rate. In agreement with this definition, we can write a differential equation

$$dl_v(t)/dt = \lambda_0 + \eta(t). \tag{3.11}$$

The sub-Lyapunov exponent acts as the drift term while the term $\eta(t)$ incorporates the finite time fluctuations of the Lyapunov exponent such that $\langle \eta(t) \rangle_t = 0$. Assuming the same limiting and reinjection mechanisms as in the corresponding theory for the discrete maps, we expect an exponential distribution

$$\rho(l_v) \propto \exp(\sigma l_v) \tag{3.12}$$

with

$$\sigma = \lambda_0 / D. \tag{3.13}$$

The scaling factor D is related to the intensity of the fluctuations in $\eta(t)$. If $\eta(t)$ were white noise, its spectral power density would be $2D$ accordingly. The exponential distribution is valid only in the regime governed by the linear equations of motion. For small arguments l_v the distribution is limited by noise and parameter mismatches, which in the double delay loop experiment only arise from the minimal differences between the two feedback loops. This is a major reason for the resulting high quality of the transverse signal, which allows for the analysis of the distribution function $\rho(l_v)$. For large arguments l_v, the distribution is cut off by nonlinearities because the transverse coordinate is bounded by the typical standard deviation of the trajectories.

Sub-Lyapunov exponent from experimental transverse distribution functions

To obtain the transverse distribution function from the experimental time traces $x_1(t)$ and $x_2(t)$, a reconstruction of the vector states $\mathbf{x}_1(t)$ and $\mathbf{x}_2(t)$ is necessary. We choose the canonical delay embedding [98, 99] with an embedding dimension b and an embedding delay h, such that each vector state is approximated by

$$\mathbf{x}_i(t) \sim \mathbf{y}_i(t) = (x_i(t), x_i(t-h), \ldots, x_i(t-(b-1)h))^\top, i = \{1, 2\}. \tag{3.14}$$

Although the embedding reconstruction is not guaranteed formally by Taken's theorem, because the signals originate from externally driven systems, the reconstruction error is expected to be reduced in the transverse signal because the explicit dependence on the external drive vanishes here. Thus, we calculate the logarithmic distance

$$l_v(t) = \ln \|\mathbf{y}_1(t) - \mathbf{y}_2(t)\| \tag{3.15}$$

for different values of embedding dimension and embedding delay. To corroborate these assumptions, we have numerically simulated this scheme with the Lang-Kobayashi rate equations. The analysis is shown in section 3.4.

To calculate 3.15, we reconstruct the phase space with delay embedding for a dimension $b \in \{1 \ldots 7\}$. Again, the time axis of the long loop is properly deskewed by $\tau_2 - \tau_1$. Two experimental distribution functions $\rho(l_v)$ for two different pump currents are shown on a logarithmic scale in Fig. 3.10 for embedding dimension $b = 3$. The embedding delay is chosen as the first zero-crossing of the autocorrelation function from the short loop signal. In the two figures, three regimes can be identified:

1. On the left side, the distribution is dominated by the small differences between the loops, mainly due to intrinsic noise. The scaling of this regime reveals the embedding dimension b, which agrees with the slope of the curve.

2. The regime in the middle is governed by the linear equations of motion, and presents the constant slope σ that we extract.

3. On the right side, the regime is mainly characterized by a high amplitude cutoff due to the nonlinearities of the system. This is because the difference between short and long loop is bounded by the standard deviation of the transverse signal, i.e. the size of the attractor.
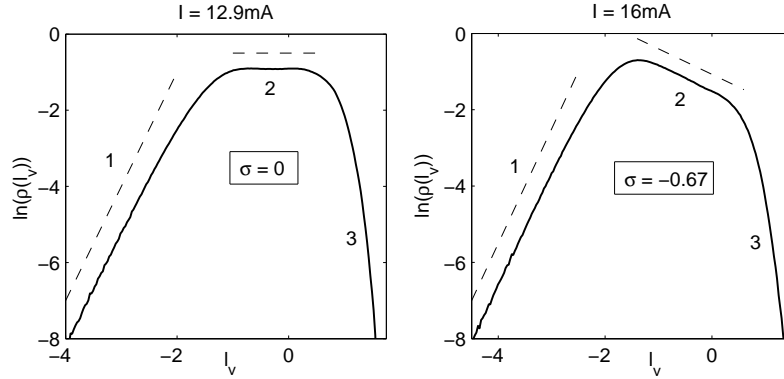

Figure 3.10: Distribution functions of the logarithmic synchronization error $l_v = \ln \|\mathbf{y}_1 - \mathbf{y}_2\|$ between short and long loop for two different pump currents revealing two different values of the slope σ. In the logarithmic plot, one can distinguish three regimes as labeled. 1) Noise-dominated. The slope agrees with the embedding dimension as indicated by the dashed line. 2) Intermediate regime governed by Lyapunov stability reveals slope σ, indicated by dashed line. 3) Cutoff regime due to boundedness of transverse component.

As shown in Fig.3.10, different operating conditions lead to different plateaus of the function $\ln(\rho(l_v))$ with slope $d\ln(\rho(l_v))/dl_v$ and consequently, different values of σ. Next, we determine the slope σ in the useful intermediate region from the set of transverse distribution functions for different embedding dimensions. For each of the time series, we extract the value of σ from the distribution function $\rho(l_v)$. The main criterion for the method is the convergence of the slope by increasing embedding dimension as illustrated in Fig. 3.11. The slope of the logarithm of the distribution function, $d(\ln(\rho(l_v)))/dl_v$, is shown for embedding dimensions $b = 2$ to $b = 7$. In the noise-dominated regime where values of l_v are small, the slope indicates the dimension. For large l_v, the fall-off corresponds to the cutoff of the distribution function. In the intermediate regime, there is a plateau in which all slopes converge. The red circle indicates the selected point for determination of σ and its uncertainity, in this example $\sigma = -0.26 \pm 0.02$. The useful plateau might reduce to a single minimum for high dimensions.

At very low or very high pump currents, the convergence becomes less clear or not detectable; thus, we assign larger tolerances from the spread between the curves or choose not to extract a σ-value for the extreme cases. The reason for the loss of clarity has again different origins depending on the case. For low pump currents, it is due to the lower signal-to-noise ratio. For high pump currents, there is intermittency between stable emission and undamped relaxation oscillations, which are persistent on timescales larger than the acquisition time.
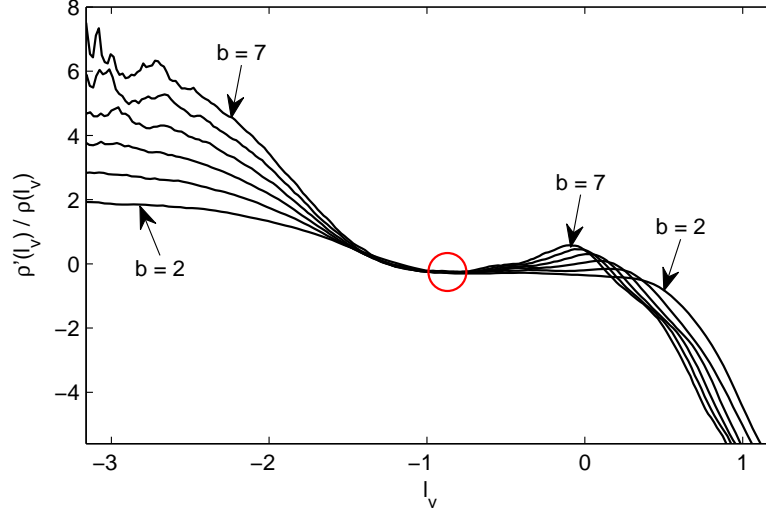
Figure 3.11: Illustration of the extraction of the value σ from the derivative of $\ln(\rho(l_v))$. Example shown for phase space reconstruction at $I = 14.5\text{mA} = 1.23 I_{th}$ using the first zero-crossing of the short loop autocorrelation function as embedding delay.

The result is a multiscale transverse distribution function. Overall, the tolerances assigned to the extracted σ-values can be regarded as a procedural error. On a linear scale, the useful range for the slope extraction typically resides in the regime of 10% to 30% of the high amplitude transverse bursts.

We would like to stress that the convergence of slopes is a consequence of the power-law distribution in the transverse variable of the setup (Eq. 3.5). This distribution function is invariant under different projections and embedding dimensions. Therefore, the convergence property is a general characteristic of dynamical systems, beyond semiconductor lasers, that can be used as criterion for the σ extraction.

The main results of this analysis are summarized in Fig. 3.12, depicting the dependence of σ on the pump current. Starting with low values of σ for small currents, the curve develops a maximum coinciding with the minimum of correlations, and again decays for large currents. The values of σ over the whole range of pump current are mostly negative. We infer a large negative value of the sub-LE in the regimes of high consistency correlation, which means that intermittent bursts of the transverse variable are comparably rare, of low amplitude, and quickly recover towards periods of full consistency. The power law distribution of v with an exponent $\sigma - 1$ supports this picture, as for the negative σ, there is a pronounced peak centered at $v = 0$ with a rapid decay. For intermediate pump currents, at the studied conditions, we obtain only a slight zero crossing of σ and, thus, of λ_0. Simulations indicate that this is related to the α-parameter of the employed laser, being $\alpha \sim 2$ (see section 3.4). Interestingly, a sub-LE close to zero already causes a very low consistency correlation. This shows the role of the

finite-time fluctuations $\eta(t)$ on the sub-LE which lead to large and frequent excursions from the synchronized state. In this sense, one could consider these fluctuations, which originate from intermittent desynchronization events due to noise or parameter mismatches (bubbling events) [100], as a mechanism that counteracts consistency: although the system is stable to its drive, the transverse signal presents intermittent bursts. The correspondence between Fig. 3.12 and Fig. 3.7 confirms the relationship between the sub-Lyapunov exponent and the regimes of strong and weak chaos. The pump current, at which there is the minimum of the consistency correlation, coincides with the maximum value of σ, while the minimum values of the sigma curve correspond to high values of the consistency correlation. Hence, the studies on the transverse distributions complement and extend those of the correlation functions. Recalling the direct connection between the sub-Lyapunov exponent and σ, we demonstrated the direct determination of the sub-Lyapunov exponent from experimental data. In the next section, we corroborate this relationship with numerical simulations.
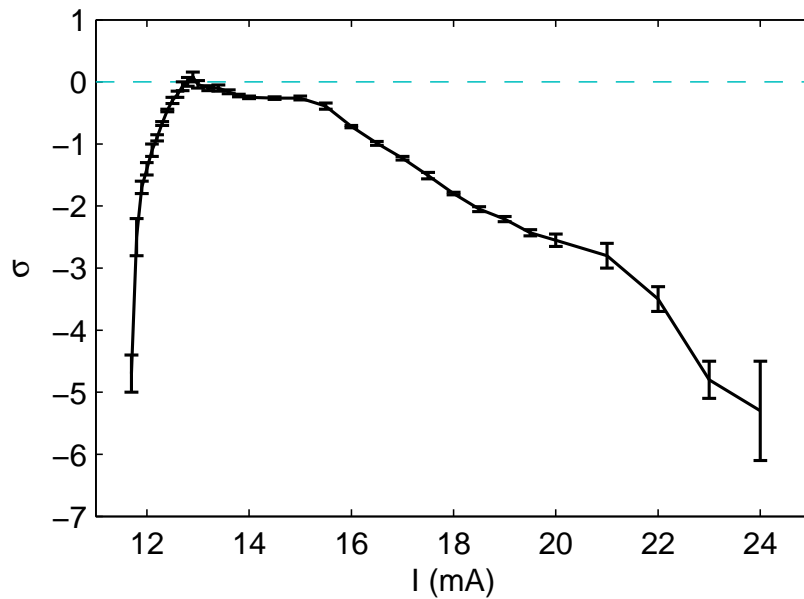
Figure 3.12: Slope $\sigma = d\ln(\rho(l_v))/dl_v$ in the intermediate regime of the transverse distribution functions. For the calculation of l_v we set the embedding delay h to the first zero-crossing of the autocorrelation function from the timetraces, and the embedding dimensions range from $b = 2$ to $b = 7$. Error bars denote the quality of convergence with increasing embedding dimension, thus, not containing systematic errors. Figure from [86].

3.4

Sub-Lyapunov exponent in numerical simulations

In order to verify our experimentally obtained results on the extraction of the slope σ, and our theoretical arguments regarding its relationship to the sub-Lyapunov exponent λ_0, we simulate a drive-response synchronization scheme with two identical units, as presented in Eq. 3.7. To introduce perturbations away from the synchronization manifold as in the realization of the experiment, we add a noise term to the equation of motion for $\dot{\mathbf{x}}_2(t)$. This noise term also allows to observe the transverse distribution function for negative sub-Lyapunov exponents by acting like a perturbation of the synchronization manifold. In comparison to the experiment, here, the state vectors of short and long loop $\mathbf{x}_1$ and $\mathbf{x}_2$ have the same time origin.

We implement the Lang-Kobayashi rate equations model [101] to simulate the dynamics of the semiconductor laser subject to delayed optical feedback. The drive and driven state contain real and imaginary parts of the complex electric field as well as the charge carrier number. The full equations for $\mathbf{x}_1 = (\Re(E_1), \Im(E_1), n_1)^\top$ and $\mathbf{x}_2 = (\Re(E_2), \Im(E_2), n_2)^\top$ read

$$
\begin{aligned}
\dot{E}_1(t) &= \frac{1 + i\alpha}{2} G_N n_1(t) E_1(t) + \kappa E_1(t - \tau) \\
\dot{n}_1(t) &= (p - 1)\gamma N_{sol} - (\Gamma + G_N n_1(t))|E_1(t)|^2 \\
\dot{E}_2(t) &= \frac{1 + i\alpha}{2} G_N n_2(t) E_2(t) + \kappa E_1(t - \tau) + \sqrt{2D}(\xi_1 + i\xi_2) \\
\dot{n}_2(t) &= (p - 1)\gamma N_{sol} - (\Gamma + G_N n_2(t))|E_2(t)|^2
\end{aligned}
\tag{3.16}
$$

with the following parameters: the gain coefficient $G_N = 2.142 \cdot 10^{-5} \text{ns}^{-1}$, the photon decay rate $\Gamma = 357 \text{ns}^{-1}$, the carriers decay rate $\gamma = 0.909 \text{ns}^{-1}$, the carrier density at transparency $N_{sol} = 170.7 \cdot 10^6$, and the linewidth enhancement factor $\alpha = 2.5$. The pump current enters as $p = I/I_{th}$, and we set it to 1.94. Feedback parameters are set to $\kappa = 10 \text{ns}^{-1}$ for the feedback strength and $\tau = 10 \text{ns}$ for the roundtrip time, which qualitatively resembles the experimental conditions nevertheless lacking detailed parameter adjustments. The noise term is set to act only on one of the two electric field components for the study of stability properties and the time series analysis method as white noise $\boldsymbol{\xi}(t)$ with $\langle \xi_i(s)\xi_j(t) \rangle = 2D\delta(t - s)\delta_{ij}$, $i, j = \{1, 2\}$, such that $\sqrt{2D\delta t} = 100$. The integration method is a stochastic Heun algorithm with step size $\delta t = 0.1 \text{ps}$.

Figure 3.13 summarizes the analysis of the transverse coordinate $\mathbf{v}(t) = \mathbf{x}_1(t) - \mathbf{x}_2(t)$ analog to the experimental procedure. The first derivative of the logarithm of the transverse distribution function $\rho(l_v)$ is shown for different embedding parameters. As in the experimental transverse distributions, the left side of the curves indicate the dimensionality of the embedding, while the right side presents a cutoff of the distribution function. The middle regime presents the convergence of the slope of all distribution functions over a wide range. For the thick black curve, l_v was obtained from normalized vector components $\Re(E)$, $\Im(E)$, n. For the colored thin lines, a delay embedding was applied to the intensity time traces
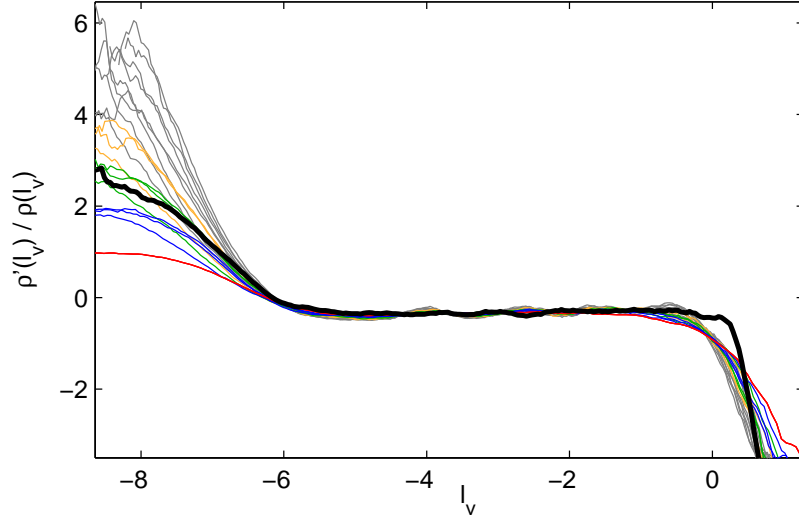
Figure 3.13: First derivative of $\ln(\rho(l_v))$ for various embedding parameters.

$P(t) = |E(t)|^2$. To achieve a match between all the plateaus, l_v from colored curves were properly shifted. The red curve corresponds to the case of no embedding $b = 1$. The rest of the curves are for embedding dimensions $b = 2$ (blue), $b = 3$ (green), $b = 4$ (orange), and $b = 5$ to $b = 7$ (gray). The multiple color curves are for various embedding delays h: $h = 0.5T_c$, $h = T_c$ and $h = 1.5T_c$ with T_c being the first zero-crossing of the short loop autocorrelation function. Due to the low noise level, we obtain a big range in which the distribution functions of $l_v = \ln \|\mathbf{v}\|$ scale with σ. The result is consistent and robust against different embedding dimensions and embedding delays applied to the time series of the intensity $P(t) = |E(t)|^2$, including even the non-embedded case of the difference signal $P_{x_1}(t) - P_{x_2}(t)$, in which false nearest neighbors appear frequently. Further, all slopes obtained by delay embedding of the intensity coincide with the slope obtained using the full vector state of $\mathbf{v}(t)$.

We also compare σ with the sub-Lyapunov exponent λ_0, which has been obtained by additionally integrating the corresponding partial linearization of the drive system in Eqs. (3.7). The plots, shown in Fig. 3.14, support a very good agreement of the curves throughout a range of α-values corresponding to the properties of the laser diodes in the experiment. For comparison of σ and λ_0, the axes are scaled by a constant factor proportional to the intensity of the finite-time fluctuations of the sub-Lyapunov exponent. Interestingly, this scaling factor emerges to be largely independent of the pump current resulting in the proportionality $\sigma \propto \lambda_0$. For $\alpha = 2.5$, a clear region of strong chaos appears where the zero-crossings of the sub-Lyapunov exponent are reproduced by σ. A lower value of the linewidth enhancement factor α leads to the avoidance of positive sub-Lyapunov exponents. From the matching between the sigma curves obtained experimentally and numerically, we can deduce that the semiconductor laser used in our experiment has a linewidth enhancement factor of $\alpha = 2.1$.
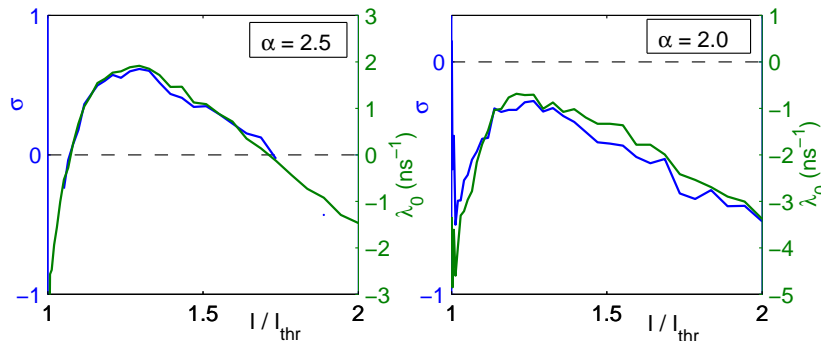
Figure 3.14: Comparison of automatically extracted value of the slope σ from distribution functions with the sub-Lyapunov exponent for $\alpha = 2.5$ (a) and $\alpha = 2$ (b). The figures show a very good agreement between σ and λ_0 with scaling factor 3ns^{-1} (a) and 5ns^{-1} (b).

This could represent a new technique to estimate the α parameter of the laser.

3.5

Summary and conclusions

We presented an optical consistency experiment based on a semiconductor laser driven by a chaotic optical signal. This chaotic drive originated from the time-delayed feedback of the laser itself, and is stored in a long fiber loop to allow for an exact repetition of the drive. The design of the experiment permits the use a non-scalar drive, in which all optical features like bandwidth, intensity or phase dynamics are kept and replayed again.

By comparing the responses of the laser, we observed that the semiconductor laser undergoes transitions from consistent to inconsistent responses and back when the pump current is increased. Such transitions are a characteristic that depends on the system employed, and other lasers may show a single transition or none at all. We relate the consistent response of the laser to a regime of weak chaos, whereas in a strong chaos regime the responses are inconsistent. We also confirmed that the consistency correlation serves as a good indicator of the different consistency regimes.

The key signature of consistency relies on the sub-Lyapunov exponent of the system, closely related to generalized synchronization. While, to date, no experimental access to the sub-Lyapunov exponent of the system existed, we have developed an experimental method to directly measure the consistency properties for high optical and dynamical bandwidth drives. By means of analysis of transverse distribution functions, we could extract σ, a direct indicator of the sub-Lyapunov exponent. The experimental method as well as the time series analysis technique are general for the synchronization of nonlinear oscillators so that, in principle, they can be applied to any type of laser or dynamical system with chaotic dynamics.

Complementary, we numerically simulated the corresponding scheme using the Lang-Kobayashi rate equations, and applied the same analysis in order to corroborate the experimental assumptions. We found consistent results for the slope σ of the distribution functions throughout all embedding dimensions and embedding delays. We further confirmed the proportionality $\sigma \propto \lambda_0$ by comparison with the directly calculated sub-Lyapunov exponent from the linear equations of motion. These findings corroborate the theoretical arguments that extend the theory for discrete maps to continuous systems, and demonstrate the robustness of the presented method. The simulations also unveil the dependence of the σ curve on the linewidth enhancement factor α, confirming consistency as a property of the laser. The good agreement between the sigma curves obtained experimentally and numerically suggest a sensitive dependence on the α factor. This phenomenon could be used to estimate the α factor or contrast its value obtained from other methods [102]. Employing the combination of experimental and theoretical methods, we provided a valuable understanding and characterization of consistency in driven systems. Given the ubiquity of "drive-response" schemes in nature, the relevance and implications of our results can be extended to dynamical systems even beyond the field of photonics.

Consistency of a semiconductor laser system to input pulse trains

> "An approximate answer to the right problem is worth a good deal more than an exact answer to an approximate problem."
>
> John Tukey, Mathematician.

4.1
Introduction

In the previous Chapter, we introduced the concept of consistency with an experiment in which a laser system is driven by its own dynamics, playing at the same time the role of drive and response system. The external drive consisted of its own delayed feedback dynamics, exemplifying a new particular way to study the effect of complex drives on laser systems. However, this scheme can be extended to the more general case in which the input drive is an external signal, not necessarily generated from the system. In this complementary approach, an external perturbation is introduced while the laser system with feedback exhibits its own autonomous complex dynamics. The compulsory question here is: can the system under these conditions still respond consistently? If so, what are the mechanisms that lead to a consistent behavior?

Previous studies have investigated the effect of external driving on nonlinear systems [53, 83, 84, 103, 104, 105, 106, 107, 108, 109]. By means of an external drive in the form of a continuous and smooth or periodic waveforms, phenomena like stochastic resonance, synchronization or entrainment were observed [53] when the system was originally in a fixed point, periodic orbit or a limit cycle. In other cases, the drive was a chaotic signal leading to similar phenomena [52, 83]. But much less is known when a nonlinear system, operating in a complex excitable-like dynamics, is driven by non-periodic short pulses. Particularly, it is

still to be explored how the consistent response depends on the characteristics of the train of pulses, like the precise timing of a certain pulse (the temporal pattern), the average number of pulses per unit time (the pulse rate) or the amplitude of the pulses.

In this Chapter, we address the consistency properties with the laser system being in its complex chaotic regime, driven by an external train of pulses. The semiconductor laser is subject to delayed optical feedback, and operates in the regime of Low Frequency Fluctuations (LFFs). The LFF regime is characterized by a complex chaotic behavior of the light intensity on a fast timescale while, on a slow timescale, the dynamics manifest a pattern of drastic dropouts of the emitted light intensity. Studies on the effect of an external modulation to the pump current in the LFF regime have already been presented, demonstrating that a periodic drive affects the nonlinear properties of the delay system [7, 103, 104, 105, 106, 109, 110]. With our approach, we aim to investigate the feasibility of stimulating the dropouts by means of an external non-periodic pulsed drive. Different pulse distributions and pulse amplitudes are utilized to analyze the existence of optimum conditions for a consistent response. Thus, this study can be seen as a step forward in the characterization of the basic principles in the drive-response schemes with an active excitable background.

The parallelism between our approach and some aspects of the neural scenario, makes it of special interest [79, 107, 108, 111, 112, 113]. Neurons in the brain communicate with short-lasting chemical and electrical signals, processing the information in an oscillating environment which is permanently active [55, 114]. In this sense, the results presented in this Chapter allow for a better understanding of the requirements for a consistent performance under complex conditions, which in turn will allow for more efficient bio-inspired techniques of information processing like Reservoir Computing [115].

The investigations were initiated by Jordi García-Ojalvo, Javier Buldú and Ingo Fischer. The experiments and data analysis were carried out by Neus Oliver in close collaboration with Thomas Jüngling and supervised by Ingo Fischer. The simulations were carried out by Thomas Jüngling. Daniel Brunner contributed to make the pump current modulation possible.

4.2

Experimental realization

Our experimental system consists of a laser diode, subject to delayed optical feedback, and to external pump modulation in the form of electrical pulses, as depicted in Fig. 6.2. The laser is an Eblana Discrete Mode laser, lasing at 1550nm and exhibiting a threshold current of the solitary laser of I_{th}=11.8mA. It is mounted on a board that allows for modulation frequencies up to 5GHz. The LFFs regime, in which we carry the experiments, is found to be around 12.7mA. A bias-tee allows for the modulation of the pump current. The laser light is injected through non-polarization maintaining fibers into an optical circulator, which determines input and output of the fiber loop. A 50/50 optical coupler divides the passing light. 50% of the light is directly used for detection. The remaining light enters into a polarization controller

to align the polarization state of the light with respect to the laser facet. The output of the polarization controller is connected to the input of the optical circulator, thus closing the feedback loop. The round-trip time of the light in the cavity is 50ns. The DC current can be adjusted to a precision of 10μA while the temperature of the laser is controlled to a precision of 0.01K. The laser output is detected with a photodiode of 12.5GHz bandwidth, and a digital oscilloscope with 16GHz analog bandwidth. During the realization of the experiment, the low cut-off frequency of the bias-tee can cause a discharge effect when the AC drive signal is applied to the DC injection current, partly due to the high amplitude of the modulation pulses. This effect translates into small global oscillations of the baseline of the temporal waveform, which in turn can introduce some artifacts in the consistency measurements. To avoid this error, we correct the global oscillations by subtracting to the acquired time traces their sliding average, excluding the pulses. The range of the sliding average is around $400ns$.
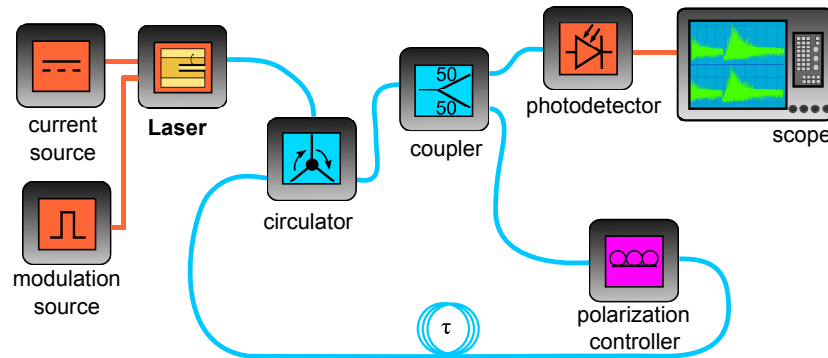

Figure 4.1: Experimental consistency setup.

When no modulation is applied, the behavior of the system corresponds to the Low Frequency Fluctuations dynamics [12, 29, 38]. This dynamical phenomenon takes place close to the solitary laser threshold, and it is characterized by cycles of a slow increase of the intensity, with fast chaotic oscillations, until a spontaneous dropout of the intensity occurs. The occurrence of the dropouts is between $400 - 900$ns, a much slower timescale than the chaotic fluctuations (typically in the sub-nanoseconds scales). Figure 4.2 illustrates a complete LFF cycle obtained from an experimental time trace. The dynamics shown are filtered to a bandwidth of 100MHz (see subsection 4.2.1). The evolution of the intensity shows fast fluctuations of the light intensity with three complete dropouts, and subsequent power-buildups phases in steps of the delay time τ.

In terms of dynamics, the LFF regime gives rise to a complex dynamical pattern with a clear timescale separation. The origin of the dropouts has been a matter of discussion and investigated from different points of view [34, 40, 41, 44, 116, 117], with a special emphasis on whether the nature of the dropouts is deterministic or stochastic [13, 40, 118, 119, 120, 121, 122]. The investigations concluded that the origin of the power drops is mainly deterministic, although noise can also influence their statistics. The mechanism leading to the LFF can be

seen as chaotic itinerancy process towards the cavity mode with the largest gain, where the trajectory gets attracted by a saddle point (anti mode) until it is repulsed back to the low gain region, causing a power drop. This chaotic itinerancy is related to the fast chaotic pulsations [43]. A look at the carrier density reveals an increase of the carriers when the dropout event takes place.
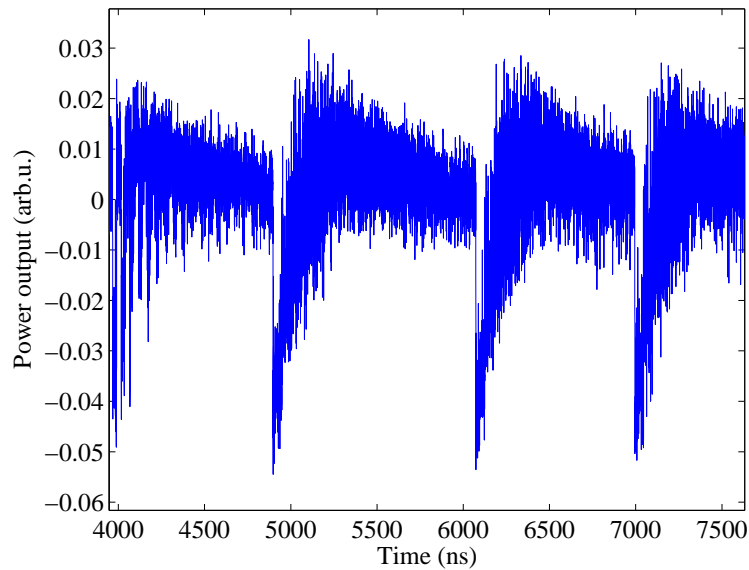

Figure 4.2: LFF cycles of a semiconductor laser with feedback obtained from experiments. The pump current was $I = 12.8\text{mA}$.

In this complex regime with excitable features, we aim to investigate the effect of an external drive with two major questions in mind: can an external stimulation induce the dropouts in a consistent manner? and what is the influence of the history of the previous dynamics? To address these questions, we inject positive electrical pulses to the laser, expecting to have an effect on the slow timescale of the system and cause a change in the carrier density like the natural dropout events do. At this point, the characteristics of the drive pulses need to be considered, such as the pulse amplitude and duration. The amplitude of the pulses is used as parameter in the following sections. For the selection of the pulse duration, we performed a qualitative investigation, in which we modulated the laser with periodic sequences of pulses, whose duration varied from 8ns to 80ns. The results showed that the duration of the pulse has a direct influence on the dropouts. A pulse too short or too long would not induce a clear dropout afterwards. In case of a triggered dropout, this would have a short duration (around 5ns) and the number of spontaneous dropouts would be more or less constant along the drive sequence, without being affected by the pulse. We observed that the best entrainment of the system was for a pulse duration between the range of 30-60ns, with slight variations. Under

such circumstance, the amount of spontaneous dropouts is significantly decreased, indicating the influence of the injected pulse in the system. These observations were in agreement with our simulations of the Lang-Kobayashi equations [101] with driving pulses:

$$
\begin{aligned}
\dot{E}(t) &= \frac{1 + i\alpha}{2} G_N n(t) E_1(t) + \kappa E(t - \tau) \\
\dot{n}(t) &= (p(t) - 1)\gamma N_{sol} - (\Gamma + G_N n(t))|E(t)|^2
\end{aligned}
\tag{4.1}
$$

where p(t) includes the injection of electrical pulses of constant amplitude w and duration s at a time t_p, so that:

$$
p(t) = \begin{cases} p & t < t_p \\ p + w & t_p \leq t \leq t_p + s \\ p & t > t_p + s \end{cases}
$$

with the following parameters: the gain coefficient $G_N = 2.142 \cdot 10^{-5} \text{ns}^{-1}$, the photon decay rate $\Gamma = 357 \text{ns}^{-1}$, the carriers decay rate $\gamma = 0.909 \text{ns}^{-1}$, the carrier density at transparency $N_{sol} = 170.7 \cdot 10^6$ and the linewidth enhancement factor $\alpha = 5$. The pump current p is defined as $p = I/I_{th}$ and set to 1.02. Feedback parameters are $\kappa = 100 \text{ns}^{-1}$ for the feedback strength and $\tau = 10 \text{ns}$ for the roundtrip time. The duration of the LFF cycle is 250ns. With these simulations, we aim to explore qualitatively the effect of an external pulse within the LFF cycle, so that the parameter values do not necessarily coincide with the values of the laser used in the experiment. A pulse induced dropout is depicted in Fig. 4.3 for a pulse amplitude of 14mV (or 0.4mA) and duration s of 10ns. In blue, the evolution of the intensity dynamics filtered to a bandwidth of 100MHz is displayed. The green curve represents the time at which the modulation pulse was injected (around 175ns), but also the adiabatic solitary emission intensity. The simulations show that the pulse induces a dropout, although it is not as pronounced as the spontaneous one taking place at 280ns. The duration of the pulse was varied in an analogous way to our experimental observations, exhibiting the best entrainment for a pulse duration equal to the delay time of the system.

To examine the possibility of pulse-induced dropouts experimentally, two different pulse distributions are used to modulate the pump current: a bimodal distribution and a uniform distribution of pulses. With the bimodal distribution, we attempt to study the existence of a sensitive and insensitive phase of the LFF cycle after the pulse as well as its dependence on the past pulses. With the uniform distribution, we aim to investigate the effect of the spacing between pulses when randomly varied following a uniform distribution. In both cases, the pulses have the same duration as the delay time of the system. This method requires a new interpretation of consistency. Now, the evaluation of a consistent or inconsistent response is confined to the dynamical features of the response system in a given time window after every pulse and throughout the replay of every train of pulses. Besides, this operation permits the distinction between inter- and intra-correlations, thus gaining a deeper insight into the conditions for a consistent and yet complex temporal behavior.
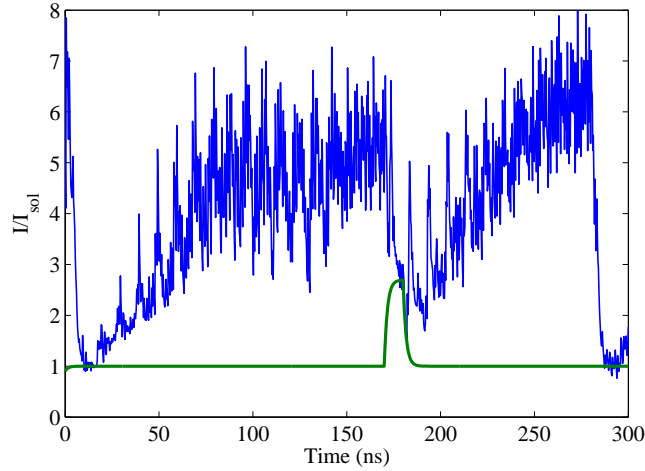
Figure 4.3: Typical LFF cycle of a semiconductor laser with feedback obtained from numerical simulations. A pulse of 14mV was introduced after 175ns.

4.2.1 A study at slow timescales

The regime of Low Frequency Fluctuations, as described in the previous section, has a slow and fast dynamics. The LFF cycle, as the power dropout and the power-buildup, is repeated in the slower timescale. To facilitate the recognition of global features of the responses to the perturbations in the LFF cycles, the fast frequency components have been filtered out. Thus, a pre-filtering to the recorded time traces is applied. Figure 4.4 (a) shows the laser response to modulation of pulses with a bandwidth of 1GHz, as acquired from the oscilloscope. Figure 4.4 (b) shows the same responses with a reduced bandwidth of 100MHz. The intensity dropouts are hidden within the fast oscillations of the system when the bandwidth is 1GHz. After the filtering, the dropouts are easier to identify and the characteristics of the individual responses, such as the depth of the dropout or the slope of the recovery, can be better compared. An extended study on the effect of filtering in the consistency of responses is presented in section 4.5.

4.3

Influence of the history of pulses: injecting a bimodal distribution of pulses

In this section, we examine two different aspects of consistency: the influence of the pulse position within the LFF cycle and the influence of the history of previous pulses. The designed train of pulses follows a bimodal distribution, so that the interval between two consecutive pulses has two possible values, each with a 50% of probability. One of the times is adjusted
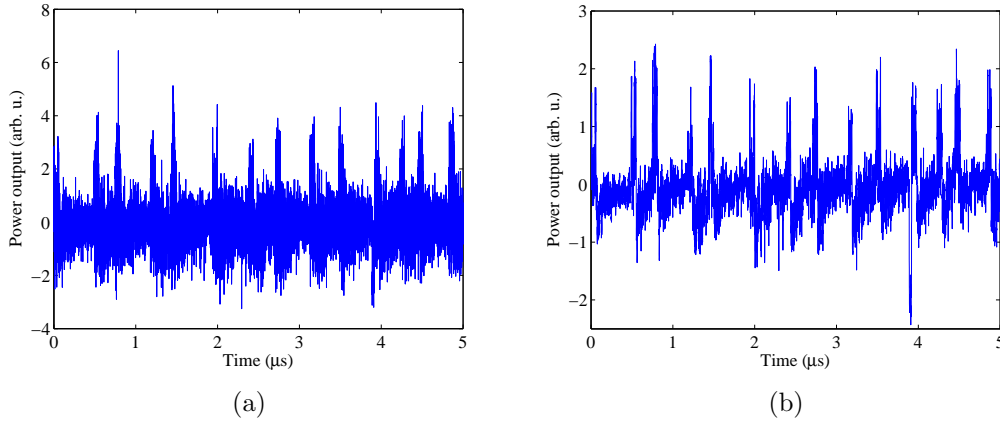
Figure 4.4: Temporal waveform of the response to input pulse trains. The amplitude of the modulation pulses was set to 25mV.

to the typical inter-dropout time of the autonomous dynamics, propitious for the stimulation of a dropout, while the other time interval is shorter and, in principle, not favorable for the pulse to induce a dropout. The bimodal modulation comprises pulses of 50ns of duration to match the delay time of the fiber loop. The pulse amplitude is initially set to 25mV, which in terms of pump current is equivalent to +1mA. Later in the study, the amplitude of the pulses is changed and used as parameter. Figure 4.5 shows the first $25\mu s$ of the bimodal modulation sequence, which has a total duration of $100\mu s$. The number of pulses contained in the train is 281.

Many features of the responses are nicely represented in persistence plots. A persistence plot is an ensemble of time traces plotted as a density plot and averaged over a certain time, 20s in our case. This is a very powerful experimental tool, since it allows to visualize up to 2.000 responses at the same time in a fast and intuitive way. Such plots can be captured directly via the oscilloscope. In order to obtain the same amount of information from numerical simulations, long computational times would be required. An example with the response of the laser to bimodal modulation is shown in Figure 4.6. The vertical axis represents the light intensity as the photodiode voltage output. The horizontal axis represents the time, 500ns per division. The color codes the frequency of the trajectory occurring at certain time-intensity coordinates, so that white means no occurrence and red means maximum frequency. Fig. 4.6 was obtained with a sampling rate of 10 GSamples/s and a bandwidth of 1GHz. To have it stabilized in time, we used a marker in the modulation sequence as a trigger. The persistence plot can be understood as a way to visualize the inter-correlation.
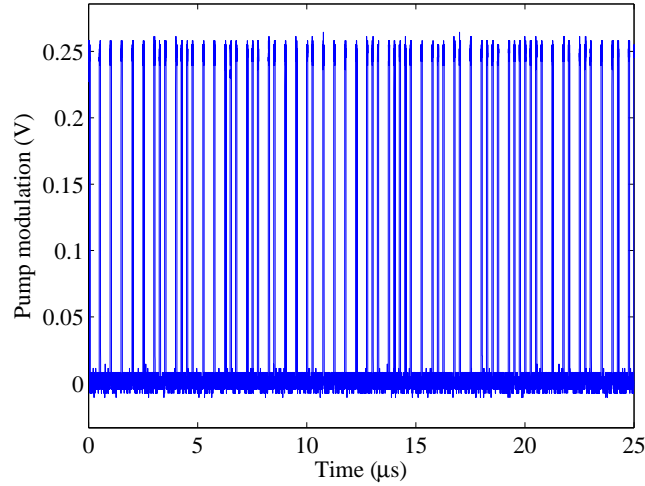
Figure 4.5: First 25μs of the bimodal input pulse train affecting the pump current of the laser system. The total duration of the modulation sequence is 100μs.
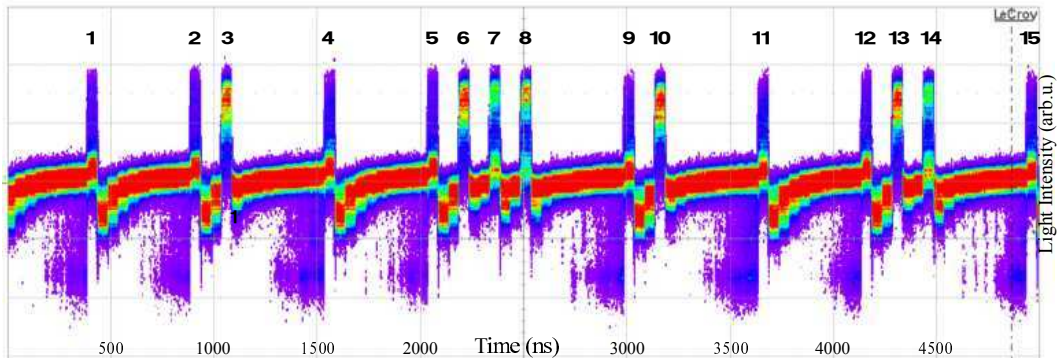
Figure 4.6: Persistence plot of the response of the laser to a bimodal modulation sequence. In this case, the two allowed interval between pulses where 150ns or 500ns. The pulse amplitude is 25mV.

In Fig. 4.6, 15 different pulse responses can be identified. The position and duration of the pulses is captured in the persistence plot as a short and relatively high elevation of the intensity from the mean. Besides, spontaneous dropouts are also identifiable. The spontaneous dropouts take place typically before the incidence of a pulse, and are represented as a lowering of the intensity with an amplitude comparable to the injected pulse's amplitude. In the figure, they show up in purple color. Remarkably, the induced dropouts are less profound than the natural ones, as observed in the simulations of Fig. 4.3.

Analyzing the responses to the perturbations in a bimodal distribution, we can classify

them into two. On the one hand, there are pulses capable to trigger a dropout after the pulse. It is the case for pulse responses 1, 2, 4, 5, 7, 9, 11, 12 and 14 of Fig. 4.6. On the other hand, there are responses that do not have a significant effect on the intensity after the pulse, but cause an elevation of the intensity during the pulse itself. This corresponds to responses of pulses 3, 6, 8, 10 and 13. We can extract from Fig. 4.6 that, although the responses are different from one pulse to another, the response to a certain pulse of the modulation sequence is consistent. In other words, responses have a higher inter-correlation than an intra-correlation.

A reason for this difference between inter- and intra-responses lies on the effect of history in the pulse responses. For instance, pulses 4 and 11 have a similar history: before each pulse there is an interval of 500ns, two pulses spaced 150ns and an another interval of 500ns. The average of responses for the two pulses is very similar since both pulses trigger a dropout consistently. If we now compare the responses to the 8th pulse and to the 14th pulse, we see that they also have a previous history in common: before the reference pulse comes a blank interval of 150ns, preceded by a pulse (7th/13th), another 150ns interval and another pulse(6th/12th). However, their responses are slightly different. Responses to the 14th seem to trigger more dropouts, whereas the responses to pulse 8th consist of an elevation of the intensity during the pulse. This can only be due to the difference between the precedents of the 6th and 12th pulse, meaning that history beyond 400ns still plays a role in the responses.

To further quantify the observations from the persistence plot, we performed the inter- and intra- correlation calculations.

4.3.1 Consistency for a bimodal distribution of drive pulses

We calculate both inter-correlation (pairs of responses only belonging to the same pulse in the sequence) and intra-correlation (pairs of responses from different pulses along the sequence) using the same global normalization procedure as introduced in Chapter 2. The analysis is intended to clarify the impact of a given pulse in the efficient stimulation of a dropout. While the intra-correlation compares the responses to all the pulses of the sequence, some of which trigger a dropout consistently and some of which do not, the inter-correlation compares the responses to a certain pulse of the drive train within the different repetitions.

For the computation of correlations, we perform 88 repetitions of the modulation sequence. The inter-pulse times have two possible values: 190ns and 500ns. The window for the calculation of the inter- and intra- correlations begins right after the pulse, so that the calculation of the correlation includes only the response of the system to the pulse, excluding the elevation of the dynamics during the pulse itself that could lead to false higher correlation values.

The pulse amplitude was varied between 8mV and 250mV. An example of the effect of the pulse amplitude on the responses can be seen from Figure 4.7. The ensemble of the 88 responses to the modulation is represented in grey, whereas, in blue, only one trial is highlighted. This visual comparison between a given trial and the whole ensemble is the basis of the calculations based on ensemble correlations. In Fig. 4.7(a), the pulse amplitude

is 25mV, whereas in Fig. 4.7 (b), the amplitude of the pulse was 79mV.
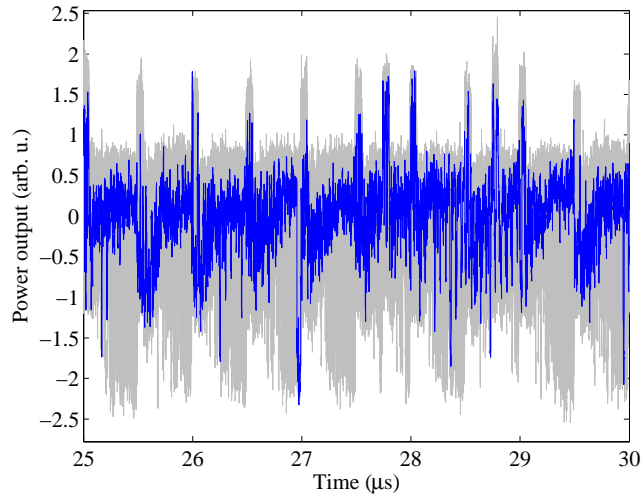
(a)
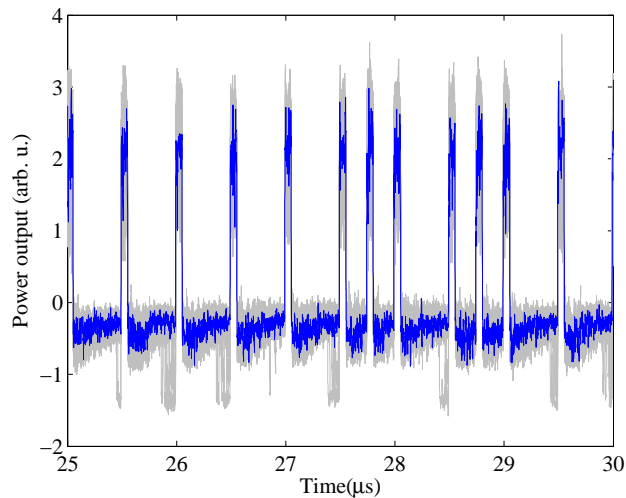
(b)

Figure 4.7: Temporal waveforms of the response to input pulse trains. The amplitude of the modulation pulses was set to (a) 25mV and (b) 79mV.

In both figures, the signatures of the pulses can be identified in the time traces, demonstrating that the two drives, comprising different amplitude pulse trains, affect the dynamics. The variability in dynamical responses seems larger for smaller amplitudes of the pulse, whereas for higher values of pulse amplitude, the responses are more confined. It is worth

noticing that the amount of spontaneous dropouts taking place before the occurrence of a pulse is significantly smaller when the pulse amplitude is big. The depth of the power-dropout is also slightly reduced when the amplitude of the pulses is 79mV.

The result of the correlation determination as a function of the pulse amplitude is shown in Figure 4.8. The curves for inter- and intra- correlation show the same trend, with an overall increase of the correlation with the pulse amplitude. For all pulse amplitudes, the correlation between responses is always higher for inter-trials than for the intra-trials, exhibiting for some amplitudes a percentage difference of up to 86%. This result agrees with the contrast observed in the persistence plot. Small pulse amplitude are non-invasive, having a non apparent influence on the dynamics. Pulses with amplitudes above the 200mV tend to control the autonomous dynamics, which reacts in a similar way to any perturbation. A local maximum around pulses of 25mV amplitude appears in Fig. 4.8. This nontrivial extremum could be due to the perfect match between the height of the pulses and the average depth of the power dropouts induced. The global increase in correlation with the pulse amplitude can also indicate that the fast degrees of freedom become more consistent as the pulse grows, not acting as additive uncorrelated noise anymore.
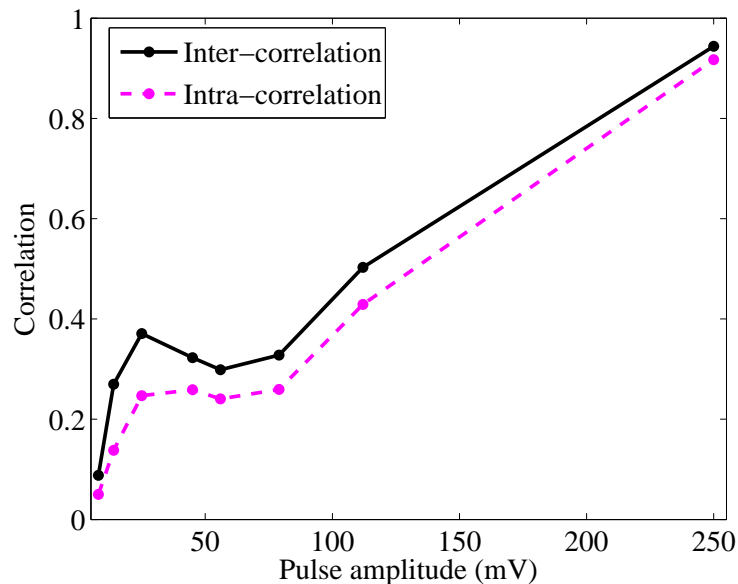

Figure 4.8: Comparison of the inter- and intra-correlation values as a function of the pulse amplitude for a modulation sequence with pulses spaced either 190ns or 500ns.

4.4

Influence of the inter-pulse intervals: injecting a uniform distribution of pulses

Another important parameter to investigate is the inter-pulse interval. To fully characterize the consistency properties, it is mandatory to know whether the time between pulses is a crucial control parameter, and how does the interval time affect the responses. We address these points by repeating the same study as described above with a pulse sequence following a uniform distribution. Now, the drive sequence consists of pulses of 50ns randomly spaced, with intervals ranging from 200ns to 500ns. The amplitude of the pulses is again varied in the study from 8mV to 250mV. The modulation sequence is depicted up to 25μs in Figure 4.9.
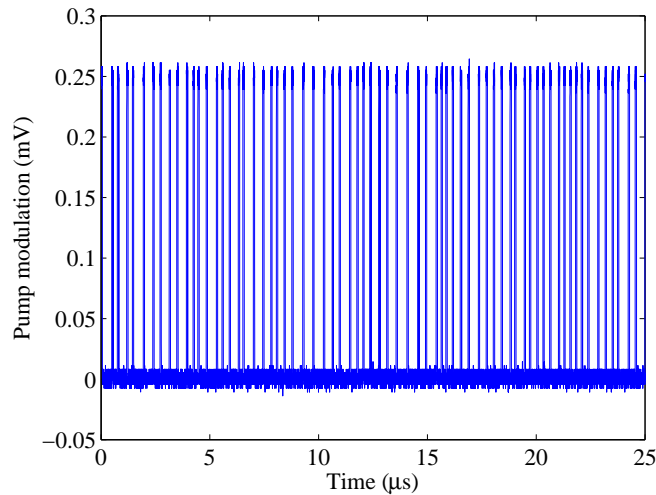
Figure 4.9: First 25μs of the uniform input pulse train affecting the pump current of the laser system. The total duration of the modulation sequence is 100μs.

The persistence plot of the time traces with modulation by a uniformly distributed pulse train is shown in Fig. 4.10. Again, the persistence mode of the oscilloscope was enabled for 20s, so that 2000 time traces are superimposed. The vertical and horizontal axes represent the light intensity and the time, respectively, while the color scale represents the probability density, from no occurrence (white) to maximum density (red). The sampling rate of the scope during the acquisition of Fig. 4.10 was 10GSamples/s with a bandwidth of 1GHz.
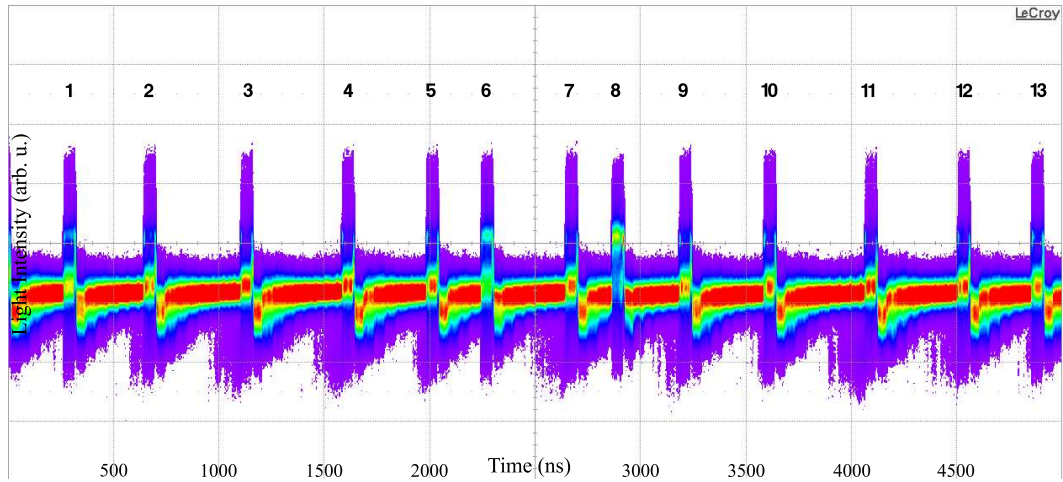
Figure 4.10: Persistence plot of the response of the laser to a uniformly distributed modulation. The pulse amplitude is 25mV.

13 pulses can be distinguished in Fig. 4.10. In contrast to the bimodal distribution of pulses, here, the responses cannot be categorized into only two types. Due to the variability of the inter-pulse times, the responses to the pulses also cover a broader range, from inconsistent to consistent response. If we look at the response to the third pulse, it shows a high degree of consistency in triggering a dropout. So does the response to the 8th pulse, which presents consistency in another behavior: the elevation of the intensity. However, the responses to the pulses 2, 4, 9 are more difficult to classify. The pulses are capable to induce a dropout, but not in a systematic manner. These are the pulses with an inconsistent response, since the outcome varies with every repetition of the sequence.

As a general observation, the inter-pulse time plays a role in the type of response. If the interval between consecutive pulses is too short, the second pulse will not lead to a dropout, but the intensity dynamics would be transiently elevated during the pulse itself. A too large interval is not favorable either, since the dropouts can then occur spontaneously. To induce a dropout, the time interval should be chosen approximately equal to the duration of a natural LFFs cycle.

4.4.1 Consistency for a uniform distribution of drive pulses

Comparatively to the study of consistency in section 4.3.1, we perform the calculations of the inter-correlation and intra-correlation for the modulation sequence following a uniform distribution of pulses (for a more detailed information see Chapter 1). The window used for the calculation has a duration of 100ns, excluding the pulse and limited by the shortest time interval.
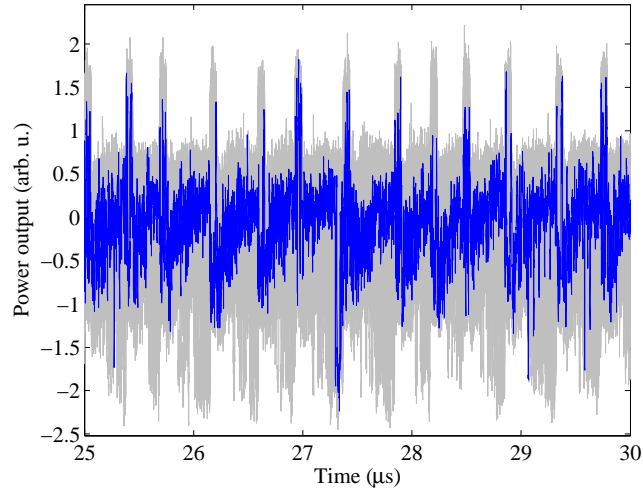
(a)
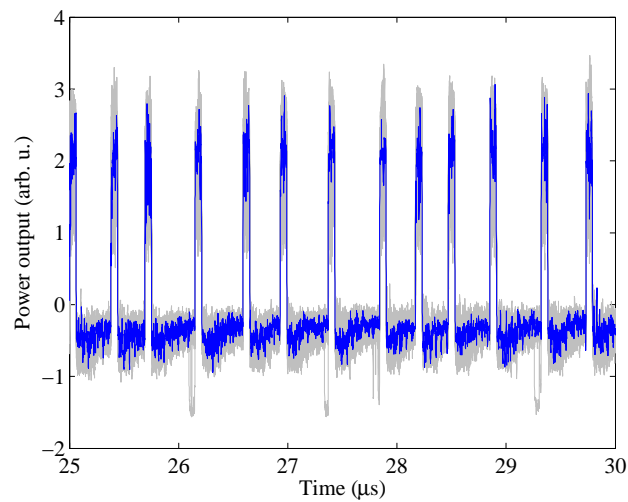
(b)

Figure 4.11: Temporal waveform of the response to input pulse trains following a uniform distribution. The grey color represents the ensemble of trajectories. The blue color highlights a response randomly selected. The amplitude of the modulation pulses was set to (a) 25mV and (b) 79mV.

As in the case of pulse train following the bimodal distribution, the amplitude of the pulse has a dramatic effect on the dynamics. In figure 4.11, we present the ensemble of the responses in grey with a given trial in blue for a pulse amplitude of (a) 25mV and (b) 79mV. Again, the differences in the type of responses between the two amplitudes are noticeable.

Even though the train of pulses is the same for both amplitudes, the case of Fig. 4.11 (b) is characterized by a strong reduction in the number of spontaneous dropouts prior to a pulse as compared with Fig. 4.11 (a). The profundity of the spontaneous power-drops is also decreased for Fig. 4.11 (b). The ensemble of all time traces reduces its range of oscillations as the input amplitude increases, reducing the difference between the single time trace and the ensemble.

Figure 4.12 depicts the correlations as a function of the pulse amplitude. The correlation values for inter- and intra- correlation increase with the pulse amplitude, showing the same tendency as for the bimodal distribution. Again, the inter-correlation is higher than the intra-correlation for all pulse amplitudes, although the contrast between them is in average smaller than in the bimodal case. The reason is due to the inconsistency of the responses to certain pulses. If a given pulse of the sequence is not capable to induce the same behavior in every repetition, the ensemble of inter-responses will be more similar to the ensemble of intra-responses, where all the experimental dynamical responses are captured. The low correlation values at small amplitudes indicate that the pulses are too small to have any impact. The amplitude of 25mV also presents a relative extreme in the correlation, proving its origin is not related to the type of modulation. The inter-correlation and intra-correlation display a plateau between 50mV and 79mV, after which the correlation values increase and become more similar.
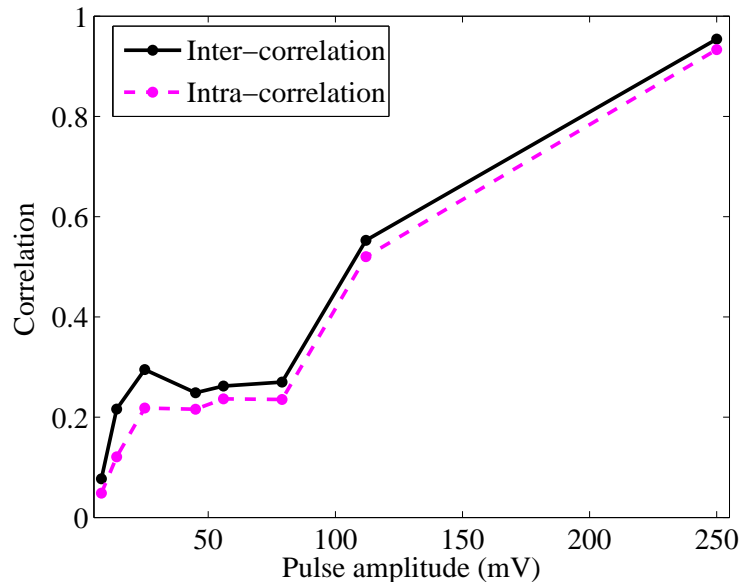

Figure 4.12: Comparison of the inter- and intra-correlation values as a function of the pulse amplitude for a modulation sequence with pulses uniformly spaced in the range [200, 500]ns.

4.5

Filtering the responses

In the previous sections, we filtered the recorded time traces to a 100MHz bandwidth. In this section, we study the effect of the bandwidth on the correlation values by varying the normalized cutoff frequency of a 2nd-order low-pass digital Butterworth filter from 20MHz to 500MHz. The different correlation values as a function of the pulse amplitude can be seen in Figure 4.13 (a) for the bimodal distribution and (b) for the uniform distribution. Interestingly, both distributions show the same trend for the different filter bandwidths. In all the presented cases, the inter-correlation is greater than the intra-correlation. The contrast between inter-correlation and intra-correlation is moderately reduced when the distribution of drive pulses is uniform. For a bandwidth of 50MHz or smaller, the local maximum around 25mV vanishes, indicating the loss of intrinsic dynamical features, and the two correlations converge for all the pulse amplitudes studied. Filtering the responses to a bandwidth of 200Mz or above causes the reduction of the contrast between inter- and intra-correlations, particularly at small pulse amplitudes. This shows that the power dropouts are less distinguishable among the fast oscillations of the dynamics. Since we are interested in preserving as many original features of the dynamics as possible, and, at the same time, we want to highlight the difference between the inter- and intra-correlations, the best compromise seems to be a filtering of 100MHz.

There is an increase of correlation values when decreasing the cutoff frequency for all the pulse amplitudes considered. This tendency suggests that the overall low correlation values can be caused by uncorrelated high-frequency components of the signal and, the more we filter, the more the uncorrelated frequencies are excluded. This effect is, however, minor for high pulse amplitudes, which indicates that the amplitude of the pulse is so large that it enslaves the system, including the high frequency components.
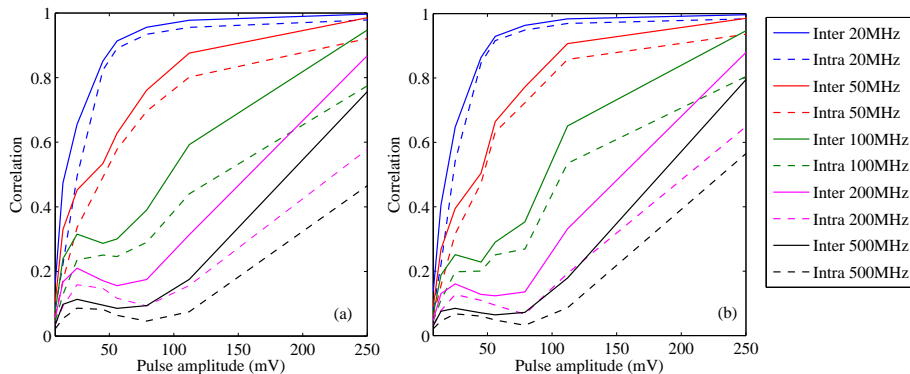

Figure 4.13: Inter- and intra-correlations as a function of the pulse amplitude for different filtering bandwidths. (a) Using a bimodal distribution of pulses as drive. (b) Using a uniform distribution of pulses as drive. Inter-correlations are plotted with solid lines, whereas intra-correlations are plotted with dashed lines. Every color represents a cutoff frequency.

4.6

Summary and conclusions

We have investigated the influence of an external drive on a semiconductor laser diode subject to optical delayed feedback. While the laser system was operating at the chaotic regime of Low Frequency Fluctuations (LFFs), we have driven the laser with two different trains of pulses, one in which the pulses followed a bimodal distribution, and one in which the pulses were uniformly distributed. Our results show that, despite its chaotic autonomous dynamics, the laser system responds in a consistent manner to the pulsed drives, reacting in a similar way when the same sequence of input trains is repeated (high inter-correlation). Nevertheless, the responses to each individual pulse of the modulation sequences maintain their own characteristics, being less similar when compared among them (low intra-correlation). We introduced new test methods to quantify consistency, such as inter- and intra-correlations, conceived for an external pulse-shaped drive. Our results unveil the importance of the temporal pulse pattern as a mechanism that can determine the consistent or inconsistent response of the system.

We have found common features between the consistency properties achieved with the two studied distribution of pulses. One of our main conclusions is that the pulse position within the modulation sequence affects the consistency of the responses. This observation is particularly noticeable in the example of the bimodal modulation train, in which consecutive pulses with a short inter-pulse time are less likely to induce a dropout, whereas pulses occurring after an interval time of 500ns tend to trigger a dropout more efficiently. However, the analysis becomes more complex if we go beyond the previous pulse, and include $n > 2$ previous pulses to the study, displaying a clear dependence of the history of the perturbation.. When the train of pulses is uniformly distributed, the range of responses is richer, reducing the contrast between the inter- and intra-correlations.

The experiments have also corroborated the existence of an optimum range of the pulse amplitude in both trains, so that the system is capable of reacting to the perturbation without being enslaved. In general terms, a range of moderate parametrical modulation amplitudes exists, in which the system shows excitability-like properties with rich dynamical features. In this range of amplitudes, the laser system can respond in a consistent manner to the pulsed drive, regardless of the complex dynamics. When the pulses are small, the effect on the dynamics is not perceptible, and it is probably hidden by noise. For large amplitude of pulses, the depth of the triggered dropouts is significantly reduced. As the amplitude of the pulses increases further, the responses of the laser tend to be more uniform or similar, until the distribution of the pulses (or their history) does not play a role anymore. The laser is then completely driven by the pulses, and reacts exactly the same way to them. These features are common to the two studied distribution of pulses. Whether the responses for the higher modulation amplitudes have also a high degree of consistency, so that the fast dynamics are also correlated, it is not yet clear.

Still, the research on consistency properties of nonlinear systems is far from complete.

All our results were obtained for pulsed drives, and the consistency properties for other modulation waveforms might provide other unexpected findings. Future work on responses to external drives might also concentrate on the investigation of consistency properties in other frequency domains, and with other forms of perturbations, like negative pulses. It should be noticed that our study is limited to a certain frequency band, and the equivalent discussion at fast time scales is not complete. The effect of the pulse duration is also a parameter to be explored in more detail. In our qualitative study, we observed that the duration of the pulse influences the induction of the power-dropouts. If the pulse is too short, it cannot provoke a clear dropout afterwards, and the probability of having an induced dropout after the occurrence of the pulse is similar to the probability of having an spontaneous dropout along the whole sequence. When the pulses have a too long duration, the response of the laser to different input train pulses is equivalent to having a short duration-pulse and the inter-correlation values are not necessarily higher. The best entrainment of the system was for a pulse duration between the range of 30-60ns, with slight variations. In that case, the amount of spontaneous dropouts is significantly decreased, proving the influence of the pulse in the system, and this fact also leads to higher inter-correlation values. Therefore, we set the width of the pulse to the delay time, aiming at short pulses, so they resemble an intense perturbation, spike-like, but still long enough to trigger dropouts. However, that is not a strict condition, and other pulse durations and even other time scales, like the relaxation time of the system, can be considered as an interesting option.

Our analysis complements the investigation of the fundamental drive-response relations presented in the previous Chapter, with the distinctive feature of introducing non-periodic pulsed perturbations as external drive. This work represents a study devoted to characterizing the response of a chaotic laser system, with a trustworthy imitation of neural dynamics at slow time scales. The presented results are therefore relevant for neuro-inspired information processing, given that, as a novelty, the system is in a complex excitable operating regime, with two timescales involved. We believe this work contributes to filling the existing gap on the conditions leading to induced consistency through pulses in dynamical systems. From a more applied point of view, the similarity of our scheme with the neural phenomenology might help to extend the state of the art bio-inspired information-processing concepts.

Consistency of an electro-optic intensity oscillator

> "Experiments should be reproducible: they should all fail in the same way."
>
> Finagle's law

5.1
Introduction

We have explored consistency of responses to different external drives in experiments based on a laser diode subject to optical feedback. The main motivation of this Chapter is to extended the study of consistency to other nonlinear configurations and to identify common properties of consistency between different schemes. Optoelectronic systems represent a perfect complementary bench-top platform to the current studies on consistency in nonlinear delay dynamical systems. Optoelectronic oscillators are becoming increasingly important as hybrid systems in communication technologies [20, 60, 123] and have been proven to be an attractive platform for optical information processing [26, 31, 46]. The standard electro-optic oscillator consists of a semiconductor laser feeding a Mach-Zehnder modulator, whose output is delayed in a fiber line, detected, amplified, filtered, and finally fed back to the modulation input of the modulator. When the filter employed is a low-pass filter, the configuration is commonly referred to as the Ikeda delayed feedback oscillator as it was used for the investigation and characterization of features of the Ikeda delay differential equation [37, 47, 49, 124, 125]. The electro-optic feedback loops with delay give rise to a wide variety of dynamical scenarios, depending on the parameters like feedback strength or filter characteristics [14, 45, 126, 127]. As a scalar nonlinear dynamical system, optoelectronic oscillators are well-studied systems in the literature, showing an excellent agreement between modeling and experiments [31, 37, 49, 124, 125, 128, 129, 130, 131]. They also present some intrinsic

advantages over all-optical systems, such as allowing for a recording of the response in the electrical domain and use it for reinjection as many times as desired. Opto-electronic systems can also function at frequencies from kHz to tens of GHz, which allows their use in applications in the fields of biology, electromagnetism, mechanics or acoustics among others. Yet these systems are more constrained in terms of chaotic regimes, exhibiting only the so-called weak chaos regime [70, 132].

Here, we investigate the consistency properties of an electro-optic intensity oscillator with first-order low pass filtering when subjected to an external forcing. A similar scheme was used for the consistency experiments of Uchida et al. [83], although, in their realizations, the feedback loop was open. Our analysis involves various drive signals, artificial and originated by the system, that lead to different responses also depending on the bifurcation parameters. This setup presents some experimental challenges and differences in comparison to the previous ones. The Ikeda oscillator is a nonlinear scalar system with a negative sub-Lyapunov exponent for all regimes, meaning that, in contrast to previous studied systems with optical feedback, it can only exhibit weak chaos. However, the optoelectronic oscillator is a system with multistability and has multiple coexisting solutions that can jeopardize the consistency [37, 47, 133]. And although it has been successfully used in the Reservoir Computing implementation [26, 82, 134, 135], their operation has been limited to conditions close to the first instability threshold. With our experiments, we want to explore the possibility to have a consistent behavior of the system with a closed loop configuration beyond the instability threshold conditions, where the dynamics are, in principle, not optimum for a reliable response. We would also like to point out that, in contrast to the experiment using an all-optical drive, in which we tested the consistency of the nonlinear laser, here we study the consistency of the entire delay system as a response system. These experiments, based on optoelectronic systems, complement our previous results, and aim to identify general features of consistency in the responses between these two nonlinear approaches: optical and optoelectronic systems.

The experiments presented in this Chapter were carried out by myself at the labs of FEMTO-ST Institute at Besançon, supervised by Laurent Larger and Ingo Fischer.

5.2

Experimental realization

The setup for the electro-optic intensity oscillator is depicted in Fig. 5.1. A semiconductor laser (JDS Uniphase monomode DFB, $\lambda = 1545$nm, $I_{th} = 17.91$mA) is used as light source. It is fiber pigtailed with an inner isolator to avoid optical feedback. The emitted light of the laser diode enters the electro-optic Mach-Zehnder modulator, acting as nonlinear element. At its output, there is a 1 by 2 90/10 optical coupler that splits the light, so that 90% of the output goes to a fiber delay line of 4.2km, leading to a delay time of $\tau_D = 20\mu$s. The light is detected by a photodiode, and converted into an electrical signal which, then, goes through an electronic amplification and a low-pass filter with a cut-off frequency of 0.52MHz. The

electrical signal is then fed back to the bias voltage of the electro-optic modulator, closing the optoelectronic feedback loop. The external drive $w(t)$ is electrically injected via a BNC connector, after the low-pass filter. The injected signal and the feedback signal experience different electronic gains before being added back to the modulator.

The light exiting the 10% branch of the optical coupler is used to observe the nonlinear function of the Mach-Zehnder in real time when plotting the output of the Mach-Zehnder $y(t)$ vs the delayed signal that enters into the Mach-Zehnder $v(t)$. The light is detected by a photodiode, and connected directly to the oscilloscope. Given that the nonlinear function is not invariant and depends on the dynamical operating conditions, the direct visualization of the transformation function is a practical tool to check the current dynamical regime (fixed point, limit cycle, chaos...), and control its deviation when the external forcing is introduced.
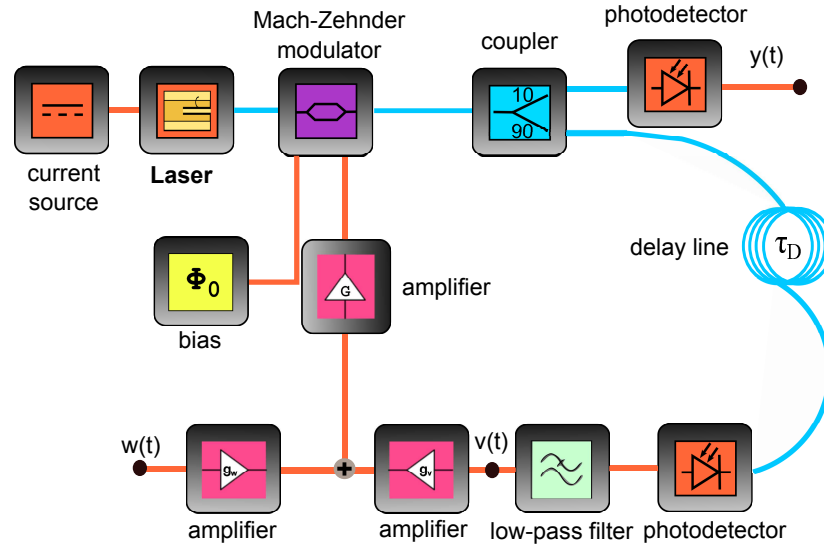
Figure 5.1: Schematic setup of the consistency setup for the electro-optic intensity oscillator.

This system can be modeled knowing that the optical power exiting the modulator follows the equation [136]:

$$P_{out}(t) = P_0 G cos^2 \left[\frac{\pi g_v v(t)}{2V_\pi} + \frac{\pi g_w w(t)}{2V_\pi} + \phi_0 \right] \tag{5.1}$$

where $v(t)$ is the feedback signal entering the Mach-Zehnder before being amplified, and $w(t)$ is the external drive term. Each signal follows a different gain path, represented by g_w and g_u. The half-wave voltage V_π (or $V_{\pi rf}$) is the voltage required to produce a π-shift in the interference condition. ϕ_0 is an offset phase that sets the operating point around which the dynamics will develop. It is tuned by an external voltage V_{DC} applied on the DC electrodes of the Mach-Zehnder. It is defined as:

$$\phi_0 = \frac{\pi V_{DC}}{2V_{\pi DC}}.$$ (5.2)

With $V_{\pi DC}$ as the DC electro-optic sensitivity. The Ikeda nonlinear delay dynamics can be modeled by a scalar first-order differential equation for the variable $v(t)$ in the case of a low-pass filter:

$$\tau \frac{dv(t)}{dt} + v(t) = SP_{out}(t - \tau_D),$$ (5.3)

where τ determines the cut-off frequency of the low pass filter $f_c = 1/(2\pi\tau)$, and S is the sensitivity of the photodiode. Combining equation 5.1 with 5.3 one obtains the following equation:

$$\tau \frac{dx}{dt} + x(t) = \beta cos^2(x(t - \tau_D) + \mu u(t - \tau_D) + \phi_0)$$ (5.4)

where $x = \pi G g_v v/(2V_\pi)$, and $\beta = \pi S G g_v P_0/(2V_\pi)$ is the weight of the nonlinearity that depends on the light power P_0 which can be tuned by changing the pump current of the laser diode.

For our Mach-Zehnder modulator, the V_π of the solitary Mach-Zehnder is 3.9V. However, if we take into account the gain factors of the circuitry, the effective V_π of the system is reduced by a factor 10, so that we often use as reference V_π'=390mV. The half-wave DC voltage is $V_{\pi DC}$=6.25V. For the estimation of β, we can use the slope efficiency of the laser, η=0.36mW/mA.

The electro-optic oscillator represents a scheme with significant differences with respect to the otherwise presented semiconductor laser systems. The instabilities and chaotic behavior are here induced through an optoelectronic feedback loop that includes a nonlinear device, the Mach Zehnder modulator; in the previous discussed systems, the laser itself acts as the source of nonlinearity. The electro-optic setup is a scalar nonlinear system whose dynamical states also differ from the all-optical systems. The Ikeda system exhibits periodic states with the appearance of higher harmonics in the evolution towards chaos. However, an analysis of the delay instabilities in this configuration showed that the Ikeda setup is restricted to weak chaos [70]. The versatility of the setup allows for different complex dynamics with a change of the filter conditions, and an operation in a broad range of frequencies from kHz to GHz. The possibility of recording the responses in the electrical domain to inject them back multiple times is a distinctive advantage for the study of consistency in the electro-optic system.

5.2.1 Methodology

The electro-optic intensity oscillator is a particular setup with challenging aspects in terms of experimental data acquisition. It is a system with a rich variety of dynamics, including multistability, but it is also very sensitive to the operating conditions. A small parameter

change can lead to significant changes in the operating dynamics. It is therefore important to make sure that, during the process of data acquisition, the parameters are not experiencing any drift.

Feedback strength and ϕ_0 are the bifurcation parameters. The feedback strength β can be controlled via the pump current source. The latter, ϕ_0, can be tuned via the applied voltage V_{DC}. A characterization of the drift showed that it is convenient to start the acquisition after a warm up time. Otherwise, the DC offset of the Mach-Zehnder can undergo a drift towards lower values at rates up to 0.75V/hour. However, one can control the changes in the dynamics with the following guidelines:

- Start the acquisition after a warm up phase of the system of about an hour of free running above laser threshold.

- Visualize the nonlinear function of the Mach-Zehnder with the oscilloscope. Any change in the dynamical regime affects the shape of the nonlinear function, so that it allows to keep track of the current dynamical state. This is of particular interest when injecting modulation on and off, since the modulation can cause the jump to another dynamical branch, and can be identified from the nonlinear function.

- Inject a signal (triangular, sawtooth) in an open loop configuration, and measure the amplitude of the output of the Mach-Zehnder. If the parameters have not drifted during the experiment, the measured amplitude should remain constant.

- Obtain the bifurcation diagram before and after the realization of the experiment. If they do not coincide, it indicates that the conditions during the experiment changed.

5.3

Dynamics without modulation

The opto-electronic oscillator exhibits a large dynamical diversity, as has been already shown and discussed in the literature on the topic. The system can exhibit periodic behavior but the complexity of its dynamics grows as the feedback strength increases. In the following, we show examples of the evolution from stable behavior to chaos with the bifurcation parameters.

5.3.1 Changing β: from fixed point to chaos

The most common bifurcation parameter in the electro-optic intensity oscillator is β. As the weight of the nonlinear function, it depends on the output power of the laser diode P_o, which can be easily tuned via the corresponding the pump current. To observe the changes in dynamics when varying the parameter β, we fix V_{DC} and change the pump current starting from a fixed point (steady state emission) to chaos. Nevertheless, the bifurcation sequence also depends on ϕ_0 (or V_{DC}) value.

The autonomous dynamical regimes for pump currents from I=23.69mA to I=31.01mA are shown in Figure 5.2 for a V_{DC} of 9.09V. The plots displayed in the left column show the experimental time traces for different acquisition conditions. The right column contains the experimental representations of the nonlinear transformation performed by the Mach-Zehnder for the same operating points. Plots (a) and (b) were acquired at a pump current of I=23.69mA, showing the fixed-point behavior of the system. Plots (c) and (d) were acquired just beyond the first bifurcation towards periodic dynamics, I=26.29mA, exemplifying the onset of periodic oscillations. The regime of squarewave oscillations is illustrated in figures (e) and (f), for a pump current of I=26.93mA. The oscillations have a periodicity of $2\tau_D$. This is the usual case when the operating point is along the negative slope of the transfer function of the Mach-Zehnder, as confirmed by the nonlinear function plotted in (f). The last pair of plots (g) and (h) show developed periodic oscillations along the negative slope, with a nonlinear function showing a slight hysteresis.

Figure 5.3 depicts the dynamical features for pump currents ranging from I=35.08mA to I=45.68mA. Figure (a) shows a bifurcated solution of period 4 dynamics, with its corresponding nonlinear function (Fig. 5.3 (b)). As β is further increased, multistable solutions develop. The period doubling cascade leads to period-2-chaos dynamics (plot (c)) and higher harmonic solutions (plot (e)). Eventually the system evolves to fully developed (global) chaos (Figures (g) and (h))[37, 47]. Every bifurcation route undergoes successive bifurcations depending on the operating conditions, and multistable attractors are formed.

5.3.2 Changing β and ϕ_0: the bifurcation diagrams

The bifurcation diagrams are an advantageous way to have a visual summary of the qualitative behavior of the system as the control parameter is varied. The period doubling cascade preceding the onset of chaos is represented iterating for every value of β. In the bifurcation diagrams, the pump current is scanned while the bias voltage V_{DC} applied to the electrodes of the Mach-Zehnder is kept constant. To obtain these diagrams experimentally, the bifurcation parameter β is slowly tuned with a triangular signal (period of $\sim$ 1s) that controls the pump current of laser diode. The amplitude of the triangular signal serves to determine the dynamical range covered by the diagram, so that an amplitude of $1V$ allows for a scan of the pump current of the laser from 25mA to 45mA. Since the characteristic time scales of the dynamics are much faster than the period of the triangular signal, the diagram can be easily obtained when many points are sampled along the scan.

Figures 5.4 and 5.5 show the bifurcation diagrams acquired as V_{DC} is increased. From these diagrams, many interesting features of the system can be extracted, and the diversity in the diagrams evidences the rich dynamical scenarios and the possible routes to chaos. In most cases, only the beginning of the period doubling cascade up to period 8 is observed, followed by a domain of higher harmonics that coexist with chaos.

The electro-optic intensity oscillator is a system that can exhibit hysteresis; thus, the dynamics displayed when β is increased can differ from those shown when β is decreased, resulting in an asymmetric bifurcation diagram. This is the situation in the bifurcation
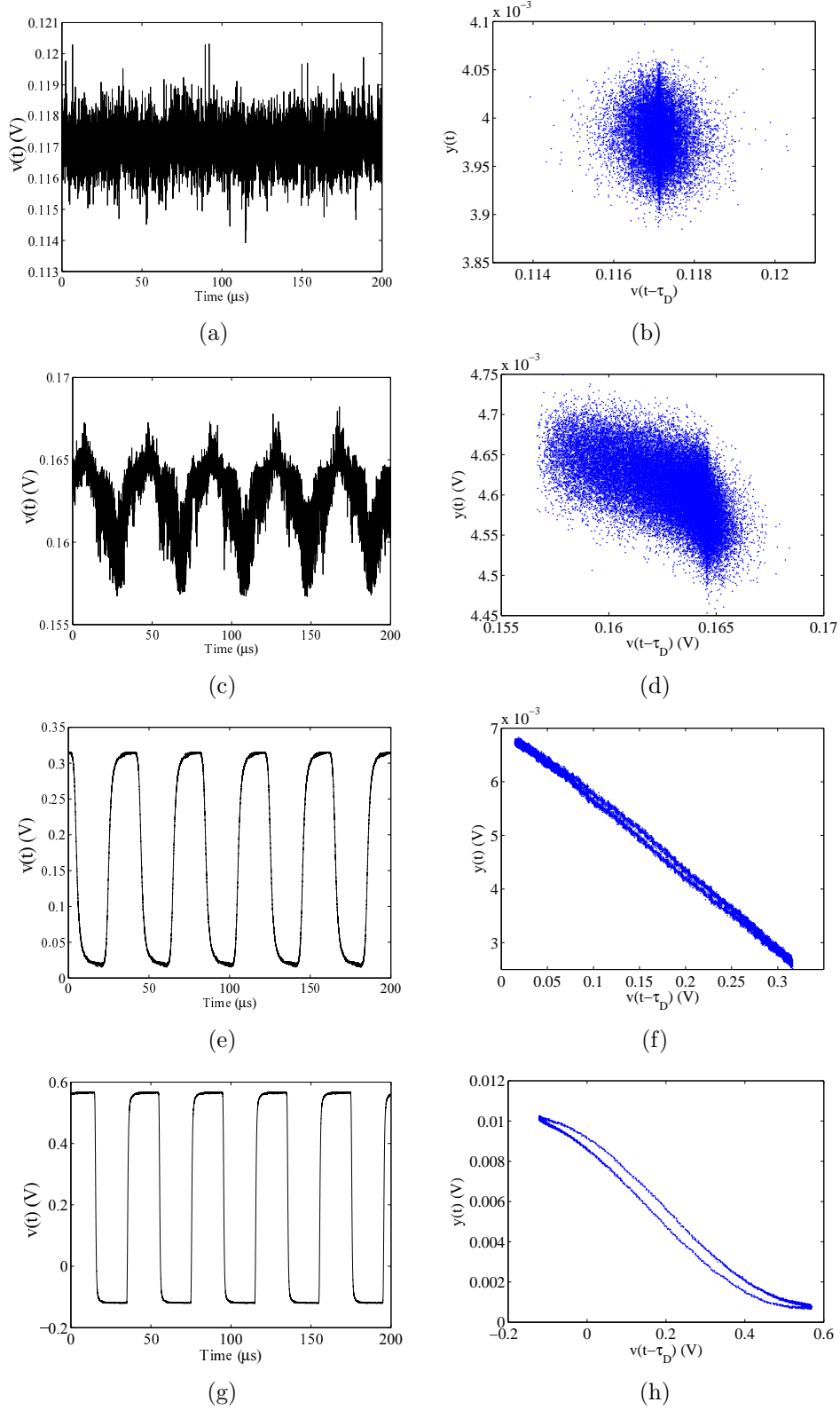
Figure 5.2: (a) Time trace and (b) nonlinear function for I=23.69mA.(c) Time trace and (d) nonlinear function for I=26.29mA.(e) Time trace and (f) nonlinear function for I=26.93mA.(g) Time trace and (h) nonlinear function for I=31.01mA.
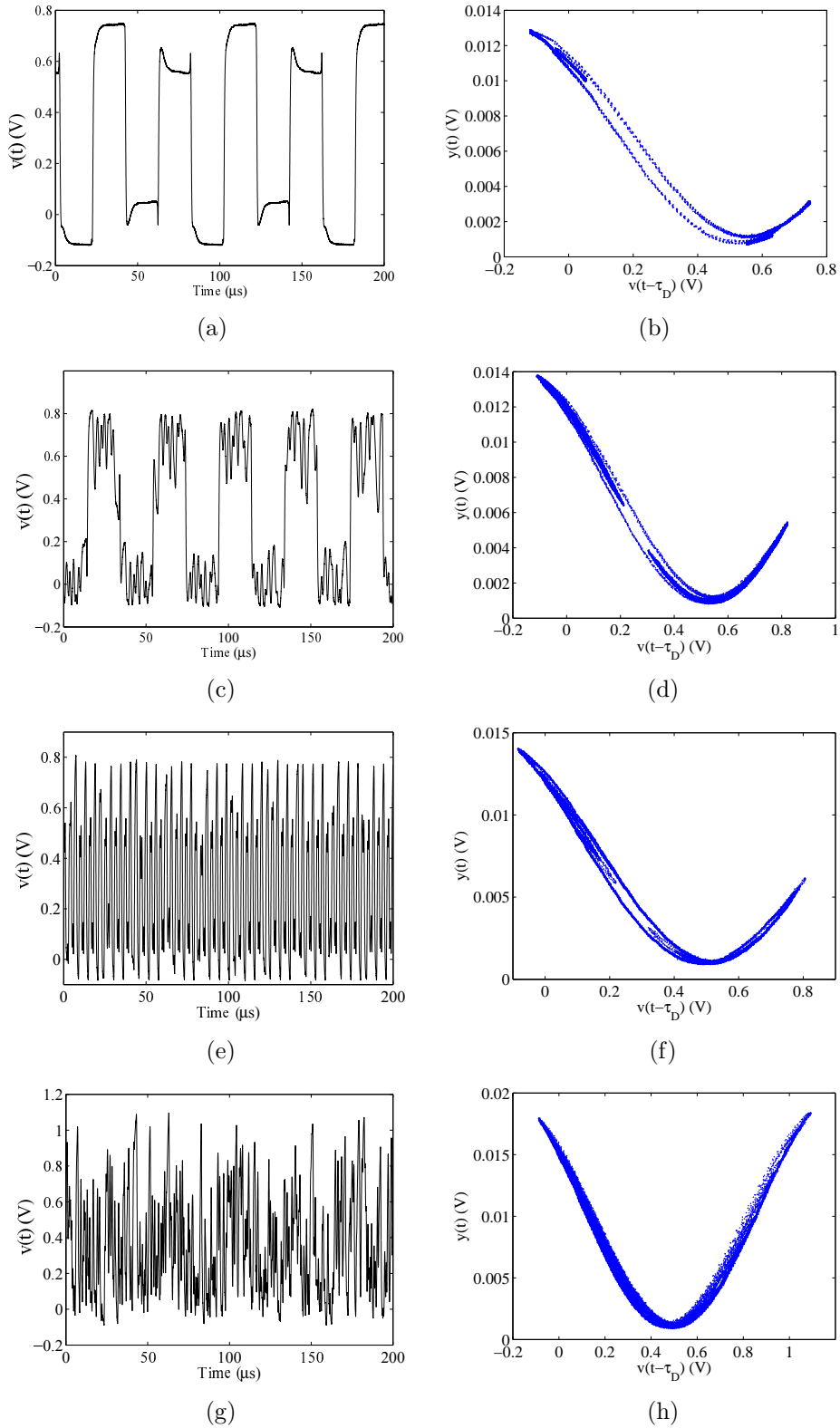
Figure 5.3: (a) Time trace and (b) nonlinear function for I=35.08mA.(c) Time trace and (d) nonlinear function for I=37.03mA.(e) Time trace and (f) nonlinear function for I=38.64mA.(g) Time trace and (h) nonlinear function for I=45.68mA.

(a) V_{DC}=0V.

(b) V_{DC}=1V.

(c) V_{DC}=2V.

(d) V_{DC}=3V.

(e) V_{DC}=4V.

(f) V_{DC}=5V.

(g) V_{DC}=6V.

(h) V_{DC}=7V.
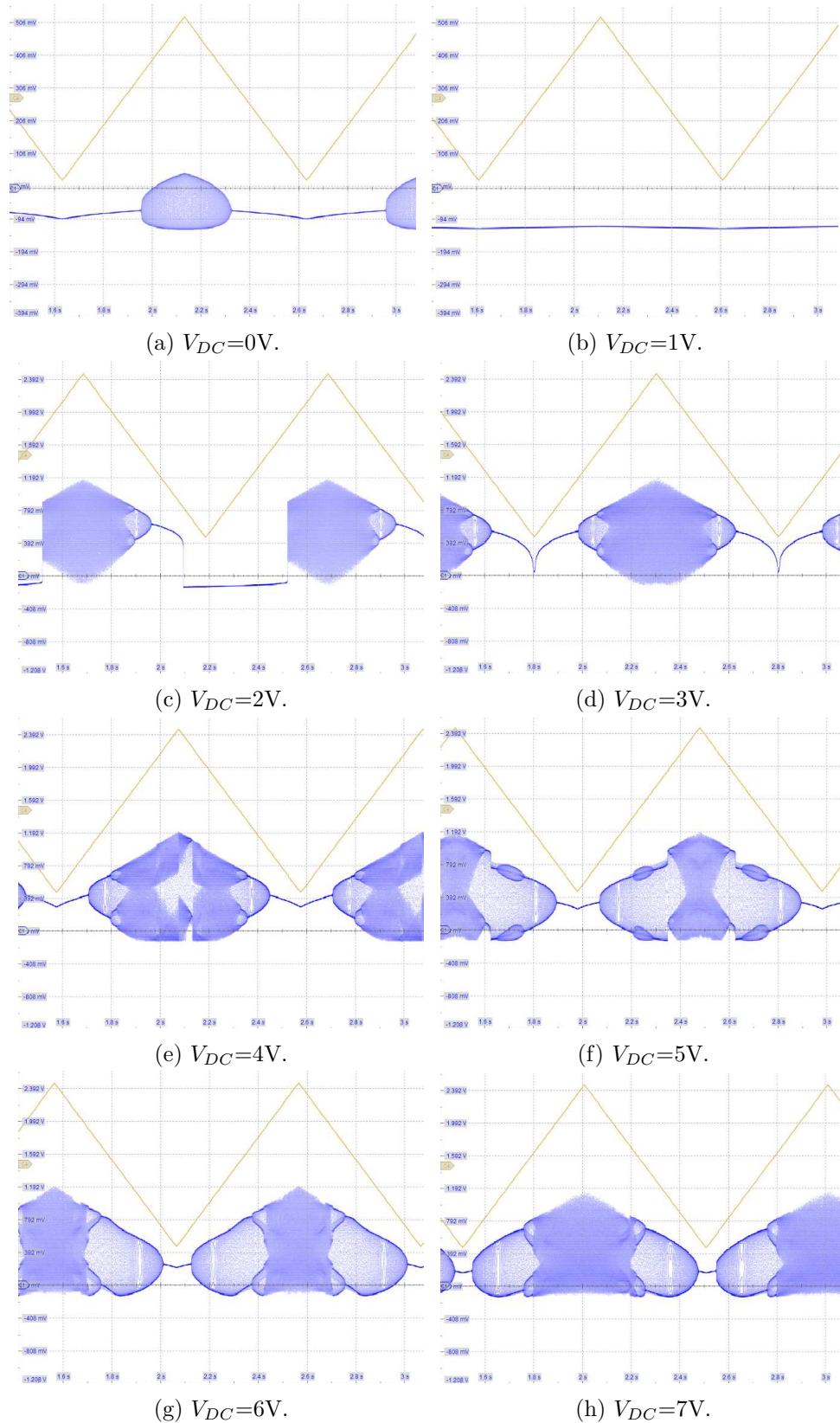
Figure 5.4: In blue, the bifurcation diagrams acquired for DC voltage values ranging from 0 to 7V. The yellow curve represents the triangular signal controlling the power supply of the laser.

(a) V_{DC}=8V.

(b) V_{DC}=9V.

(c) V_{DC}=10V.

(d) V_{DC}=11V.

(e) V_{DC}=12V.

(f) V_{DC}=13V.
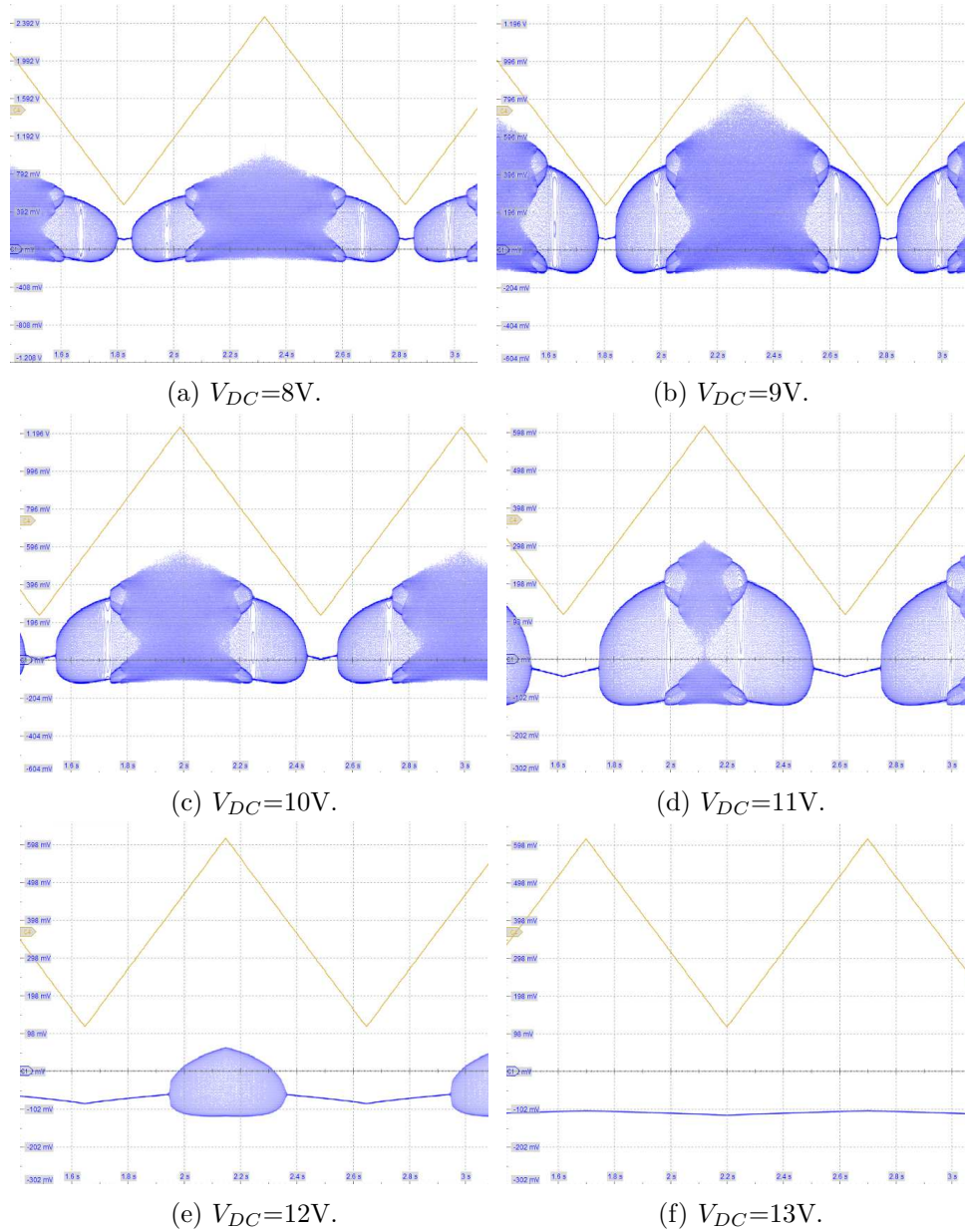
Figure 5.5: In blue, the bifurcation diagrams for V_{DC} from 8 to 13V are depicted. In yellow, the triangular signal controlling the power supply is shown.

diagrams (c), (e), (f) and (h) from Fig. 5.4. Dynamical scenarios with hysteresis can affect the occurrence and interpretation of consistency in the responses.

The comparison between Fig. 5.4(a) and Fig. 5.5(e) or Fig. 5.4(b) and Fig. 5.5(f) clearly shows that the sequence of bifurcation diagrams is repeated after approximately 12V. This is in agreement with the half-wave voltage, measured to be $V_{\pi DC} = (6.64 \pm 0.01)$V. Even though a parameter drift can induce changes in the current operating conditions, the succession of bifurcation diagrams shown in figures 5.4 and 5.5 is preserved.

Given the amount of information included in the diagrams, the bifurcation diagrams also represent a helpful way to choose the operating conditions, and to keep track of the dynamical changes due to parameter drift. The bifurcation scenario remains invariant in the range of DC voltages (8-10)V, and characterized by the period doubling cascade route to chaos, as the ones illustrated in Figures 5.2 and 5.3. Under these voltages, the diagrams do not present hysteresis either. Consequently the operating conditions displayed in Fig. 5.5(a)-(c) are chosen for the realization of the experiment. In the following, we rely on the bifurcation diagrams, and the nominal DC voltage value is used as orientation in the experiments only.

5.4
Consistency with an external drive

In this section, we study the effect of an external drive on the autonomous dynamics of the electro-optic setup, and measure the consistency through correlations of responses. The methodology consists of the repeated injection of modulation signals with a blank time ($\geq 600\mu$s) in which the system relaxes to its autonomous dynamics.

Blank times are extremely important. The closer the system is to a bifurcation, the more time it needs to return to its autonomous dynamics. If those are not reached, the consistent behavior will not be achieved either. For our consistency investigations, it is desirable to operate sufficiently far away from the bifurcations.

The amplitude of the drive signals is referenced to the V'_π=390mV of the system. However, that does not take into account the amplitude of the drive signal with respect to the amplitude of the autonomous dynamics. To do so, the gains experienced by the injected signal $w(t)$ and the feedback signal $v(t)$ need to be considered. The voltage applied to the Mach-Zehnder can be written as:

$$u(t) \simeq G[g_v v(t) + g_w w(t)] = G g_w [\frac{g_v}{g_w} v(t) + w(t)] \tag{5.5}$$

which allows to write the amplitudes referenced to the modulation, and where the proportion g_v/g_w is approximately 0.52.

Three different types of drives are used in our investigations: an harmonic waveform, a pseudo-random sequence of pulses, and recorded autonomous dynamics. We start the experiment with an harmonic waveform whose frequency is related to the frequency of the higher harmonics of the system. Such signal can contribute to characterize how the Ikeda

system adapts to a smooth periodic signal, and represents a good starting point to identify features in the responses like transient times. Given that it is an harmonic drive without structural differences among periods, it is also interesting to see how different the inter- and intra-correlations in this case are.

The second drive employed consists of a pseudo-random sequence of pulses, similar to the study performed in Chapter 4. This modulation can contribute to identify similarities between the two systems, and to analyze the effect of a short perturbation in a delay system with different complex dynamics.

Finally, we use recorded waveforms from the autonomous system running in closed loop. The purpose is to examine whether the nonlinear response of the Ikeda system is more consistent when the drive is a waveform generated by the system itself, and to observe the differences with respect to the other forms of drives. In the following, the time traces displayed correspond to the detected delay signal $v(t)$.

5.4.1 Harmonic drive: the starting point

We start our investigations with an harmonic drive to characterize the response of the intensity oscillator to a smooth periodic signal with a frequency of the order of the fast oscillations in the system. In particular, the modulation consists of a sine waveform of $200mV_{pp} < V'_\pi$ and a frequency of 275kHz, which compared to the fundamental frequency of the square waves defined by $1/2\tau_D$=25kHz, corresponds to the 11th harmonic of the system. The harmonic modulation sequence has a total of 80 periods, which will be used to distinguish between inter- and intra-correlations. The blank time added between repetitions of the modulation has a duration of 600μs. The bias voltage V_{DC} is set to 9.09V, and the conditions are checked to be the same before and after data acquisition and similar to the case of Fig. 5.5(a)-(c).

Figure 5.6 illustrates the influence of the sinusoidal drive on the dynamics of the system. The plots (a), (c) and (e) correspond to the experimental time traces under modulation for increasing values of β. The sinusoidal drive is also represented in black color with an offset to be distinguishable from the waveforms. In every plot, 10 dynamical responses to the repetitions of the drive are depicted on top of each other. The plots (b), (d) and (f) represent the recovery of the system to its autonomous dynamics during the blank time for the same conditions as plots (a), (c) and (e).

Fig. 5.6(a) and (b), acquired for I=26.93mA, exemplify the situation in which a system with periodic dynamics receives an external harmonic, forcing of higher frequency. The system adapts easily to the driving, after a transient time that equals more or less the delay time τ_D. Then, the systems responds in the same way to every repetition of the drive. When the modulation is switched off, as depicted in Fig. 5.6 (b), the system goes back to the original oscillations of smaller amplitude at the fundamental frequency, with traces of the forced frequency visible on top. For I=35.08mA, the autonomous system is not in the fundamental periodic state anymore, but in a period 4 oscillation. In Fig. 5.6(c), the time traces exhibit oscillations at the same frequency as the drive, but with variations in amplitude that are consistent between trials, and related to the period 4 oscillations. When the modulation is

removed, the oscillations recover their amplitude but preserve the periodicity imposed by the drive. This could indicate a scenario close to a bifurcation, in which the dynamics either needs more time to regain the autonomous operation or will never do. The two plots (e) and (f) were obtained at a pump current of I=37.03mA, so the system without modulation was in a period-2-chaos state. With the injected drive, the 10 responses start to synchronize after a longer transient of 80μs. Then, the forced dynamics shows alternations in amplitude within a period of the modulation. Although the match between the repetitions is not perfect, the general behavior (and especially the phase) are preserved, limiting the range of the oscillations. During the blank times, the synchronization is lost but the irregular fluctuations are maintained at the drive frequency.
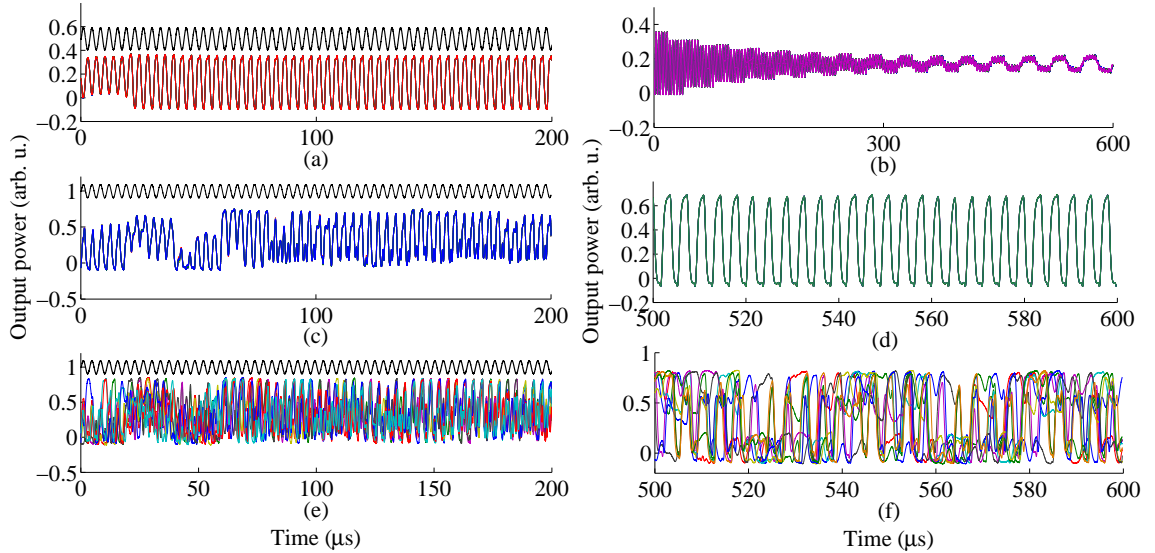
Figure 5.6: (a) Experimental time traces under modulation and (b) time traces during the blank time for I=26.93mA; (c) experimental time traces under modulation and (d) time traces during the blank time for I=35.08mA; and (e) experimental time traces under modulation and (f) time traces during the blank time for I=37.03mA.

The computation of inter- and intra-correlations between the responses of the system to the sinusoidal modulation provides a better insight into the consistency for different dynamical conditions. The result of the calculation of correlations is shown in Fig. 5.7. The dotted vertical lines divide the dynamical scenarios of the system, although given the jumps between multiple stable dynamical solutions, some boundaries cannot be properly defined. Multiple realizations show that the trend of the curve is more or less invariant of the ϕ_0 parameter. When the system is in a steady state or periodic oscillations regime, the response to an harmonic forcing is consistent; the system adapts to the modulation as the high inter- and intra-values indicate. When the system has entered into chaotic dynamics, the response is not consistent anymore, and the correlations drop drastically. However, a regime in which

the transition between consistent to inconsistent response occurs can be defined. In this regime, the autonomous dynamics correspond to period doubling, period 4, or even period 2-chaos and their pump currents fall within the range of (30-37.5)mA. In this area of the transition, the system preserves partially its autonomous dynamics while displaying signs of the modulation frequency. Here, the contrast between inter- and intra-correlation is also the most pronounced. This is due to the fact that the remaining consistency is related to the generated temporal pattern of the responses, which displays differences from one period to another of the harmonic drive (see Fig. 5.6 (c)).
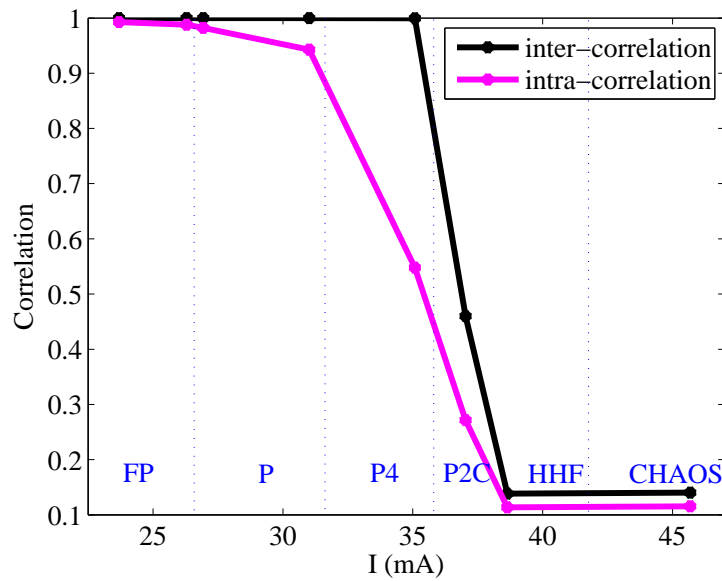
Figure 5.7: Correlation as a function of the pump current I for an harmonic modulation of $200mV_{pp}$. The dotted lines divide in an approximate manner the different dynamical regimes found at different I. FP: Fixed Point; P: Periodic, P4: Period 4; P2C: Period-2-chaos; HHF: Higher Harmonic dynamics; Chaos.

5.4.2 Pseudo-random pulse distribution: does the timing of a pulse matter?

A pseudo-random distribution of pulses might have a different impact on the dynamics as compared with the harmonic modulation. The sinusoidal drive, as a smooth signal, can enslave the system totally or partially depending on the pump current. The correlations display an abrupt transition towards inconsistent behavior as the bifurcation parameter β is increased. In either case, the dynamics is affected by an adjustment to the oscillation frequency of the drive. With a drive in the form of a sequence of random pulses, it is intriguing to know what dynamical phenomena a short pulse induces in the system, and more importantly, whether it does it consistently. The randomly spaced pulses also contribute to

investigating further the role of the temporal timing of the perturbation, as shown in the study presented in Chapter 4.

The amplitude of the pulses is set to 300mV (again below the V'_π=390mV of the Mach-Zehnder). The total duration of the sequence is 22ms, and the duration of the blank time between trials is 3.6ms. The pulse duration is set to 5μs, so that it represents a perturbation of relatively short duration at the different dynamical regimes explored. and the total sequence includes 99 randomly spaced pulses. Every modulation sequence and blank is repeated 77 times. The β parameter is employed as bifurcation parameter, keeping ϕ_0 fixed at V_{DC}=5.34V. But more important, we made sure that ϕ_0 did not drift between, before and after the data recording, and based the selection of V_{DC} on the shape of the bifurcation diagram.

Some dynamical features are depicted in Fig. 5.8. The plots (a) and (d) represent numerous experimental time traces under the pulsed modulation, also depicted as the black curve and shifted with an offset for a better visualization. In Fig. 5.8(a), the responses to the 77 repetitions of the drive, obtained for a pump current of I=27.00mA, are shown. Such responses overlap almost perfectly, displaying a power drop during the occurrence of the pulse. Further observations indicate that this power drop can turn into a power elevation depending on the operating conditions defined by the slope of the nonlinear function. For lower modulation amplitudes, the drop might not appear. Nevertheless, the most remarkable feature is the actual change in the responses from one pulse to another. The dynamical oscillations have different frequencies, and the pulse-induced transitions are consistent among the trials. Moreover, not all the pulses induce a change in the oscillations, demonstrating the dependence of the response change on the timing of the pulses. Plot (b) shows the corresponding recovery to the autonomous dynamics during the blank times. Again, the 77 acquisitions are plotted, displaying the evolution to the autonomous periodic oscillations, which is achieved after approximately 0.75ms. In plot (c), 77 responses to a randomly chosen pulse (the 44th) are depicted. The high degree of consistency is revealed at this scale, suggesting also a high value of the inter-correlation. It should be noted that the featured non-autonomous dynamics does not correspond to the well-known autonomous dynamics.

The plot (d) corresponds to stronger feedback conditions, I=37.04mA, and displays only 5 different realizations under the drive. The amplitude of the oscillations already indicates the entrance to a chaotic regime. The responses, although qualitatively similar, do not show a consistent response to the event of a pulse. The blank times reveal the existence of multistability (Fig. 5.8(e), 3 experimental waveforms). The recovered dynamics when the modulation is switched off does not always lead to a period-2-chaos (green curve), but sometimes exhibits high harmonic frequency dynamics (red curve) or something in between (blue curve). These jumps between dynamical branches are more likely to take place for pump currents above 36mA, and provoke an inconsistent response to the modulation. The blank times are designed to set similar initial conditions of the system, which does not apply if the dynamical behavior is different from trial to trial. Figure 5.8(f) shows 5 responses to the randomly chosen 44th pulse. Some responses are more similar to others, presumedly due to a common initial state, although the inconsistency is predominant.
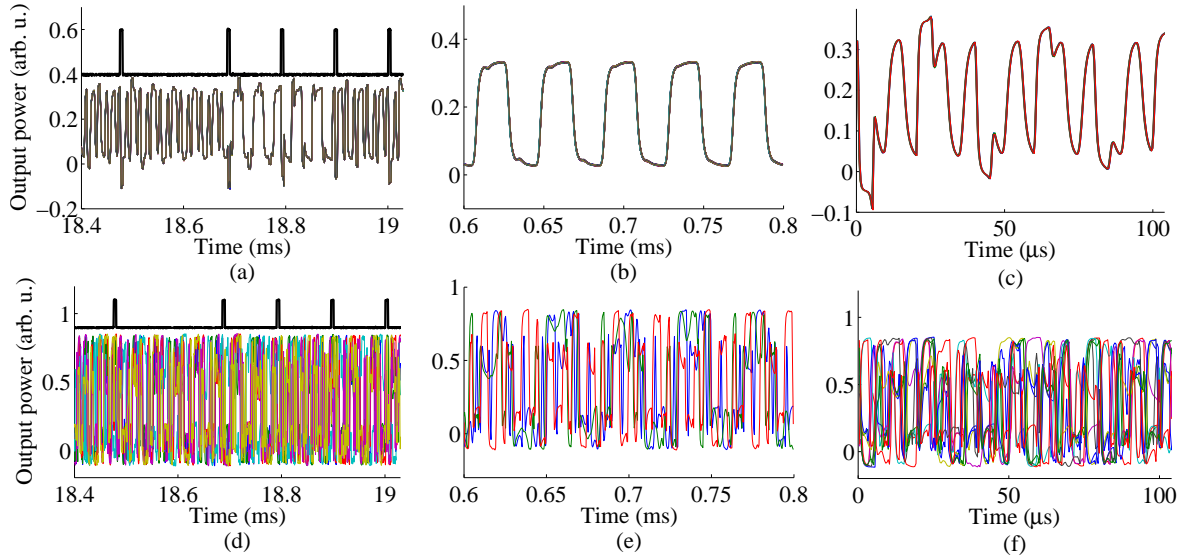
Figure 5.8: Experimental time traces (colored curves) under modulation (black curve) for (a) I=27.00mA and (d) I=37.04mA. (b) and (e): zoom into the recovery times of the autonomous dynamics for I=27.00mA and I=37.04mA respectively. Responses to a randomly chosen pulse for (c) I=27.00mA and (f) I=37.04mA.
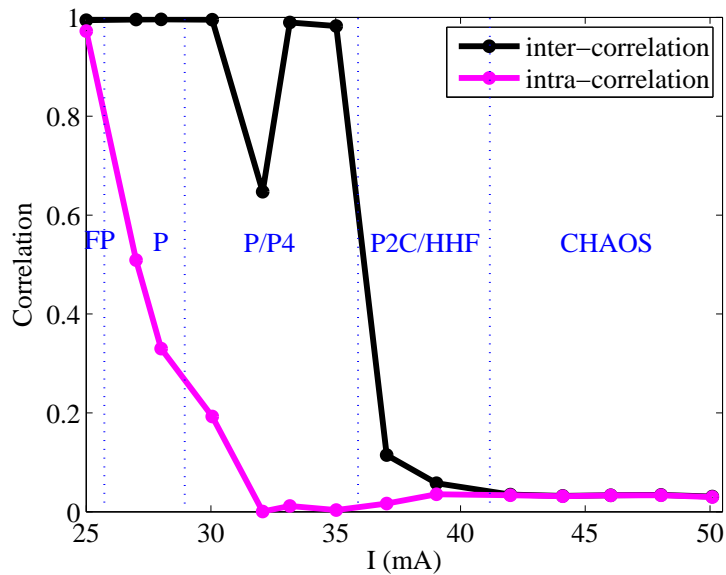
Figure 5.9: Correlation as a function of the pump current I for a drive of pseudo-random distribution of pulses with amplitude of 300mV_{pp}. The dotted lines divide in an approximate manner the different dynamical regimes found at different I. The dotted vertical lines indicate approximately the ranges of the different autonomous dynamics of the system. FP: Fixed Point; P: Periodic, P4: Period 4; P2C: Period-2-chaos; HHF: High Harmonic Frequency dynamics; Chaos.

To complement these observations with a systematic study over a larger range of the bifurcation parameter, we calculate the two kinds of correlation for opto-electronic intensity oscillator driven by the pseudo-random pulse sequence. For every value of β, the 77 repetitions of the drive are compared, in terms of inter-responses and intra-responses. The window used for the correlations is defined by the shortest interval between pulses, 105μs, as depicted in Fig. 5.8 (c) and (f) and includes the pulse itself. The results of the analysis are summarized in Fig. 5.9. The dotted vertical lines separate the dynamical scenarios of the system. The contrast between inter- and intra-correlations is quite significant for the periodic and period doubling regimes, after which the difference between them is reduced. These are the conditions under which the injection of a certain pulse causes the consistent changes in frequency dynamics, thus leading to a low correlation among intra-responses. Albeit the contrast is significantly larger than in the sinusoidal drive case, the trend of the correlation curves is the same, showing a drastic decrease of the correlation as the dynamics reach a local chaos branch. The drop around 32mA in the inter-correlation is related to the weak presence of multistability in this operating point, which affects the initial conditions set on the recovery times. Beyond 43mA, when the fully developed chaos is established, the modulation does not leave any reproducible signature on the dynamical responses and the responses become inconsistent.

5.4.3 Recorded time traces: consistency to its own dynamics

In this subsection, the drive signals used to test the consistency of the responses of an electro-optic intensity modulator are time traces generated by the system running in a closed loop configuration and without external forcing. For comparison, 3 time traces were acquired at different operating conditions to be used as drive. In particular, the driving waveforms correspond to the periodic, period-2-chaos and fully developed chaos regimes. With these signals, we aim to investigate three aspects of the oscillator system. First, whether the responses can still show consistency with a more complex drive. Second, whether the system is more sensitive to its own generated dynamics. This should be translated into the achievement of higher levels of consistency. And third, whether the consistency properties vary between the three dynamical waveforms.

Aside from the original amplitude of the recorded time traces, which in some cases might exceed the V'_π, we also attenuated the signals to explore the dependence of the consistency properties on the amplitude of the drive.

For every modulation waveform, we tuned the β parameter to obtain data at 6 different dynamical regimes, which were selected manually to avoid operating conditions close to bifurcations. Those regimes at which the drives were injected are:

- A fixed point with pump currents between 24.00-26.20mA.

- Periodic dynamics that can be found in the range I=27.00-31.00mA.

- Period 4 dynamics, typically observed between I=33.00-35.50mA.

- Period-2-chaos dynamics for pump current in the range of I=36.00-37.30mA.

- Higher harmonic dynamics, the most unstable case, I=38.70-42.00mA.

- Global chaotic regime, which appears for pump currents above 43.00mA.

As part of the methodology, a control over the drift of ϕ_0 was realized before and after the data acquirement. The consistency properties are again tested via the calculation of correlations, although, here, no distinction between inter- and intra-responses is made. The whole length of the time trace is used as a correlation window and compared with every repetition so that we can only speak of inter-correlations. The duration of the time traces used for modulation are 10ms, and the blank times are 4ms long. During these acquisition of the time traces, the DC voltage was set to 7.21V. Given the extension of the study, only some representative cases are shown.

Drive 1: Periodic waveform

The periodic solution of the system is very stable over a significant feedback range, and present for almost every value of ϕ_0. The amplitude of the periodic oscillations might vary, but their period is fixed to τ_D or $2\tau_D$, depending on the position of the operating point along the slope of the nonlinear function. This case study can also be seen as an extension of the harmonic drive investigations with a slower frequency of 50kHz. The recorded waveform for I=30.01mA with a range of the dynamics V_0=600mV_{pp} is depicted in Fig. 5.10(a). The consistency results as a function of pump current and amplitude of drive are sketched in Fig. 5.10(b). The overall trend of the curves resembles the harmonic case presented in section 5.4.1, with high correlation values for small pump currents and a monotonic decrease of the values as β is increased. The start of the decay in the correlation varies with the amplitude of the drive. Large amplitudes $(0.6-1)V_0$ can sustain a consistent response up to pump currents of 37mA. For the lower amplitudes, the consistent response is limited to pump currents below 30mA, meaning periodic conditions. It should also be noted that the smallest amplitude does not necessarily imply the worst performance. When the system operates at fully developed chaos, the consistency goes down to correlations close to 0, regardless of the drive amplitude. This indicates that a consistent behavior does not seem possible at these conditions.

Drive 2: Period-2-chaos waveform

The period-2-chaos dynamics is very sensitive to slight parameter variations, even when the oscillator is running freely, and tends to coexist with other types of dynamics like the higher harmonics. It is therefore not surprising that multistability is also present for setting drive amplitudes when the period-2-chaos is used as a drive.

Figure 5.11(a) depicts a zoom of the recorded signal used as a drive, with global square-wave like oscillations, with periodicity $2\tau_D$ and fast chaotic oscillations superposed. The original amplitude of the oscillations is 0.97mV_{pp}. An example of the response dynamics
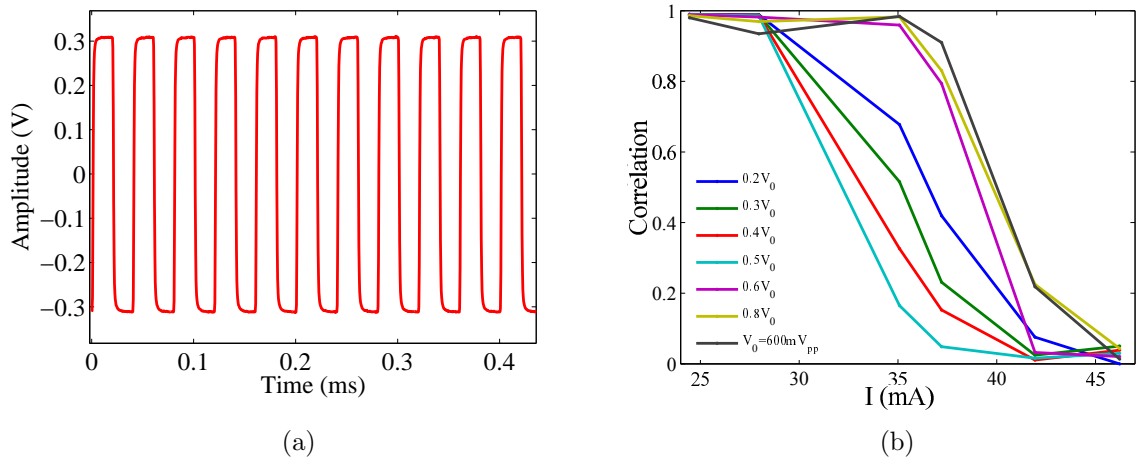
Figure 5.10: (a) Zoom into a part of the periodic drive signal acquired at I=30mA. (b)Inter-correlation values for the periodic drive as a function of the pump current.
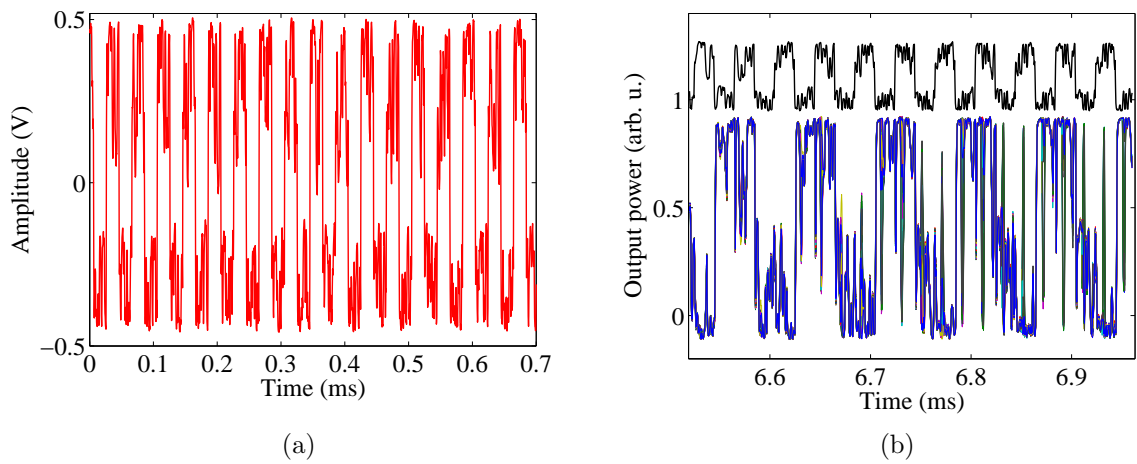

Figure 5.11: (a) Temporal piece of the drive signal corresponding to a period-2-chaos dynamics. (b) Black: signal drive with $0.5V_{pp}$; coloured curves: 10 responses at higher harmonic dynamics I=39.05mA.

of the system to the period-2-chaos modulation is shown in Fig. 5.11(b). The drive signal was injected into the opto-electronic system for a pump current of I=39.05mA, which in the autonomous feedback dynamics conditions would correspond to a period-2-chaos or higher harmonic dynamics. The modulation, plotted in black with an offset, was 50% attenuated in the experiment. Below the modulation, 50 response waveforms are depicted for a time interval larger than 450μs. The figure shows the transition around 6.65ms from a perfectively synchronized response of all the time traces to a bistable behavior in which the time traces are divided into two types of dynamics. Here, the bistability of the system is manifested during the modulation of the system, and not right after the start or removal of the drive. Consequently, there is a loss of the global consistency among the responses. However, it should be noted that the fact that the transition takes place at exactly the same instant along the many repetitions can be seen also as a consistent behavior. Such temporal consistent switching could be due to the vicinity of coexisting attractors but the actual mechanisms leading to this phenomenon are still to be investigated. Although not shown in the figure, the whole sequence of responses goes through a process of transitory dynamics, bistability, synchronization and bistability again, and every transition happens at a precise and consistent timing.

The correlations calculated for different values of β and amplitudes of modulation are shown in Fig. 5.12. Low amplitudes of the drive (0.2-$0.4V_0$) lead to high correlations when the pump current is below 30mA. Nevertheless, the response dynamics does not follow the drive, being structurally different from the injection dynamics. With the increase of β, their correlation values decrease, and the responses exhibit only a phase synchronization. For higher amplitudes of the drive, the responses are highly correlated for pump currents up to 40mA. There are two significant drops at 37mA for amplitudes of $0.4V_0$ and $0.5V_0$. Although many other causes can be involved in the origin of the low correlation, the operating conditions around this pump currents are close to the bistable solutions of period-2-chaos and higher harmonic dynamics, which imply transitions between the two states, and/or the need for longer recovery times. It is worth mentioning that, in the chaotic regime, the consistency of the system to a period-2-chaos drive signal is higher than in the previous cases shown. The amplitude of $0.6V_0$ presents the best entrainment in the chaotic regime, although the overall consistency in the global chaos regime is better than the results obtained with previous drives.

Drive 3: Chaotic waveform

In this last section, a chaotic waveform, as illustrated in Fig. 5.13, is used as a drive. The amplitude of the chaotic oscillations is $V_0 \simeq 1V_{pp}$. Two examples of the driven dynamics for different operating conditions are depicted in Figure 5.14. Plot (a) shows the modulation in black color, attenuated to a 20% of the natural amplitude together with 50 dynamical responses obtained at I=34.98mA. Plot (b) shows 50 responses to the same drive with amplitude $0.8V_0$ and acquired at I=39.58mA. Two important features are worth of note. In both cases, all trials overlap in fluctuations that differ from the drive, which demonstrates the ability of the system to respond consistently to the modulation. But a comparison between
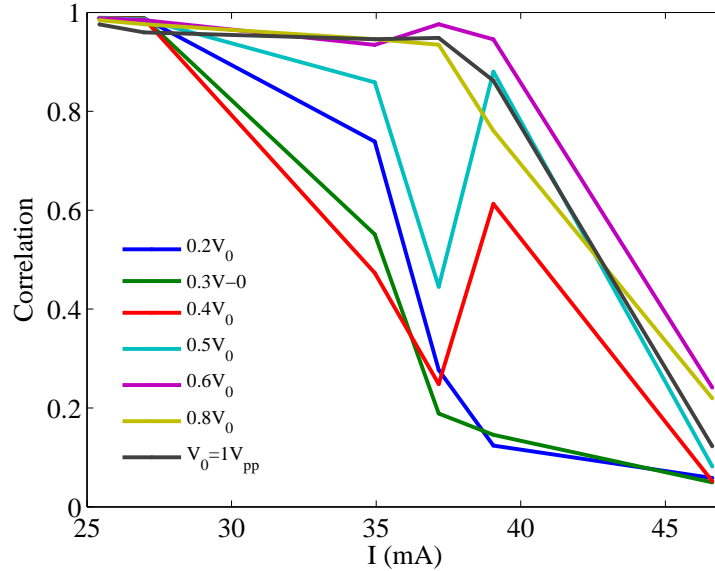
Figure 5.12: Inter-correlation values as a function of the pump current I for a drive of period-2-chaos. The color of the curve represents the case for a given amplitude of the drive.

the dynamics of plots (a) and (b) also points to the fact that the responses are characteristic to the operating conditions.

The examination of the consistency properties for a chaotic waveform in terms of correlations is depicted in Fig. 5.15. The curves for different attenuations of the drive show a plateau, almost insensitive to the amplitude, until pump currents of 35mA are reached (presumably period 4 dynamics). Above 35mA, the diminution in correlations is not as dramatic as with other drives. The correlation curves are ordered with enlarging width of the drive, achieving a correlation beyond 0.5 in the fully developed chaos regime when the original amplitude of the injected signal is unmodified. Even though a correlation of 0.5 is not enough to make strong claims on the consistent behavior of the system in a chaotic regime, it is a promising result in terms of the consistency capabilities of the opto-electronic oscillator, and the understanding of their dynamical properties. It also demonstrates that the system responds with a higher level of consistency when the drive is more similar to the intrinsic operating conditions. The reason behind this phenomenon represents a challenging aspect that deserves to be addressed in the future.
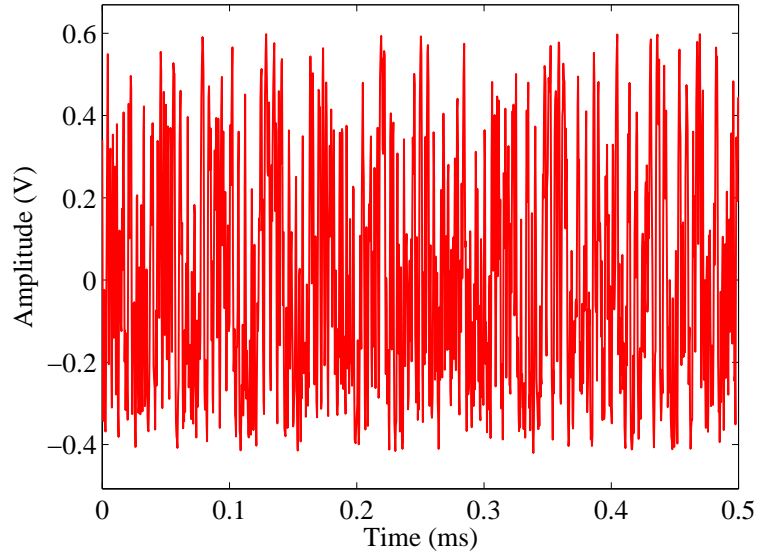
Figure 5.13: Zoom of the chaotic time trace used for the modulation.
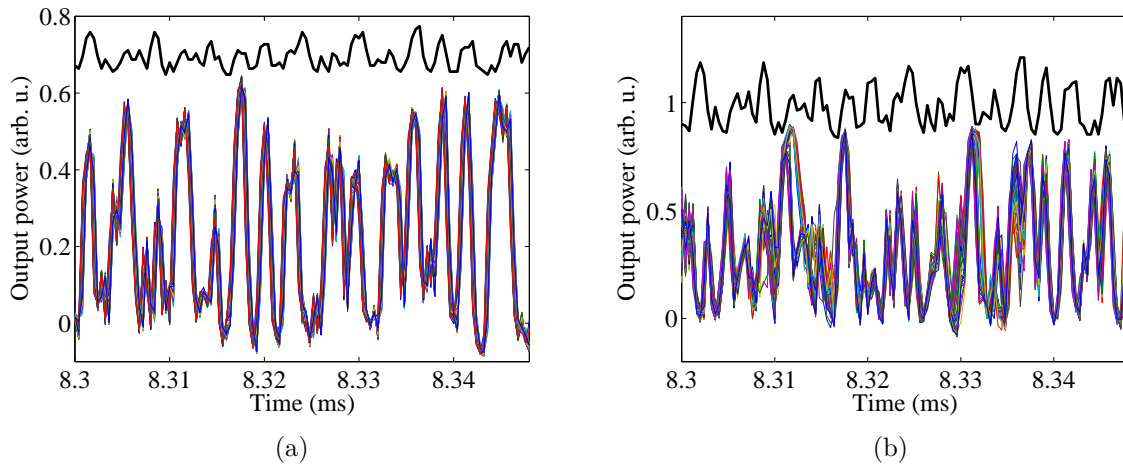
Figure 5.14: (a) $0.2V_{pp}$ at period 4 dynamics I=34.98. (b) $0.8V_{pp}$ at higher harmonic dynamics I=39.58mA.
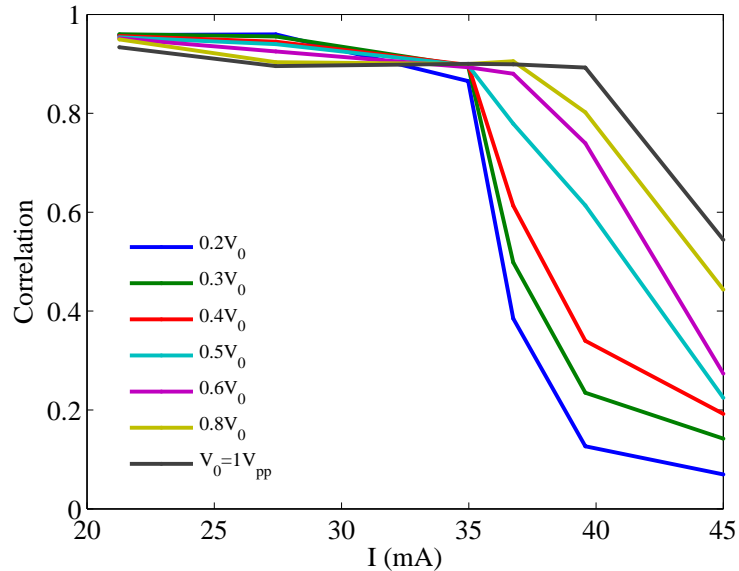
Figure 5.15: Correlation as a function of the pump current I for a drive of pseudo-random distribution of pulses with amplitude of $300mV_{pp}$.

5.5

Summary and conclusions

We presented the consistency characteristics of an electro-optic intensity oscillator with Ikeda dynamics subject to different external drive signals. The system without external modulation is known for its characteristic routes to chaos, depending on the bifurcation parameters and displays waveforms, from periodic oscillations to fully developed chaos. The drive signals were injected into the Mach-Zehnder modulator while the system was in closed-loop operation and at different dynamical regimes, controlled by the bifurcation parameter β. Our results show, in general terms, that a highly consistent response is attainable when the system is operating in periodic or period-4 oscillations, regardless of the drive or its amplitude. As the pump current of the laser is increased, the system is more sensitive to external perturbations, and other factors come into play so that consistency depends strongly on the operating conditions and the drive properties.

In our investigations we used an harmonic drive, a pseudo-random pulse sequence and recorded waveforms as drives. As the complexity of the drive increases, the responses of the oscillator get more diverse. The harmonic drive had the frequency of the 11th harmonic and a fixed amplitude below V_{π}' of the system. The nature of the waveform allowed us to distinguish between inter-correlations (comparison of the same period along the repetitions), and intra-correlations (comparison among different periods). The correlation curves for inter- and intra-

responses exhibit two major features: the inter-values are consistently above the intra-values, and both correlations decrease as the dynamics starts to exhibit chaotic characteristics.

The same features are obtained for a drive following a pseudo-random pulse distribution. Nevertheless, the contrast between inter- and intra-correlation is significantly higher than in the harmonic case. This is due to changes in the dynamics induced by the pulse, which consistently alter the frequency of the oscillations from one pulse to another.

Interesting results are also observed when signals generated by the system are used for modulation, with varying amplitudes. Although the trend in correlations is always the same (high consistency with drastic decay as the dynamics enters into chaotic regimes) differences can be found between the drives. A drive consisting of periodic oscillations result in a similar behavior to that observed with the harmonic drive. As the drive signal shows chaotic characteristics (period 2 + chaos), the consistency at high values of β is remarkably improved. When a chaotic signal is used for modulation, the correlations in the chaos regime acquire values above 0.5. In all cases, the consistency properties vary slightly with the amplitude of the signal.

The opto-electronic oscillator shows physical features like multistability and hysteresis that can degrade the reliability of the responses to the drive. Moreover, experimental issues such as parameter drift can worsen the reproducibility if not controlled accurately. Nevertheless, the oscillator has still proven to show consistency at many levels. Multistability can destroy consistency by switching between dynamical states during the driving process or at the recovery times. But then, such bistability also leads to other interesting and consistent behavior: the occurrence of the transition from one solution to another during the injection of the drive at the same instant, which we named temporally consistent switching. Also related to the surprising role of timing is the effect of the injected perturbations, crucial to induce reliable changes in the driven dynamics like the frequency of the oscillations. For almost all drive signals, the responses still preserve partial consistency when the system operates in a regime of local chaos. In the example of the chaotic drive, the degree of consistency is even sustained in the fully developed chaos. These results open new perspectives for information processing techniques, which could extend their performance to other conditions of operation.

Yet many questions remain unaddressed. From the practical point of view, the effect of amplitude and frequency of an artificial drive signal needs to be characterized in more detail. Specifically, the ratio between the amplitudes of the modulation and the autonomous dynamics can be a key factor to guarantee consistency. Moreover, the mechanisms that lead to an inconsistent response have been identified (bistability, operation close to bifurcation, drift in parameters...) but their individual contributions in a practical example have not been quantified yet. In the case of an harmonic or pulsed drive, it would be interesting to characterize the temporal dependence of the inter-correlation. This means to calculate the period-resolved correlations in the case of the harmonic drive, and the pulsed-resolved correlations in the case of the pulsed drive. Preliminary results with the harmonic drive indicate the existence of a transitory time after the beginning of the modulation characterized by low inter-correlations per period. As the time evolves, there is a time window where the responses are highly synchronized until the inter-correlations go down to low values again. A

deeper investigation could clarify the presence of some sort of memory time in the system. Also the pulse duration represents an important parameter to explore in the case of the pulsed drive. From a fundamental point of view, the Ikeda delay system has a constant negative sub-Lyapunov exponent in all regimes, meaning that the system can exhibit weak chaos only. In the weak chaos regime, consistent responses of the laser system are expected but we showed that in the local or global chaos, those are difficult to achieve. The exception is found in the chaotic modulation, where the similarity between the drive and response dynamics causes a consistent repetition of the response behavior with every replay of the drive. Besides, the dynamics under modulation, with their characteristic and original oscillations, are full of interesting phenomena, from which we only presented a small sample. These open questions illustrate the potential of the driven Ikeda system, as a promising scheme full of unexplored capabilities.

Random bit generation with a chaotic semiconductor laser

> "The generation of random numbers is too important to be left to chance."
>
> Robert R. Coveyou,
> Mathematician

Random bits are widely used in modern digital technologies, including communication and computation systems. Modern cryptography relies on randomness to guarantee the security of the systems. For instance, authentication and encryption protocols use random bits as codes or keys to scramble the information and protect it from being hacked. Weather forecasters, climate scientists, financial experts, and social physicists also require random numbers to run their predictive models and study with them phenomena such as climate change, economic growth or spreading of epidemics.

Such a demand for randomness has lead to the appearance of different approaches to random bit generators (RBGs), based either on physical entropy sources or deterministic algorithms. Quantum RBGs, founded on physical random phenomena such as nuclear decay, generate, in principle, truly random bit sequences. However, they produce them too slowly to be integrated in modern technologies. Besides, their implementation is often a non trivial task that requires a strict control over the underlying properties.

In contrast, pseudorandom bit generators based on a random seed and a deterministic algorithm allow for faster bit rates, but are vulnerable if the seed is guessed. To overcome these limitations, laser schemes based on the digitization of a chaotic signal [25, 137] have been proposed recently. With the use of semiconductor lasers as the source of chaos [138], fast independent bits at high speed can be generated, taking advantage of the inherent noise and fast temporal dynamics, and resulting in a large spectral bandwidth.

In this Chapter, we demonstrate the generation of random bits at high speeds by means of a chaotic laser system. We employ the chaotic output of a single semiconductor laser subject to its own time delayed feedback. More precisely, our scheme is based on a single laser subject

to polarization rotated feedback. Among its advantages are the simplicity and robustness of the setup together with the rich and suitable dynamics for the generation of random bits that this system displays. The evidence of the randomness of a candidate bitstream is typically provided by standard test batteries [139]. They represent the reference for randomness, and can be computationally intensive and time consuming. In order to construct suitable systems for random bit generation, it is necessary to identify the conditions under which a dynamical system and digitization process are likely to succeed or fail, without having to test all possible conditions in advance. We consider the interplay between the dynamics and digitization process, including acquisition conditions and postprocessing methods, for successful random bit generation. With our general guidelines, extensible to other chaos-based systems, we can define optimal conditions, and minimize the postprocessing procedures. We also demonstrate experimentally the relevance of these criteria by improving the performance of our random bit generator. Finally, we discuss the information theoretic limits, confirming that, with our approach, we reach the maximum possible generation rate.

This Chapter is based on the work from the following publications: N. Oliver, M. C. Soriano, D. W. Sukow, and I. Fischer, *Dynamics of a semiconductor laser with polarization-rotated feedback and its utilization for random bit generation*, Opt. Lett., vol. 36, no. 23, pp. 46324, Dec. 2011. N. Oliver, M. C. Soriano, D. W. Sukow, and I. Fischer, *Fast Random Bit Generation Using a Chaotic Laser: Approaching the Information Theoretic Limit*, IEEE J. Quantum Electron., vol. 49, no. 11, pp. 910918, Nov. 2013. The characterization of the setup and the experimental data acquisition was conducted by Neus Oliver together with David W. Sukow. Miguel C. Soriano contributed to the assembling of the experiment and application of NIST tests. The success of the experiment is a consequence of the vivid discussions with Miguel C. Soriano, David W. Sukow and Ingo Fischer.

6.1

What are random numbers?

A random number is a number generated by a process whose outcome is unpredictable, independent, and cannot be reproduced. A good example of random numbers can be obtained from coin flipping. If we assign heads to bit 0 and tails to bit 1 from an unbiased fair coin, each flip has a probability of 50% of producing a 0 and equal probability of obtaining a 1. If we repeat this process many times, we would get a binary random sequence of bits (0 and 1) in which every bit is generated independently of the others, and it is impossible to predict the next one (heads or tails) from knowing the past results. The process is also known as random bit generation.
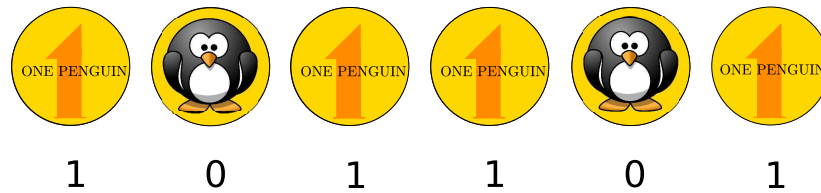
Figure 6.1: Example of binary random sequence obtained from flipping a coin six times: 101101.

6.1.1 Types of random bit generators

In this example, we use the coin flipping as a random number (or random bit) generator. However, when it comes to cryptographic applications, this would neither be a sufficiently fast, nor a practical method to generate infinite sequences. Therefore, there are two basic types of generators that have been used to date: Pseudorandom Number Generators (PRNGs) and physical Random Number Generators (RNGs). PRNGs have been used for producing the keys used in communications systems, since they are cheap and can operate at rates that the processor speed allows. However, as its name suggests, they are not truly random, and have some fundamental limitations. PRNG are based on a deterministic algorithm which needs a "seed" to originate the sequence of pseudorandom numbers. If an attacker guesses the seed, the whole sequence of bits could be reproduced with the algorithm, making it vulnerable for security applications. Secondly, due to its deterministic and digital nature, the unpredictability is bounded by the periodicity of the bit sequence. Often, the PRNGs attempting to improve these limitations with longer periods compromise in turn their speed [140].

For such reasons, there is a growing interest in new systems capable of generating true random bits, using real random or unpredictable phenomena. Physical Random Number Generators (RNGs) produce random bits from physical entropy sources or chaotic physical processes. Some examples are the Quantum RBGs, which promise to generate truly sequences based on quantum mechanical uncertainty [141, 142, 143, 144] or noise-based RBGs [145, 146, 147, 148, 149]. Other examples of physical processes include atmospheric noise [58], electronic noise [150] or chaotic electrical circuits [151]. However, these RNGs typically produce the random bits too slowly to keep pace with modern data rates.

6.1.2 Why a random bit generator based on a semiconductor laser?

A promising approach for fast RNGs is the use of semiconductor lasers as a source of chaos. Semiconductor lasers allow for large spectral bandwidth and strongly diverging trajectories when subjected to external perturbations, such as delayed optical feedback [17, 152]. Moreover, semiconductor lasers have an inherent source of noise, the spontaneous emission noise, which contributes to the randomness and avoidance of recurrences of the system, together with additional sources of noise intrinsic to the experiment (see section 6.3.4). These properties of chaotic lasers have made high generation bit rates possible [153] when used in combina-

tion with some form of postprocessing. Some examples of chaotic laser-based RBGs include semiconductor lasers with optical feedback [25, 154, 155], optical injection [153, 156, 157] or photonic integrated circuits [158, 159, 160].

Another advantage of employing semiconductor lasers is their easy implementation in telecommunications systems. Semiconductor lasers, due to their small size and their feasible integration in fiber-optic components, are the ideal candidates to be used in real commercial systems or in conjunction with classical encryption techniques. Moreover, as an optical approach to random number generation, high generation speeds are possible.

6.2
Experimental implementation

For wide applicability, we have designed an experimental system that is simple, compact, robust, and made of relatively low-cost, standard, fiber-based telecom components. It comprises a semiconductor laser with delayed Polarization-Rotated Optical Feedback (PROF). Semiconductor lasers subjected to polarization rotated feedback exhibit a rich variety of complex phenomena [161].

As illustrated in Fig.6.2, the experiments involve a single semiconductor edge-emitting laser (Eblana Discrete Mode Laser), with a wavelength of 1.54 μm and with a threshold current $I_{th} = 12.1$ mA at 22°C. The laser package is built without optical isolators. The laser diode is fiber-pigtailed, and connected to a 1x2 90/10 optical coupler, the principal output of which passes through a variable optical attenuator used for feedback strength control. A Faraday mirror (FM) provides the polarization-rotated optical feedback, and its behavior is based on the Faraday Effect. [1]
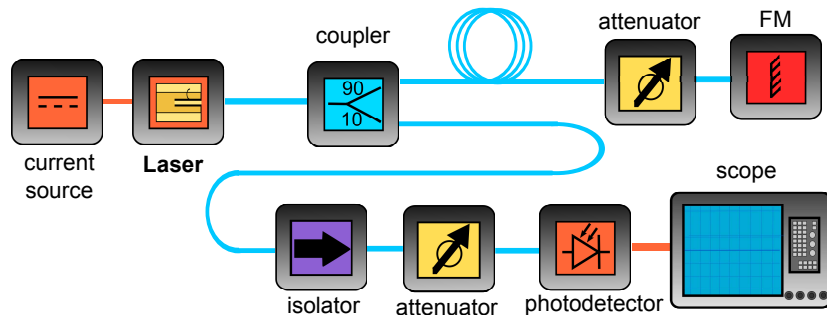
Figure 6.2: Experimental schematic diagram.

---

[1]The Faraday effect describes the rotation of the polarization of a signal, as it passes through certain optical media within a magnetic field. Located at the end of the optical fiber, the Faraday mirror is designed to rotate the polarization state by 45° twice, once when the light enters, and again when the light is reflected back into the fiber. Since the Faraday effect is non-reciprocal, the resultant polarization of light is rotated by 90° with respect to the original signal.

The Faraday mirror reflects the light, and rotates its polarization state by 90° with respect to the original signal. Between 10-20% of the emitted output light is reinjected back into the laser, forming an external cavity with a roundtrip delay time of $\tau = 90.9$ns. This simple and robust experimental system, made of standard fiber-based telecom components, is insensitive to changing environmental conditions, i.e. any polarization mode dispersion or birefringence that occurs anywhere along the optical fiber is exactly compensated for by the Faraday mirror. The roundtrip time is chosen sufficiently large such that the feedback phase has no influence on the dynamics. Moreover, this configuration can produce strong feedback which will prove to be an important element in our study.

The light exiting the 10% port of the optical coupler is used for detection. It first passes through an inline optical isolator and, then, an attenuator which controls the power impinging on the fiber-coupled photodetector (Miteq 12.5GHz bandwidth). The signal is captured by a digitizing oscilloscope (LeCroy 816Zi, 16GHz analog bandwidth, up to 80GS/s sample rate, 8-bit ADC). The acquisition settings are controlled with the data analysis functions of the oscilloscope. The electrical signal is finally postprocessed in an offline procedure.

6.3

Dynamical properties for a good Random Bit Generator

The employed dynamics plays a crucial role in the success of random bit generation, since not all dynamical states may lead to the generation of sufficiently independent bits. A system with certain dominant frequencies in its dynamics could produce some recurrences in a bit sequence, showing a periodic non-random pattern. In the same manner, working in a dynamical region of periodic, quasi-periodic or steady-state operation would not produce random numbers because its output would not satisfy the condition of unpredictability. Consequently, dynamical schemes, in which a chaotic signal is digitized for the generation of bits, have been intensively investigated. For this approach, semiconductor lasers are an excellent source of chaos. The fast internal timescales of the semiconductor lasers allow for large bandwidth dynamics when subjected to delayed optical feedback [38] and, thus, chaotic lasers enable the generation of random bits at ultra-fast rates [25, 77, 154, 162]. So far, most of the studies focused on systems with optical feedback which preserve the polarization state of the light in the feedback loop. The polarization maintained feedback has been proven useful in many applications including chaotic transmission [20, 163]. However, it is very difficult to guarantee a coherent feedback when light is transmitted in a standard optical fiber over a long distance. Other schemes of delayed optical feedback employ polarization rotated feedback [161, 164]. When a laser is subjected to polarization rotated feedback, the two polarization modes interact directly or through the carrier density, giving rise to chaotic instabilities. This type of delayed optical feedback has been less studied in the literature and the dynamical scenarios have not been fully understood.

One main feature of semiconductor lasers subject to delayed optical feedback is the destabilization of the output intensity. The dynamics becomes unstable with unpredictable changes

in the amplitude of the signal. Figure 6.3 depicts a zoom into a chaotic time trace with fluctuations in the sub-nanosecond scale. It should be noted that, although many experiments with PROF are polarization-mode resolved, in our setup we detect the total output intensity only. Therefore, all the temporal data shown in this Chapter and the results derived correspond to the total output intensity.
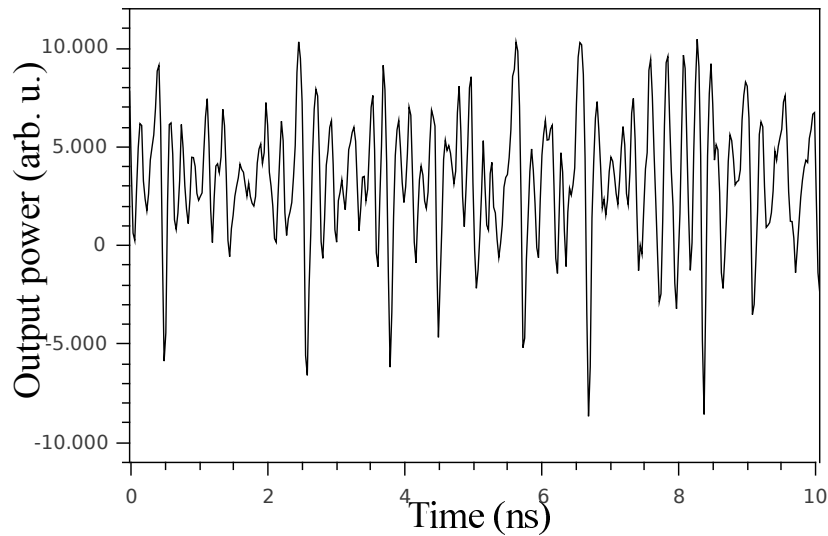
Figure 6.3: Chaotic oscillations in the output intensity of a SL pumped at $1.52I_{th}$ with PROF.

When it comes to random bit generation, having a system with chaotic dynamics is not sufficient to identify suitable operating conditions. In particular, two features are considered to be necessary to generate randomness: a broad radio-frequency power spectrum and an autocorrelation function (AC) with a fast decay.

6.3.1 RF power spectrum

A broad rf power spectrum, that mimics white noise and allows for fluctuations at frequencies up to 10GHz (and beyond), is considered to be a necessary feature to produce randomness at high speeds. Figure 6.4 shows power spectra at different pump currents and feedback strengths, acquired by replacing the scope with an RF spectrum analyzer (Anritsu MS2667C). Feedback strength is quantified as the fractional power transmission T in the external cavity, that is, the ratio of power reentering and emerging from the laser pigtail. This is a convenient operational definition, although it does not include laser/fiber coupling efficiency. Figures 6.4 (a) and 6.4 (b) are for equal, strong feedback but different currents; both display a broad spectra with no dominant frequencies evident. If only spectral criteria were considered, either of these would be a good candidate for a RBG. In contrast, the spectrum of Fig. 6.4 (c) is for similar current but lower feedback than 6.2 (b). It displays more structure with two

evident peaks (relaxation oscillation peak and its second harmonic) and, therefore, would be considered less suitable for randomness applications. The signature of the external cavity
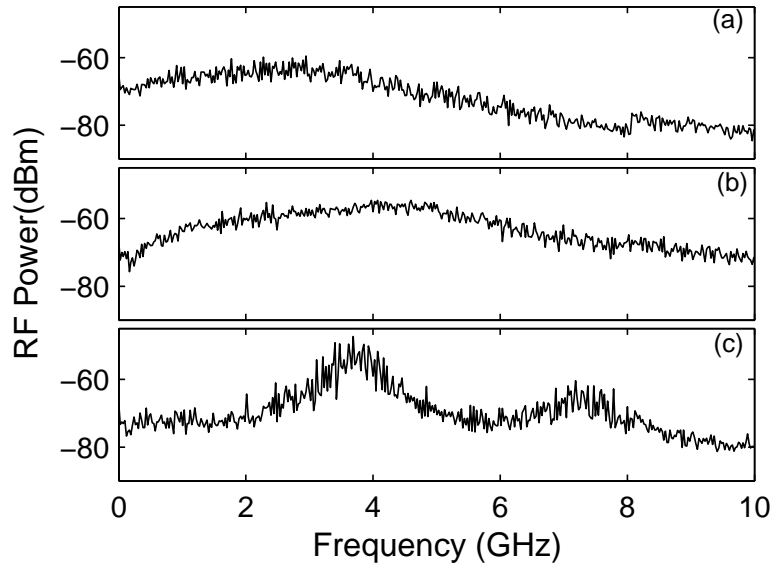
Figure 6.4: Rf power spectra of the laser intensity for (a) 14mA, T=52.2%, (b)=18.3mA, T=52.2%, (c)=18.3mA, T=16.9%. Figure from [162].

modes in integral multiples of 11MHz is not apparent on this scale, but can show up on the 100 MHz scale, as depicted in Fig. 6.5. The observed mode spacing is $\Delta f \sim 5.4$MHz, corresponding to twice the round-trip time (2τ). The mode spacing can be translated into an optical cavity length of L ~ 8.2m.

Most previous studies on PROF systems have involved low or moderate feedback, where spectral structures are more apparent but the strong feedback chaotic case has not been studied thoroughly. The ability to access this regime experimentally is critical for our random bit generation study.

6.3.2 Autocorrelation conditions

Low autocorrelation (AC) conditions, at which temporal correlations are the weakest, help select an optimum operating point, and assure the independence of successive points by selecting an appropriate sample interval.

The external cavity round-trip frequencies at integer multiples of $1/\tau$ are also evident in the time domain. The corresponding timescale τ appears in autocorrelation functions of time traces. The autocorrelation function between times t and s is defined as:
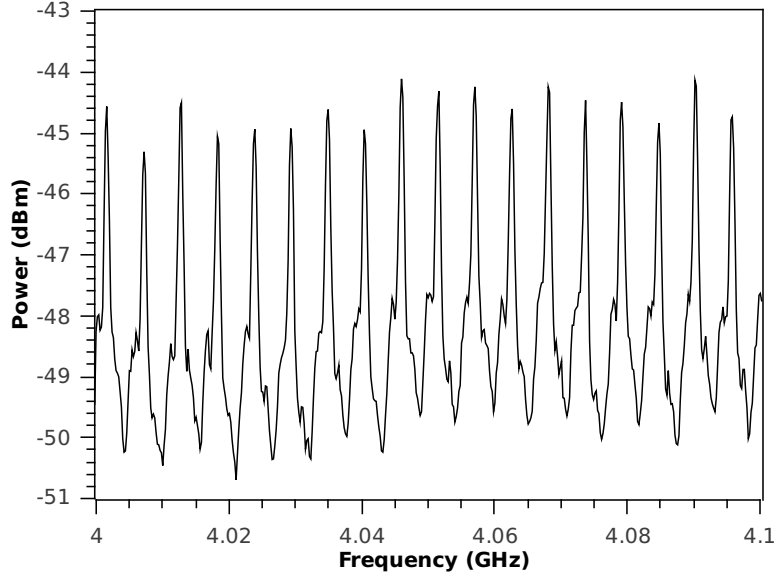
Figure 6.5: RF-spectrum of a SL with PROF showing the external cavity modes. The pump current is 19.00mA and T=52.2%.

$$AC(s) = \frac{<[x(t)- <x(t)>][x(t-s)- <x(t)>]>}{<[x(t)- <x(t)>]^2>} \tag{6.1}$$
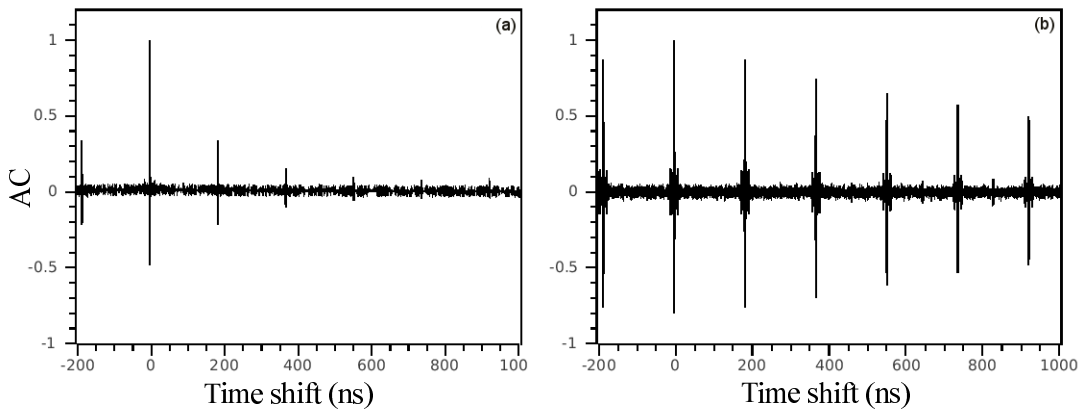
Figure 6.6: AC function of the intensity dynamics (a) for 14.1mA and T=16.9% and (b) for 18.3mA and T=16.9%.

Figure 6.6 shows the AC up to a time shift of 1000ns. Peaks in the AC function appear at integer multiples of τ, as is typical for delayed feedback systems. Figures 6.6 (a) and (b) were obtained under the same feedback level (T=16.9%) but with different pumping current (14.1mA and 18.3mA respectively). The increase of pump current leads to drastic changes in the height of the AC peaks, which can indicate a transition between strong and weak chaos regimes. The high delay echos of Fig. 6.6 (b), having a correlation almost as high as for the zeroth peak, indicate a possible weak chaos regime, in which the response of the laser is consistent to its own feedback after one delay time. As the pump current is decreased, the height of the peaks diminish, entering into a region of strong chaos (Fig. 6.6 (a)). Operating in a strong chaos regime, where the AC peaks have the smallest height, is advantageous for the application of random bit generation.

Interestingly, the height of the AC peak at even multiples of the delay time is larger than at odd multiples of τ, which are imperceptible in most cases. This is a particular characteristic of the PROF systems, due to the rotation of the polarization state of the light. The polarization of the travelling light is parallel to the original emitted light of the laser after two roundtrips, causing a major contribution to the even-multiple AC peaks.
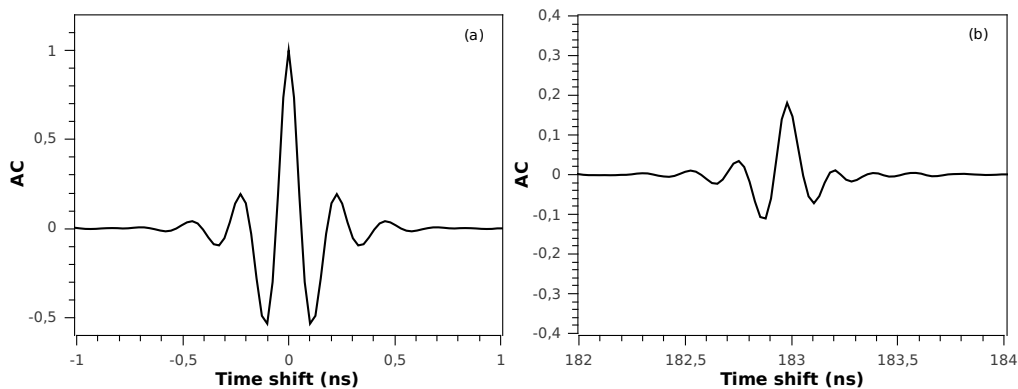
Figure 6.7: AC function of the intensity dynamics: a) For the resolved zeroth AC peak; b) For the resolved second AC peak.

A detail of the AC function of the intensity dynamics obtained for I=18.3mA and a power transmission of T=52.2% is shown in Figure 6.7. It corresponds to the same operating conditions as Fig.6.4 (b). Fig. 6.7 (a) depicts the AC function around zero time shift, which decays rapidly, and where correlations between points in time are lost within 1 ns. The structure of the second peak, shown in Fig. 6.7 (b), is smaller compared to the zeroth peak, slightly asymmetric, and also presents a faster decay [165]. The AC peak heights at multiples of τ and the width of the zeroth peak both provide useful criteria for tailoring the dynamics. To select the operating conditions for the laser, we can first identify under which pump current and feedback strength the height of the delay time peak is minimum, avoiding

a situation like 6.6 (b). This will assure an operating point at which temporal correlations are the weakest. In contrast, to ensure that successive points will be independent of one another, the sample interval needs to be longer than the AC decay time.

6.3.3 Systematic study of the AC properties

For a systematic study of the autocorrelation properties, we examine the height of the AC peak at time shifts of 2τ as a function of laser pump current and feedback strength. We choose the 2τ peak as reference because, as is typical of PROF systems, it is the largest. Nevertheless, we have verified that the first peak at τ delay shows the same features. The results are shown in Fig. 6.8. The pump current is represented on the horizontal axis, feedback strength is along the vertical, and the 2τ AC peak height is indicated by the color legend on the right hand side.
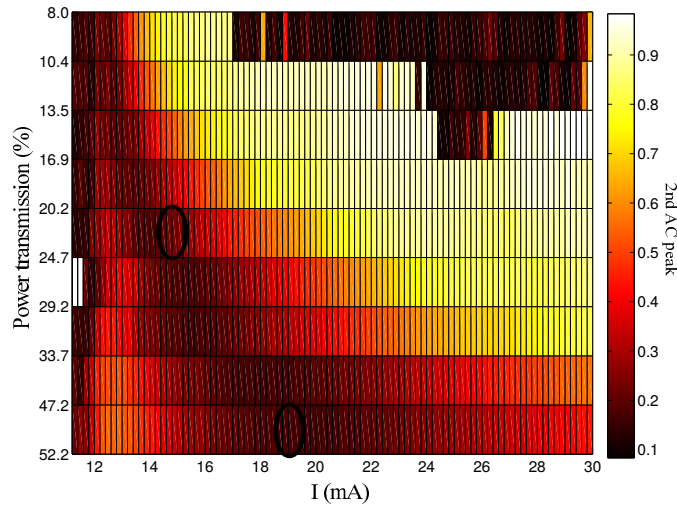
Figure 6.8: Map of the height of the AC second peak for varying feedback and current conditions. The selected operating conditions are labeled within the ellipses. Figure from [162].

A region of low AC appears abruptly for low coupling (power transmission of around 16.9%) and high current (24 mA), but this region corresponds to steady-state operation. The low AC in this case arises from noise, and so is rejected for a dynamics-based random bit generator. Similarly, a thin strip of low AC appears at the lowest currents (under 12mA) but, here, the laser operates below threshold so the conditions are also unsuitable. Nevertheless, a wedge of low AC begins at low currents (13mA) and low couplings (10.4% of power transmission), which smoothly grows and expands into a larger region of high feedback strength (power transmission of around 52.2%), and moderate currents (between 16-23mA). Here, the height of the 2nd AC peak is confined to values around 0.3 or below, which implies a

significant reduction of more than 70% with respect to the zeroth AC peak. In principle, any operating point satisfying this requirement is suitable as initial condition for random bit generation. Certainly, it is advantageous to select dynamical conditions where the AC peak is the shortest. The RF spectra of points within this region are also broad, thus, this region is identified as the most promising region for random bit sequences generation purposes.

Based on the dynamical guidance provided by the combination of a broad RF spectrum (as presented in Figure 6.4) and AC characteristics with short delay peaks (feedback strength and pumping current conditions inside the wedge), we select two different operating points for our random number generator based on a chaotic laser: pump current I = 19.00mA and feedback T = 52.2%; and pump current I = 15.00mA and feedback T = 24.7%. In both situations, the percentage change between the 0th AC peak and the height of 2nd peak is more than 70%.

6.3.4 Role of noise

In order to obtain random bits, we benefit not only from the dynamical properties of the laser described along this previous section. Additionally, different sources of noise are present in our experimental scheme, namely system noise and detection related noise. One of the main contributions of noise associated to the system originates from the spontaneous emission noise, inherent to the laser. Spontaneous emission noise has a quantum nondeterministic origin, and it is amplified in the system by the chaotic dynamics [74, 159, 166, 167].

Additional sources of noise come from physical devices in the experiment like the pump source but there is also detection related noise from the photodetector or the analog to digital converter. Their origin is different from the laser chaos, and its effect is also present in the random bit generation process. To what extent the presence of these additional sources of noise contributes to the generation of random bits is an interesting topic of discussion [75]. However, its contribution to the detected dynamics of the system is unavoidable in real systems, which must be considered as a whole.

6.4

Acquisition conditions

The data acquisition is an important step in the process of random bit generation. Especially, the analog to digital conversion for the amplitude corresponding to the chaotic output power, intrinsic to the acquisition hardware, is as critical for the success as the dynamical properties. It is necessary to adjust the amplitude of the analog signal to the amplitude acquisition scale of the oscilloscope such that the full 8-bit range is used in a smart manner (Figure 6.9). As a general rule, the probability density function of the original time trace should cover all the bins available (Fig. 6.9 (a)). However some restrictions must be taken into account. Points that go off-scale, i.e. points in saturation, are recorded as extrema values by the analog-to-digital converter (ADC) of the oscilloscope. If there are too many of those in a bit sequence, the blocks of zeros and ones are too frequent to be considered random. This would then

require more postprocessing steps in the random number generator. This case is illustrated in Fig. 6.9 (b), where the bins 0 and 255 are strongly over-represented. In contrast, a signal too small will only span a small subset of the possible 8-bit range, as depicted in Fig. 6.9 (c). This results in not random sequences as well.
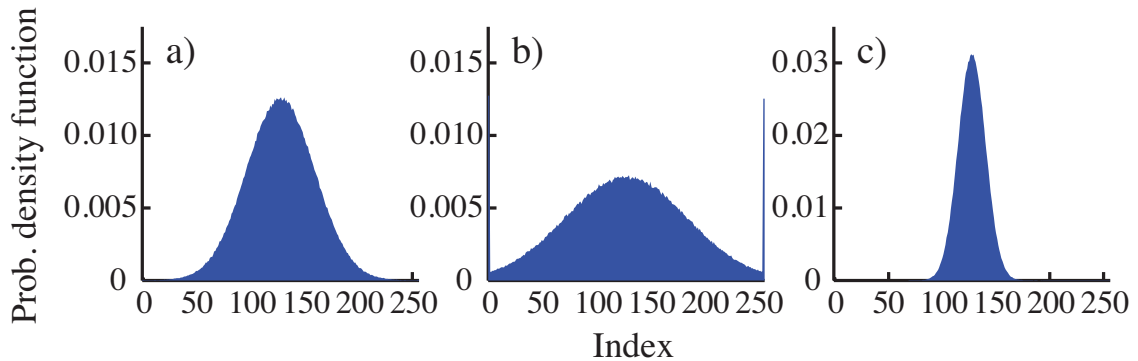
Figure 6.9: Illustration of different acquisition conditions for an artificially-generated Gaussian signal. Figure 6.9(a) shows a favorable amplitude distribution. Figure 6.9(b) shows a distribution that contains too many extrema values while figure 6.9(c) depicts a distribution with bins too sparsely populated. Figure from [77].

To obtain good reproducible results, the analog to digital conversion must be controlled so that the amount of saturated points lies within the allowed statistical deviation. This depends on the total number of samples, and the discrete bins in which the histogram is divided. The number of off-scale points is easy to restrain on-line from the oscilloscope. We set the vertical scale (without variable gain) on the oscilloscope such that the signal displayed was not too small (avoiding the case of Fig. 36.9 (c)), and then we used the variable attenuator to reduce the signal if there were too many saturated points (avoiding case of Fig. 6.9 (b)). We found the best performance of our random number generator when the ratio of extrema values to maximum value (most populated bin) is around 0.09% for 5 million points divided into 200 bins.

Furthermore, we have avoided the Digital Dignal Processing (DSP) where possible. It is commonly applied to the channel traces of the oscilloscope to flatten the frequency response, and to improve the group delay, resulting in a 16 bit format. Nevertheless, current hardware analog-to-digital converters (ADC) with 16 bit resolution are still limited to sampling rates of hundreds of MSamples/s, whereas conventional ADCs with 8 bit resolution support higher sampling rates. A preliminary truncation to the 8 LSBs has been implemented to mimic the current technological state-of-the-art for high speed ADCs. To explore the potential of our scheme, we also provide the results using the full 16 bit digitized output of the oscilloscope.
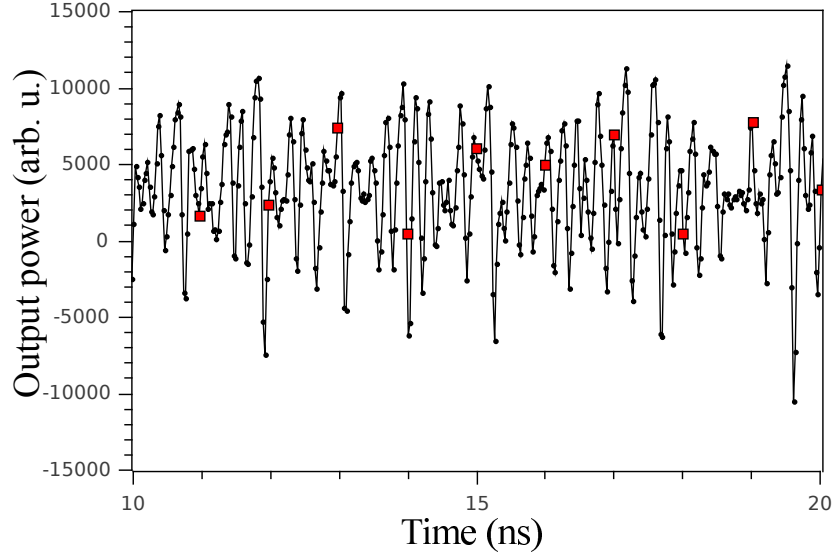
Figure 6.10: Chaotic oscillations in the output intensity of a SL pumped at $1.52I_{th}$ with PROF. Red squares indicate the points used for random bit generation.

6.4.1 Sampling rate and data acquisition

The final bit rate depends strongly on the time scales of the dynamical system but also on the initial sampling rate of the oscilloscope. The larger the sampling rate is, the more it becomes possible to generate bits at higher speed.

The first step we carry out is to capture time series at a 40 GS/s sampling rate, with the oscilloscope under the first operating conditions we selected in the section 6.3, pump current I = 19.00mA and feedback T = 52.2 %. As mentioned above, due to the Digital Signal Processing, the oscilloscope saves data initially in 16-bit binary word format, which we truncate to the 8 Most Significant Bits (MSBs) to equal the raw ADC resolution. This results in the chaotic time trace coded as a string of 8 bit binary numbers.

From the 8 bit raw data, we extract points separated by 1ns interval. In this manner, the chosen set of points exceed the decay time of the zeroth AC peak, which is around 0.7ns (see Fig. 6.7 (a)) and, therefore, we ensure that points forming the new signal are not correlated. This new set of points does not depend on past inputs, and it is said to have no memory, which makes it more suitable for random bit generation. In Figure 6.10, the red colored squares indicate data separated 1ns in time, which written in 8 bit format, as presented in Table 6.1, will be used to generate random bits. Note that the ten binary numbers present almost no variation in the three first binary positions. Taking into account this fact is crucial for RBG, as explained in the next section.

Data point	Binary representation							
	MSB							LSB
1	0	0	0	0	0	1	1	0
2	0	0	0	0	1	0	0	1
3	0	0	0	1	1	1	0	0
4	0	0	0	0	0	0	0	1
5	0	0	0	1	0	1	1	1
6	0	0	0	1	0	0	1	1
7	0	0	0	1	1	0	1	1
8	0	0	0	0	0	0	0	1
9	0	0	0	1	1	1	1	0
10	0	0	0	0	1	1	0	1

Table 6.1: Table containing binary representation of highlighted data points from Figure 6.10 spaced 1 ns in time and used for RBG. The Most Significant Bit and the Least Significant Bit are also indicated.

6.5

Postprocessing

A point of emphasis in our study is to minimize postprocessing requirements as much as possible to demonstrate the efficacy of methods based on the dynamics to generate randomness. In this manner, we keep most of the original information, and also improve the efficiency in the postprocessing, which in turn may increase the bit rates when implemented in real time. This is in contrast to protocols which start with a chaotic signal but where significant manipulation of the data is also employed, such as additional logical or software processing which combines outputs through logic gates or computing high-order derivatives [168]. Our approach is to simply omit some of the Most Significant Bits (MSBs) from each acquired data point (sample). The most significant bits are the bit positions in a binary number representing the highest exponents of 2.

The original chaotic laser intensity does not cover all values with equal probability. This can be observed from Fig. 6.11 which shows a histogram for the laser signal for 32 Million samples as detected, without any prior manipulation. The abscissa, named index, indicates the 2^8 different values one can code with 8 bits. The more symmetric the parent distribution is, the easier it is to obtain random bits after the postprocessing. Our initial distribution resembles a non-symmetrical Gaussian, in which certain values are more frequent than others. Yet, the histogram does not have saturated points nor too many empty bins, which were the two main requirements discussed in Section 6.4. The inequality and asymmetry in the parent distribution affects the randomness of the bits, but by means of the exclusion of the MSBs, a flatter histogram can be obtained.
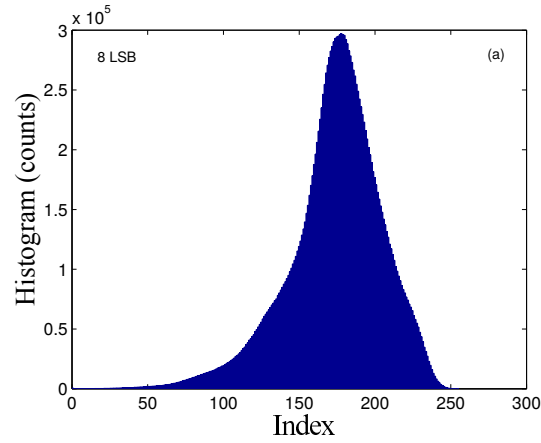
Figure 6.11: Probability density function for 8 bits, obtained at a pump current of I=19.00mA and feedback T=52.20 %.
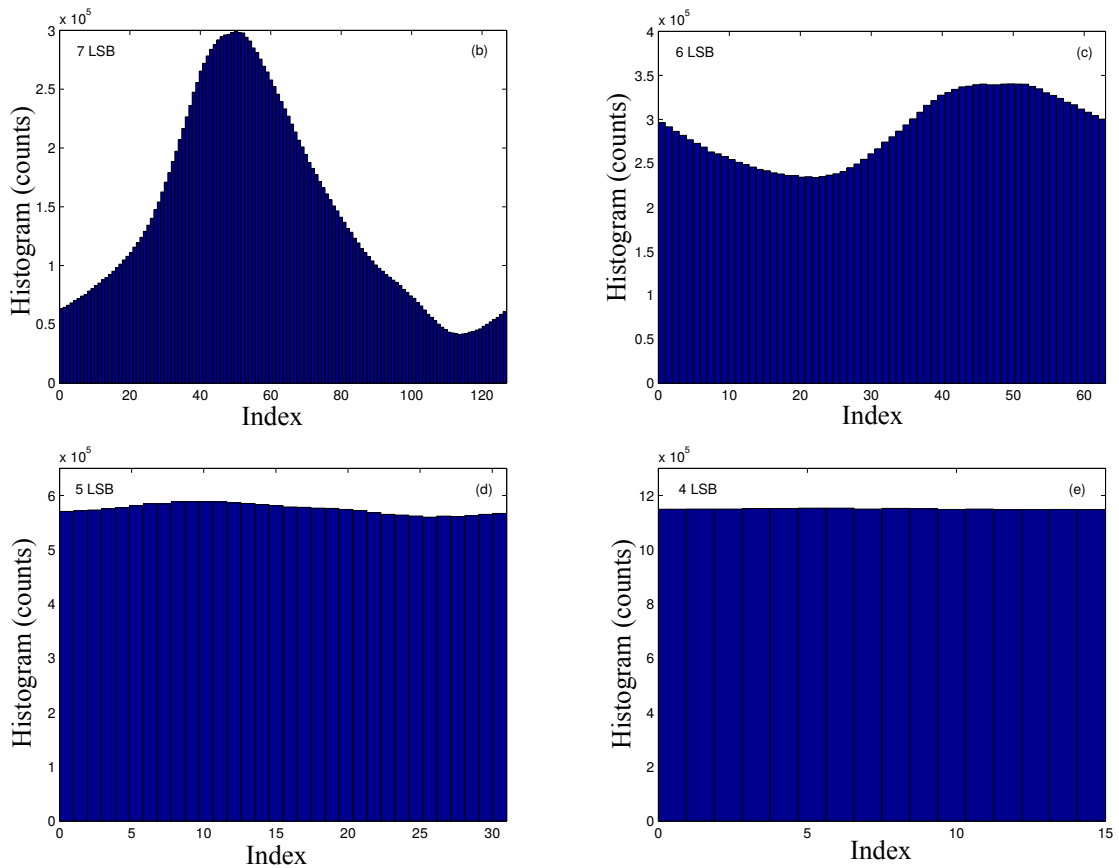
Figure 6.12: Probability density functions for (b) 7 LSBs, (c) 6 LSBs, (d) 5 LSBs and (e) 4 LSBs.

The truncation of bits can also remove the residual correlations present in the original dynamics. The number of bits necessary to remove can be estimated by plotting histograms of the truncated values until a flat histogram, within allowed statistical variation, is obtained [156]. Fig 6.12 shows the distribution for 7 to 4 bit samples from one chaotic waveform acquired under the selected optimum conditions (pump current I=19.00mA and feedback T=52.2%). The largest MSB is omitted in Fig. 6.12 (b), showing the seven least significant bits. A clear peak in the histogram is still identifiable. In Figure 6.12 (c) two of the most significant bits are excluded. The histogram becomes more uniform while its maximum starts to vanish. When only the five least significant bits are selected, the histogram becomes flatter, as figure 6.12 (d) indicates. Keeping the 4 LSB of the 8-bit data, the distribution looks uniform (Figure 6.12 (e)).

After performing this analysis, the four MSBs are discarded from each 8 bit sample, and the four least significant bits (LSBs) are retained, as illustrated in Figure 6.13. The least significant bits, obtained from points originally separated 1ns in time, form the bitstream that we evaluate for randomness using the NIST battery of statistical tests [139]. This is explained in the next section.
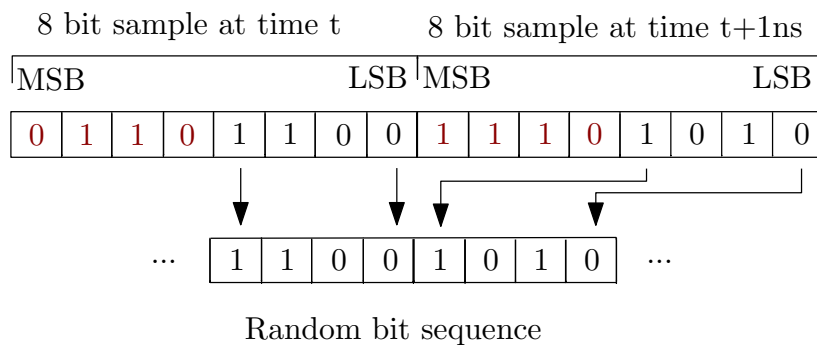
Figure 6.13: Illustration of the method used to generate the random bitstream.

6.6

Assessing the randomness

The National Institute of Standards and Technologies (NIST) provides a Statistical Test Suite for Random and Pseudorandom Number Generators for Cryptographic Applications [139]. This Test Suite consists of 15 tests that were developed to verify the randomness of a bit sequence generated by random or pseudorandom number generator. In Table 6.2, the 15 NIST tests and a short description of their main purpose of each test is provided. For an in-depth description, please see [139].

The pass criteria depends on the length of the sequence to test and a significance level α. A significance level (α), typically chosen in the range [0.001,0.01], can be defined for the tests. For assessing our data, we choose α=0.01, indicating that one would expect 1 sequence in a

hundred to be rejected. Each test is based on a calculated statistical value known as the p-value. The p-value is the probability that a perfect random bit generator would have produced a sequence less random than the sequence being tested, given the kind of non-randomness assessed by the test. Consequently, a p-value equal to 1 implies that the sequence appears to be totally random, while a p-value equal to 0 indicates that the sequence is completely non-random. From the p-value, the uniformity of p-values (also called P-value) is derived together with the Proportion as the result of the analysis. With an α=0.01, the P-value should be larger than 0.0001 and the Proportion should be in the range of 0.99 ± 0.0094392 to pass all the tests.

Statistical Test	Test Purpose
The Frequency (Mono-bit) Test	Determine whether the number of zeros and ones are approximately the same as would be expected for a truly random sequence.
Frequency Test within a Block	Determine whether the frequency of ones in an M-bit block is approximately M/2.
The Runs Test	Determine whether the number of runs (k identical bits bounded by opposite bits) of ones and zeros of different k is as expected for a random sequence.
Test for the Longest-Run-of-Ones in a Block	Determine whether the length of the longest run of ones within the tested sequence is consistent with the expected length in a random sequence.
The Binary Matrix Rank Test	Check for linear dependence among fixed length substrings of the original sequence.
The Discrete Fourier Transform (Spectral) Test	Detect periodic features in the tested sequence.
The Non-overlapping Template Matching Test	Detect generators that produce too many occurrences of a given aperiodic pattern.
The Overlapping Template Matching Test	Detect generators that produce too many occurrences of a given aperiodic pattern.
Maurer's "Universal Statistical" Test	Detect whether the sequence can be significantly compressed without loss of information.
The Linear Complexity Test	Determine whether the sequence is complex enough to be considered random.
The Serial Test	Determine whether the number of occurrences of the 2^m m-bit overlapping patterns is approximately the same as expected for a random sequence.
The Approximate Entropy Test	Compare the frequency of overlapping blocks of 2 consecutive lengths (m and m+1) with the expected result for a random sequence.
The Cumulative Sums Test	Test whether the cumulative sum of partial sequences occurring in the tested sequence is too large or too small relative to the expected for random sequences.
The Random Excursions Test	Determine if the number of visits to a particular state within a cycle deviates from what expected for a random sequence.
The Random Excursions Variant Test	Detect deviations from the expected number of visits to various states in a random walk.

Table 6.2: Description of the purposes for each NIST test. Extracted and adapted from [139].

6.7

Generation of random bit sequences

A bitstream formed from points acquired at a pump current of 19.00mA and fractional power transmission of T = 52.2% is tested using the NIST tests. As explained in previous sections, points are separated by 1ns and truncated to the 4 LSB to ensure the absence of correlations and a uniform probability density function.

The results of the NIST battery are shown in Table 6.3 for 1000 samples of 1 million bits each. For tests which produce multiple P-values, the worst case is shown. According to the criteria presented in section 6.6, all tests passed, verifying that under these conditions our system and procedure produce a statistically random bitstream. The bit rate is 4Gbit/s, based on four bits per data point, and a 1ns interval between points. This represents a successful approach to random bit generation by emphasizing the role of the dynamics over the postprocessing steps. With the bit truncation as the only processing technique, we first demonstrate the efficacy of the employed dynamics, keeping as much of the original data as possible; and second, we avoid a slow down of the final bit rate, given that bit truncation is a fast binary operation. Moreover, our speed of 4Gbit/s is competitive with recent state-of-the-art RNGs that employ more sophisticated experimental schemes and postprocessing methods.

Statistical Test	P-value (min)	Proportion	Result
Frequency	0.033584	0.9900	Success
Block Frequency	0.851383	0.9940	Success
Runs	0.090388	0.9840	Success
Longest-Run-of-Ones	0.227180	0.9930	Success
Rank	0.371941	0.9940	Success
Discrete Fourier Transform	0.699313	0.9900	Success
Non-overlapping Template	0.013102	0.9860	Success
Overlapping Template	0.044797	0.9870	Success
Maurer's Universal	0.419021	0.9870	Success
Linear Complexity	0.701366	0.9900	Success
Serial	0.180568	0.9940	Success
Approximate Entropy	0.394195	0.9930	Success
Cumulative Sums	0.179584	0.9890	Success
Random Excursions	0.126609	0.9932	Success
Random Excursions Variant	0.066528	0.9932	Success.

Table 6.3: Results of Statistical Test Suite NIST SP800-22 for a set of 1000 Sequences of 1Mbit each

6.8

Interplay of postprocessing and sampling rate

Our first results have enabled the generation of random bits at a fast rate, representing a successful approach that concentrates on the dynamical properties. In this section, we explore the role played by the dynamical properties together with the postprocessing and sampling rate used in the data acquisition process. The interplay between these factors is relevant for generating random bits at the highest bit rate the system allows. The limitations to the maximum achievable rate, which have remained unexamined so far, is also discussed.

The autocorrelation function of the captured time-series data is affected by bit truncation, in such a way that residual correlations in the original dynamics are destroyed, and thus allowing for an increase in the rate of random bit generation. This is illustrated in Fig. 6.14, which compares the AC function of the full 8 bit signal in Fig. 6.14 (a) with the AC function for the same data truncated to 4 bits in Fig. 6.14 (b). The typical AC peaks, appearing at integer multiples of the delay time τ, are completely extinguished for the truncated data. Therefore, although the AC function of the 8 bit data can provide useful criteria for choosing a dynamical regime and sample interval suitable for random bit generation [162], bit truncation can modify the characteristics such that one can dispense with some of the associated limitations. The example of Fig. 6.14, acquired for I=21mA and power transmission T of 24.7% and chosen for illustration purposes due to its high AC, indicates that the omission of the 4 MSBs represents a postprocessing procedure sufficient to eliminate natural correlations that appear in the original chaotic dynamics.

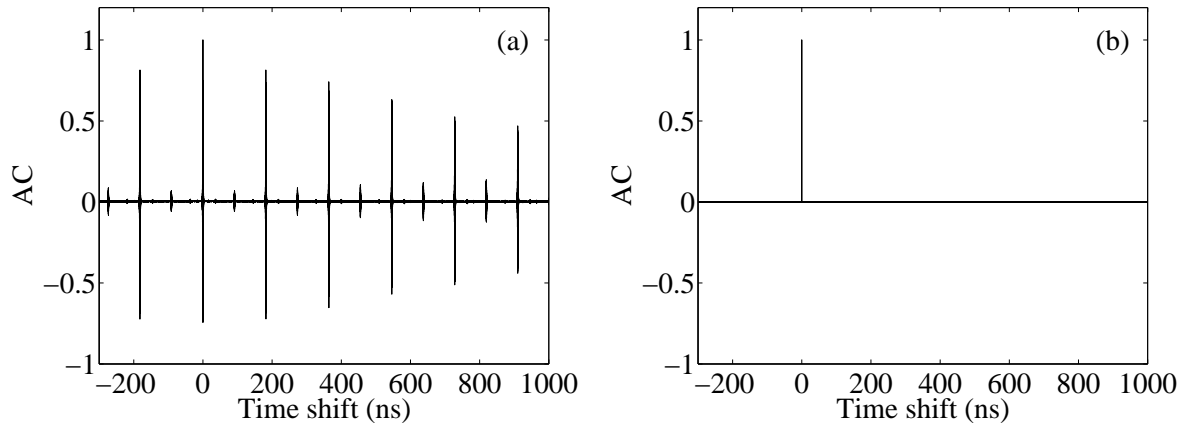Figure 6.14: (a) AC function for full 8 bits and (b) AC function for 4 LSBs obtained at pump current 21 mA and feedback strength (T) of 24.7%. Figure from [77].

Another feature of great importance is the narrowing of the zeroth AC peak. In the full data set, the decay time of this peak is typically on the order of 100ps, whereas for the truncated set this decay time is shorter. In this sense, the acquisition sampling rate might

be crucial to determine the success or failure in the generation of random bits. The sample interval of data must exceed the width of the zeroth AC peak to ensure that successive points will be independent of one another. In order to study the effect of acquisition sampling rate in the AC zeroth peak, we analyzed the AC function of the truncated bit sequences with two different sampling rates, 80GSamples/s and 40GSamples/s, but keeping the same analog bandwidth. Figure 6.15 (a) shows a zoom to the zeroth AC peak of a sequence with samples separated 12.5ps (80GSamples/s). Two neighboring samples (red dots) are correlated with a value of 0.04, whereas in Fig. 6.15 (b) two neighboring samples, spaced 25ps (40GSamples/s), have a correlation of two orders of magnitude smaller (0.0006).
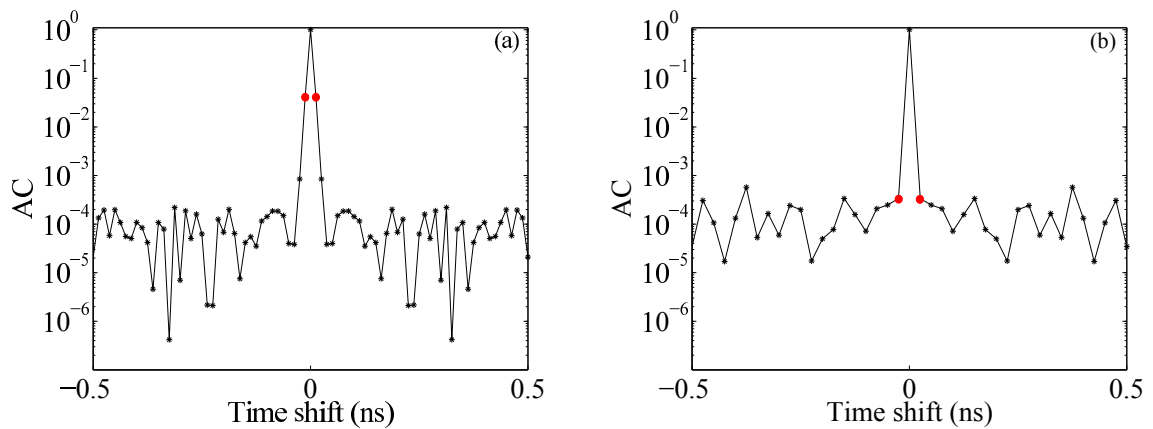
Figure 6.15: (a) AC function for 4 LSBs with a sampling rate of 80GSamples/s and (b) AC function for 4 LSBs with a sampling rate of 40GSamples/s. Both figures were acquired for I=15.00mA and T=24.7%. Figure from [77].

From the random bit generation point of view, keeping the 4 LSBs, as illustrated in Fig. 6.14 (b), can modify the AC function making the delay time signature disappear. This finding avoids the requirement of choosing a subset of points of the initial timetrace that would limit the final acquisition rate, as it was the case in previous works [146, 154, 158, 162, 168, 169]. However, Fig. 6.15 indicates that residual correlations in the truncated data also depend on the sampling rate. Time series acquired at 80Gsamples/s provide more detailed information about the temporal waveform while keeping the same analog bandwidth. This extra information results in redundances after the postprocessing, which degrade the performance of the random bit generator based on a chaotic laser. An example of this redundance is found in the non-negligible residual correlation between two consecutive points in the AC function for 4 LSBs, as depicted in Fig. 6.15 (a). Therefore, increasing the sampling rate beyond a certain threshold results in higher values for the AC of two consecutive data points. This restricts the final bit generation speed: the postprocessing together with the sampling rate must guarantee an AC function for 4 LSBs with extinguished peaks at τ and a sufficiently small neighboring correlation. Based on these investigations, a chaotic signal acquired at 40GSamples/s and truncated to the 4 LSBs presents the best compromise in

terms of acquisition rate and postprocessing.

6.9
Optimizing the bit generation rate

To generate faster random bits, we choose the optimal conditions regarding dynamics, acquisition-digitization and postprocessing. We started capturing samples at 40GSamples/s at a dynamical condition of I=15.00mA and T=24.7%, which exhibits a fast autocorrelation decay of the original dynamics and a broad power spectrum. The ratio of saturated points with respect to the maxima is controlled to 0.09%. The sampling rate of 40GSamples/s implies that sample points are separated 25ps in time. Bits are truncated from the initial signal to its 4 LSBs, having a correlation value between neighboring samples of 0.0006, as shown in Fig. 6.15 (b). To assess the statistical randomness of the bit sequences, we used a bitstream of 1Gbit that underwent the NIST tests. The results, as shown in Table 6.4, prove that we succeeded in passing all the 15 NIST tests. Following this optimized approach, we can extend the potential rate of Random Bit Sequence Generation from 4Gbit/s to 160Gbit/s, based on four bits per data point and a 25 ps interval between points. This new generation bit rate of 160Gbit/s improves by almost two orders of magnitude the bit rate previously obtained with the same system [162], being one of the highest presented so far using a simple and robust system, and requiring only minimal postprocessing.

Statistical Test	P-value (min)	Proportion	Result
Frequency	0.514124	0.9950	Success
Block Frequency	0.272977	0.9890	Success
Runs	0.150340	0.9860	Success
Longest-Run-of-Ones	0.532132	0.9890	Success
Rank	0.435430	0.9850	Success
Discrete Fourier Transform	0.524101	0.9910	Success
Non-overlapping Template	0.006152	0.9870	Success
Overlapping Template	0.715679	0.9820	Success
Maurer's Universal	0.397688	0.9820	Success
Linear Complexity	0.370262	0.9880	Success
Serial	0.152044	0.9930	Success
Approximate Entropy	0.002697	0.9930	Success
Cumulative Sums	0.239266	0.9920	Success
Random Excursions	0.033926	0.9891	Success
Random Excursions Variant	0.083893	0.9922	Success

Table 6.4: Results of Statistical Test Suite NIST SP800-22 for a Set of 1000 Sequences of 1 Mbit each. For tests producing multiple P-values and proportions, the worst case is shown. The final generation rate is 160Gbit/s.

In an attempt to increase the rate at which random bits are generated, we kept the same analog bandwidth but doubled the sampling rate to 80GSamples/s. The rest of the parameters were kept unchanged. The ratio of saturated points with respect to the maxima is again set to 0.09%. We kept only the 4 LSBs from the original timetrace, which have samples every 12.5ps. The correlation coefficient of two consecutive points for I = 15.00mA and T = 24.7% is now 0.04 for the truncated data (Fig. 6.15(a)), significantly greater than in the previous case. We tested the randomness of 1Gbit each with the NIST tests. The corresponding bit rate was 320Gbit/s but the bit sequences did not pass the majority of the 15 tests, meaning that the truncated signals acquired at 80GSamples/s are not random. To gain a better overview, we also analyzed high resolved data acquired at 80GSamples/s for other injection current and feedback strength conditions. The samples were captured such that they satisfied the above mentioned acquisition requirements and were truncated to their 4 LSBs. The outcome of the NIST tests showed again for all tested operating conditions a dramatical failure. Tests like Longest Run, Serial or Approximate Entropy tend to fail in all the dynamical cases, with a typical number of failed test that lies between 6 and 10. This finding corroborates that increasing the sampling rate further, without extending the analog bandwidth, does not lead to the generation of random bits at higher speeds.
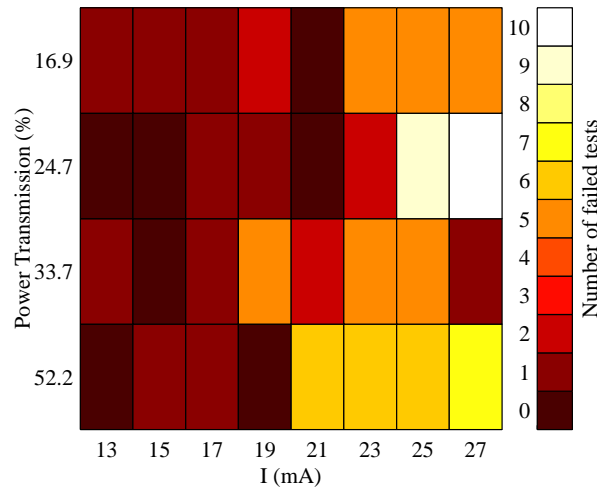
Figure 6.16: Map of number of failed NIST tests for varying feedback power transmission (T) and bias current. Figure from [77].

We checked that the successful generation of random bits reported in Table 6.4 is not a unique case. We extended our study to several operating conditions, namely different bias currents and feedback strengths. For each dynamical condition, we repeated the same criteria for the acquisition and postprocessing, based on the control of saturated values (around 0.09%) and 4 bit truncation. We acquired 1000 Samples of 1 Million bits for each dynamical case that were subjected to the NIST statistical test suite. Figure 6.16 shows the number of

failed NIST tests for different conditions of injection current and feedback strength. In the vicinity of the chosen operating point (I = 15.00mA and T = 24.7%), conditions are more favorable for random number generation for a wide range of feedback strengths. One test or no tests fail, meaning that the involved dynamics, together with the chosen acquisition conditions and postprocessing, can lead to successful random bit generation. Cases in which one NIST test fail might be optimized by adjusting slightly the analog to digital conversion. However, for injection currents larger than 23mA, the number of failed tests tends to increase significantly. This illustrates that the acquisition criteria and the omission of the 4 most significant bits is not sufficient to overcome the unsuitable dynamics of the laser with polarization-rotated optical feedback under those operating conditions.

6.9.1 Extension to 16-bit digitization

Taking advantage of the 16 bit numbers provided by the oscilloscope after the DPS, we repeated the process to discover the full potential of the system. In this case, we acquired samples at the same operating condition: I = 15.00mA and T = 24.7%. The data from the original signal were separated 25ps, and we adjusted the acquisition conditions again to have a proper number of saturated values. The number of most significant bits omitted was again 4, and we retained the 12 LSBs. We evaluated the randomness using 1000 samples of 1 Mbit data. The results, presented in Table 6.4, confirm that bit sequences, obtained under the described conditions, are sufficiently random that they pass the statistical tests of NIST. The bit generation rate for this case is 480Gbit/s (= 40 gigasamples per second × 12 LSBs). This means that if the ADCs had a resolution of 16 bits at high speeds, the attainable generation rate would be three times faster.

6.9.2 Information Theoretic limits

In this subsection, we evaluate the results from the previous section according to Information Theory. Information Theory sets the fundamental limits of information capacity in a channel in the context of communications. Therefore, it is interesting to know which are the fundamental limits of maximum bit generation rate depending on the analog bandwidth. In our scheme, we start from an analog system (chaotic laser) with dynamics of a certain bandwidth, as shown in Fig. 6.4. The analog system generates a signal which is sampled and digitized via an ADC. The maximum amount of bits one can extract from the generated waveform at a certain rate has an upper bound defined by Nyquist's theorem [170, 171]. Nyquist's theorem for a finite bandwidth noiseless channel states that the maximum channel capacity is given by:

$$maximum\ data\ rate\ (bit/s) = 2H \log_2 V \qquad (6.2)$$

Where H is the bandwidth of the dynamical system, and the digitization and V are the quantization levels. This maximum channel capacity corresponds to the maximum rate of bits one can extract from the given waveform. It is important to note that it does not

Statistical Test	P-value (min)	Proportion	Result
Frequency	0.165340	0.9960	Success
Block Frequency	0.907419	0.9920	Success
Runs	0.576961	0.9930	Success
Longest-Run-of-Ones	0.088762	0.9860	Success
Rank	0.506194	0.9920	Success
Discrete Fourier Transform	0.112708	0.9820	Success
Non-overlapping Template	0.006661	0.9900	Success
Overlapping Template	0.961039	0.9900	Success
Maurer's Universal	0.814724	0.9870	Success
Linear Complexity	0.749884	0.9920	Success
Serial	0.599693	0.9880	Success
Approximate Entropy	0.227180	0.9880	Success
Cumulative Sums	0.239266	0.9920	Success
Random Excursions	0.023412	0.9834	Success
Random Excursions Variant	0.085154	0.9934	Success

Table 6.5: Results of Statistical Test Suite NIST SP800-22 for a Set of 1000 Sequences of 1Mbit each. For tests producing multiple P-values and proportions, the worst case is shown. The final generation rate is even 480Gbit/s.

make sense to distinguish signal and noise in this case, since the noise along with the chaotic dynamics is an integral part of the signal used for random bit extraction. We benefit from a wide bandwidth of our laser, that comprises frequencies up to 20GHz, which is beyond the 3dB cutoff frequency of 16GHz from the oscilloscope. Such frequencies are present in the chaotic output of the laser, and are also involved in the whole process of generation of random bits. Therefore, we assume in Nyquist's equation 20GHz bandwidth (according to the Nyquist-Shannon sampling theorem) and the 256 discrete quantization levels (corresponding to 8 bit digitization), obtaining a maximum data rate of 320Gbit/s. However, our signal is truncated to the 4 LSBs, so only 16 discrete levels are present in our realization. In this case, the maximum channel capacity for 20GHz bandwidth and 16 quantization levels reduces to 160Gbit/s.

This result indicates that our experimental bit rate remarkably coincides with the maximum data rate provided by Information Theory, given the bandwidth of our chaotic source. Thus, we have reached the highest bit generation rate possible with our system. One should take into account that Eq. 6.2 serves as hard upper bound to the attainable bit rate. Still, real systems, due to technical limitations, might not achieve it, and approaching the maximum data rate requires optimization of the three factors described in the previous sections: dynamical conditions, acquisition and postprocessing. Still, we cannot exclude that more sophisticated tests for randomness than the NIST battery could find some remaining correlations in our random bits, which represents an interesting work to investigate in the future.

If we analyze now the case of the 80GSample/s sampling rate, the failure in generating random bits at speeds of 320Gbit/s corroborates experimentally the existence of an upper limit in the bit generation rate. This upper limit gives an estimation of the best achievable performance of the experiment beforehand, and provides a clue to what extent generated bits can rely on the underlying dynamical process. The maximum attainable bit rate depends on the analog bandwidth of the system, and cannot be improved by simply increasing the sampling rate further. Hence, tentative bit rates beyond the upper bound given by Eq. 6.2 cannot lead to the generation of random bits.

Finally, we studied the maximum data rate for 16-bit digitization given by Eq. 6.2. For 20GHz bandwidth and 2^{12} quantization levels, the maximum channel capacity is 480Gbit/s. Again, both experimental and information theoretic rates coincide. This implies that we achieved the highest speed possible for our random bit generator when truncation to the 12 LSBs is the postprocessing step applied to the chaotic signal.

With our investigations on the Information Theoretic limits, the role played by the bandwidth in the final speed of random number generators is acknowledged. Therefore, the exploration of bandwidth enhancement methods of the chaotic system (and their relevant parameters involved) should be considered in future studies of random bit generation.

6.10

Discussion

To the best of our knowledge, this is the first work in which a single laser subjected to polarization rotated optical feedback (PROF) is used to generate random bits. A semiconductor laser with PROF exhibits a rich variety of dynamical phenomena [161, 164, 172, 173], significantly different from the dynamics of other delay feedback schemes. With polarization rotated optical feedback, the returned light has crossed polarization of the outgoing electric field. The resulting interaction between TE and TM mode gives raise to unstable dynamics, characterized by chaotic fluctuations in the sub-nanosecond scale and by a fast autocorrelation delay. The rf spectrum of the laser becomes broader with PROF, covering frequencies beyond 10 GHz. Besides, polarization rotated feedback can exhibit strong chaos, and does not require the polarization state of light to be maintained along the entire setup, making it specially favorable for chaotic applications.

We have proven the validity of the PROF dynamics for the application of random bit generation. However, numerical simulations of the system could provide the opportunity to gain more insight into the dynamics of the system, exploring parameters that are difficult to access in the experiments. A model for a semiconductor laser with polarization rotated feedback would be typically simulated by a rate equation model with two orthogonal linearly polarized electric fields [161, 172]. The majority of the theoretical models focused on the situation where a single mode, usually the TE, was rotated and injected into the TM mode. This situation corresponds to a unidirectional coupling of polarization modes (TE $\rightarrow$ TM). Nevertheless, in the more general scenario, which also corresponds to our experimental

scheme, both polarization modes are rotated and injected into the corresponding orthogonal modes, leading to a bidirectional coupling between them (TE $\leftrightarrow$ TM).

The proposed rate equations for the TE and TM modes are described as follows (for simplicity, we substitute the subscripts $\{TE, TM\}$ by $\{1, 2\}$):

$$\frac{dE_1(t)}{dt} = \frac{1}{2}(1 + i\alpha)\{G_1[N(t) - N_0] - \gamma_{p,1}\}E_1(t) + \kappa_1 E_2(t - \tau) \tag{6.3}$$

$$\frac{dE_2(t)}{dt} = \frac{1}{2}(1 + i\alpha)\{G_2[N(t) - N_0] - \gamma_{p,2}\}E_2(t) + \kappa_2 E_1(t - \tau) - i\Delta\omega E_2(t) \tag{6.4}$$

$$\frac{dN(t)}{dt} = J - \gamma_s N(t) - [N(t) - N_0]\{G_1|E_1(t)|^2 + G_2|E_2(t)|^2\} \tag{6.5}$$

$$\tag{6.6}$$

where E is the electric field for every polarization mode. N is the carrier density and $\Delta\omega$ is the frequency detuning $\omega_1 - \omega_2$. The detuning is given relative to the TE mode frequency. $G_{1,2}$ are the gain coefficients, and N_0 is the carrier density at transparency. $\gamma_{p,1,2}$ are the inverse of the photon lifetime, $\kappa_{1,2}$ are the feedback strength, and γ_s is the inverse of the carrier lifetime. The delay time of the external loop is denoted by τ, α is the linewidth enhancement factor, and J is the current density. Other changes in phase, due to propagation in the external cavity or reflections from optical elements, should also be included for a more complete version of the model.

This type of delayed optical feedback has been less studied in comparison with coherent optical feedback. Particularly, the model with bidirectional injection between modes has not been used experimentally in detail. Albeit numerical simulations were beyond the scope of this thesis, we cannot omit the fact that conducting simulations can help to easily explore the parameter dependence, and provide some hints for the best operating conditions beforehand.

The development of our random bit generator has been carried out with two essential approaches. In the first approach, we focused on the dynamical properties, looking for the optimal features for randomness: unpredictability of the laser output in a strong chaos regime, characterized by the loss of memory with fast AC decay, and a broad rf spectra that allows for high bit generation rates. With such ingredients and a postprocessing step, we generated random bits at 4Gbit/s, proving the effectiveness of the dynamical criteria for random bit generation. In the second approach, we aimed for a better understanding of the capabilities and limitations of the generator, exploring the interplay between all the factors involved in the process: dynamics together with acquisition conditions and postprocessing. Knowing how each of these steps affect the next one, can optimize the system significantly, improving the performance of the random bit generator to a bit rate up to 160Gbit/s. The fast generation rate of our random bit generator is not its only advantage. Since its components are made of standard telecom components, is also suitable for fiber-optic communication purposes. Nevertheless, the postprocessing is still performed offline. Other works have gone a step further, and have implemented a real-time random bit generator with typically slower bit rates [159, 174]. Whether our random bit generator would suffer from a slowdown in the real-time generation rate in favor of robustness is an unresolved issue at the moment.

To assert the randomness of the bits, we have trusted the outcome of the NIST tests. They are the most commonly used test batteries but there exist other test suites, like Diehard or ENT [175, 176] that could also be applied to complement the statistics. In this sense, more sophisticated techniques of assessing the randomness could determine that our bitstream is not completely unpredictable. However, none of these tests can ultimately prove randomness. To prove definitely that a given sequence of bits is random, we would need that sequence to be infinite, which is, from a practical point of view, impossible.

All physical random bit generators presented to date have verified the quality of their random bits through the mentioned tests for randomness, with the constraint that it entails. Therefore, there is some disagreement about which process (or even a combination of them) is better to generate random bits. The use of a given method is often related to its final application. The deterministic nature of a pseudo-random bit generator can turn beneficial for simulation and modeling, in which replaying the same sequence of numbers again might be required, and having recurrences after 2^{32} bits is acceptable. Other applications, such as data encryption keys, games or gambling, are best served by a physical random bit generator.

Less clear is the choice between a quantum bit generator and a chaos-based bit generator. There is this tendency to think that quantum bit generators are truly random since they are based on quantum mechanics, a nondeterministic behavior. But still, quantum generators are not exempt from critique. Some scientists argue that the events at the subatomic level are not random but deterministic, and its behavior seems random to us because no proper measurement technique has been developed. The truth is that these type or generators often require the use of another physical process to guarantee the randomness, as well as some sort of postprocessing. In turn, they are less efficient than the chaos-based generators. With the use of semiconductor lasers as source of randomness, we have the best of both worlds: the spontaneous emission noise, quantum in origin, is amplified by the chaotic attractor leading to unpredictable dynamical behavior.

Another point in question is related to the role of noise in the system. Random bit generators based on chaotic lasers have two contributions to the unpredictability: the deterministic chaotic dynamics, and the noise coming from different sources of the system and detection. It is a topic of discussion how noise and chaos contribute to the randomness of the bits. Some approaches have been reported recently [74, 75] to investigate how the entropy of bits depends on the inherent noise and the dynamical properties of the laser. Mikami et al. [74] simulated a chaotic laser with white noise of small amplitude to extract one bit from the optical intensity at every sampling step. Their results show that, starting from the same initial state, there is an increase of entropy of the bit extracted with time, due to the divergence of trajectories corresponding to different noise cases. Hagerstrom et al. [75] used a photon-counting optoelectronic feedback oscillator to investigate how the entropy rate can reflect the deterministic or stochastic features of the system, depending on the bandwidth and resolution of the measurement device. Determining the weights of noise and chaotic dynamics to the randomness of the bits in our chaotic laser system is an interesting topic to investigate.

The field of random bit generation continues to be an an exciting area of research with

constant advancements. New approaches to physical and pseudo random bit generators are being developed, focusing on applications such as secure key distribution. In 2012, a first experimental method for secure key distribution was reported by Yoshimura et al. [177] with generation rates of 2 Mbit/s. The implementation was based on the synchronization of two mutually coupled chaotic lasers driven by a common random optical signal. Although the work of Yoshimura at al. utilized semiconductor lasers, other physical schemes like Quantum Key Distribution have been reported [178]. Future work on the topic should also focus on a more feasible and user-friendly implementation of the random bit generators. Sanguinetti et al. [179] demonstrated recently that a mobile phone's camera can be used to generate random bits. Whether random bit generators can be implemented in hardware at lower costs and at speeds above the electronic bottleneck is an interesting challenge for the future.

6.11

Summary

We have presented a simple, robust and versatile semiconductor laser system whose chaotic dynamics is used for random bit generation. We have shown how chaotic dynamics from a laser subjected to PROF, with fast oscillations and broad power spectrum, is a prerequisite to generate randomness. Other factors need to be addressed when designing a random number generator based on a chaotic laser: dynamical properties of the system, acquisition and digitization conditions, and postprocessing of the original signal. We have shown how understanding the interplay between them is crucial to improve the performance of a random bit generator.

We have derived clear guidelines using simple procedures that can be applied to other chaos-based systems. In particular, an appropriate adjustment of the analog to digital conversion implies less stringent conditions in the postprocessing to ensure random bits. At the same time, bit truncation is a necessary but not sufficient condition for random bit generation, and requires the combination of suitable dynamics and acquisition conditions. The zeroth AC peak of the truncated signal also provides important information for the maximum sampling rate allowed, showing residual correlations between neighboring samples when the sampling rate is too high.

We also connected the maximum achievable rate of random bit generation to Information Theory considerations, and investigated the existence of an upper bound to the bit generation rate related to the analog bandwidth of the system. With the proper balance, a simple system based on a semiconductor laser with feedback can be used to generate random bits with the information theoretically highest possible rates of to 160Gbit/s for 8 bit digitization and 480Gbit/s for 16 bit digitization. This new and deeper understanding of the interaction between involved mechanisms may have broad applicability and lead to significant improvements of other chaos-based random bit generators.

This work illustrates the relevance, not only of semiconductor lasers with delayed feedback as a robust and versatile scheme for random bit generation, but also of photonic technology,

in general, as a perfect platform for the development of high-speed systems to be used in cryptography, an active research field with growing perspectives.

Conclusions and future work

"Science never solves a problem
without creating ten more."

George Bernard Shaw,
Dramatist.

7.1
Conclusions

Photonic systems are powerful test-beds for the investigation of complex dynamics emerging from delays in feedback or coupling. The aim of this Thesis was to study two relevant properties of photonic delay systems with direct applications in current information processing and encryption systems: consistency and unpredictability. We characterized the ability of laser systems with delay to exhibit, on the one hand, reliable complex dynamics when an external stimulus is applied, and on the other hand, unpredictable complex behavior, depending on the operating conditions. Consistency properties have been studied as a necessary condition for the implementation of Reservoir Computing schemes. The property of unpredictability has been exploited in the application of random bit generation with a chaotic semiconductor laser.

For the characterization of the consistency properties, we used three different schemes based on a semiconductor lasers systems with delay. In the first scheme, we investigated consistency of a semiconductor laser to its own time-delayed feedback, so that the drive was the self-generated complex signal, and the response system was the semiconductor laser itself. The idea behind it was to drive the laser system twice with the same chaotic input, and compare whether the corresponding responses were consistent. This required a high accuracy in the repetition of the drive, which we achieved with the design of a fiber-optic setup with a second feedback loop in which the chaotic drive was stored, for the first time, optically. The high quality of the experiment allowed us to illustrate the occurrence of transitions between consistent and inconsistent responses in the laser, and characterize their dependence

on the drive signal and operating condition. The results could be associated to a change in dynamical conditions from weak to strong chaos. But more importantly, the experiment allowed for the extraction of the σ value, a direct indicator of the sub-Lyapunov exponent, and therefore, of the degree of consistency, which until now was obtainable only from numerical simulations. The proportionality between σ and λ_0 was demonstrated numerically, and unveiled its dependence on the linewidth enhancement factor of the laser.

The next step was to extend the study to the use of a semiconductor laser system with excitability properties subject to electrical input pulse trains. Here, two different pulse trains modulating the pump current of the laser were used as drives, while the semiconductor laser with delayed feedback operating in the chaotic regime of Low Frequency Fluctuations acted as response system. The purpose of this experiment was to study the possibility and requirements to induce a consistent response, particularly the power drop-out, with the injection of a short pulse. At slow timescales, the system showed a clear dependence on the temporal pattern of the pulses, as the contrast between the inter- and intra-correlations illustrated. The analysis also showed that the amplitude of the pulses was a significant parameter, highlighted by the existence of an optimum range of amplitudes where the system displayed excitability-like properties without being completely enslaved by the drive. This setup aimed to shed light on the way neurons respond to short inputs in a chaotic environment. The obtained results are relevant for a better understanding of neural information processing in the brain.

To complement the investigations on consistency, the last drive-response scheme used was an electro-optic intensity oscillator driven by 3 scalar signals: an harmonic waveform, a sequence of pulses, and recorded time-traces from the autonomous dynamics. Under certain conditions, the response system can show hysteresis and coexistence of multistable states. Still, we found that consistency can be achieved. A common feature of the setups investigated was the higher inter-correlations values with respect to the intra-correlation values. Our study showed that when the autonomous dynamics were periodic or period doubled, a consistent response was obtained independent of the drive. In cases of bistable dynamics, new sorts of consistency were discovered, like reproducible time-position transitions between the two states. The ability of the oscillator to sustain partial consistency in the global chaos regime when the drive was a chaotic time trace generated by the system, opens the door to uses of reservoir computing at other operating conditions.

The last Chapter of this Thesis was devoted to the use of the unpredictable dynamics for the generation of random bits. A semiconductor laser with polarization rotated feedback was utilized to provide chaotic dynamics characterized by randomness-like features, including a flat broad spectrum, suppression of the delay echoes of the autocorrelation function and no recurrences in the temporal oscillations. Such conditions can be associated with a regime of strong chaos. Nevertheless, we found that other factors like the data acquisition and the postprocessing of the signal also affected the randomness of the finally generated bits. We demonstrated that the right balance between all the factors that come into play is crucial for the optimum performance of the system. The validity of our guidelines was proven with our random bit generator, enhancing its generation rate up to 160Gbit/s. This represents the

fastest bit rate achieved with a single laser and minimum postprocessing to date. We also predicted the potential of any random bit generator by using Information Theory to link the maximum achievable rate with the bandwidth of the system.

7.2
Future work

Interesting and promising results have been found in the different systems presented in this Thesis. However, there are still many open questions to address in future work. Consistency in nonlinear systems is a novel concept, lacking a mathematical definition, and whose relation with generalized synchronization is still under debate. It would be interesting to extend the implementation of the experimental method and analysis for the extraction of σ to other nonlinear oscillators.

Although we made steps towards a better understanding of the existing requirements for a consistent response, the full range of involved parameters were not covered in our study. The frequency and amplitude of the scalar drives and their relation with the autonomous dynamics could be a subject for a more detailed investigation. Regarding the ability to induce a consistent response to a drive in an excitable system, more suited forms of perturbations could be designed to trigger a characteristic response like a power-dropout. Complementing these measurements with other techniques, like the period-resolved inter-correlation in the case of harmonic drives, could shed some light on the role of time evolution in consistency. The phenomenon of temporally consistent switching between states also deserves deeper studies.

In the particular case of the Ikeda oscillator, future investigations should focus on the mechanisms underlying the loss of consistency when approaching the chaotic regime, taking into account that such system only displays weak chaos and, therefore, a consistent behavior should be possible. Another interesting topic to explore is the reason behind the higher level of consistency when the drive is a chaotic waveform generated by the system. A better understanding of these aspects might allow for consistent responses in the global chaos regime.

Concerning random bit generators based on chaotic lasers, ongoing work will concentrate on the development of methods to increase the final bit rate. Technological improvements that allow for higher sampling rates and broader analog bandwidths of the oscilloscope, together with faster postprocessing steps, might be a good strategy. From a more fundamental point of view, the contribution of the inherent noise to the randomness of the final bits is not yet characterized in our system, and represents an exciting challenge for the future.

Bibliography

[1] T. Erneux. *Applied delay differential equations*, volume 3. Springer Science & Business Media, New York, 2009.

[2] R. J. Kosinski. A literature review on reaction time. *Clemson University, South Carolina*, 10, 2008.

[3] G. Orosz, R. E. Wilson, R. Szalai, and G. Stépán. Exciting traffic jams: nonlinear phenomena behind traffic jam formation on highways. *Physical Review E*, 80(4):046205, 2009.

[4] T. Vyhlidal. *Analysis and Synthesis of Time Delay System Spectrum [Ph. D. dissertation]*. Czech Technical University, 2003.

[5] P. Fleurquin, J. J. Ramasco, and V. M. Eguiluz. Systemic delay propagation in the us airport network. *Scientific Reports*, 3, 2013.

[6] Kestutis Pyragas. Continuous control of chaos by self-controlling feedback. *Physics Letters A*, 170(6):421–428, 1992.

[7] Y. Liu, N. Kikuchi, and J. Ohtsubo. Controlling dynamical behavior of a semiconductor laser with external optical feedback. *Physical Review E*, 51(4):R2697, 1995.

[8] R. N. Hall, G. E. Fenner, J. D. Kingsley, T. J. Soltys, and R. O. Carlson. Coherent light emission from gaas junctions. *Physical Review Letters*, 9:366–369, 1962.

[9] M. I. Nathan, W. P. Dumke, G. Burns, F. H. Dill Jr., and G. Lasher. Stimulated emission of radiation from gaas pn junctions. *Applied Physics Letters*, 1:62–64, 1962.

[10] T. M. Quist, R. H. Rediker, R. J. Keyes, W. E. Krag, B. Lax, A. L. McWhorter, and H. J. Zeigler. Semiconductor maser of GaAs. *Applied Physics Letters*, 1:91–92, 1962.

[11] R. F. Broom. Self modulation at gigahertz frequencies of a diode laser coupled to an external cavity. *Electronics Letters*, 5(23):571–572, 1969.

[12] C. Risch, C. Voumard, F. K. Reinhart, and R. Salathe. External-cavity-induced nonlinearities in the light versus current characteristic of (Ga, Al) As continuous-wave diode lasers. *IEEE Journal of Quantum Electronics*, 13(8):692–696, 1977.

[13] C. H. Henry and R. F. Kazarinov. Instability of semiconductor lasers due to optical feedback from distant reflectors. *IEEE Journal of Quantum Electronics*, 22(2):294–301, 1986.

[14] G. Giacomelli, M. Calzavara, and F. T. Arecchi. Instabilities in a semiconductor laser with delayed optoelectronic feedback. *Optics Communications*, 74(1):97–101, 1989.

[15] C. O. Weiss and R. Vilaseca. *Dynamics of lasers*. VCH Verlag, Weinheim, 1991.

[16] F. T. Arecchi, G. Giacomelli, A. Lapucci, and R. Meucci. Dynamics of a co_2 laser with delayed feedback: The short-delay regime. *Physical Review A*, 43(9):4997, 1991.

[17] J. Ohtsubo. *Semiconductor lasers: stability, instability and chaos*. Springer, Berlin, 2nd ed. edition, 2007.

[18] K. Lüdge. *Nonlinear laser dynamics: from quantum dots to cryptography*. Wiley-VCH, Weinheim, 2012.

[19] A. Uchida. *Optical communication with chaotic lasers: applications of nonlinear dynamics and synchronization*. Wiley-VCH, Weinheim, 2012.

[20] A. Argyris, D. Syvridis, L. Larger, V. Annovazzi-Lodi, P. Colet, J. García-Ojalvo I. Fischer, C. R. Mirasso, L. Pesquera, and K. A. Shore. Chaos-based communications at high bit rates using commercial fiber-optic links. *Nature*, 438(18):343–346, 2005.

[21] L. Larger and J.-P. Goedgebuer. Encryption using chaotic dynamics for optical telecommunications. *Comptes Rendus Physique*, 5, 2004.

[22] C. R. Mirasso, P. Colet, and P. Garcia-Fernandez. Synchronization of chaotic semiconductor lasers: Application to encoded communications. *IEEE Photonics Technology Letters*, 8:299, 1996.

[23] M. Peil, I. Fischer, W. Elsäßer, S. Bakic, N. Damaschke, C. Tropea, S. Stry, and J. Sacher. Rainbow refractometry with a tailored incoherent semiconductor laser source. *Applied Physics Letters*, 89:091106, 2006.

[24] F. Y. Lin and J. M. Liu. Chaotic lidar. *IEEE Journal of Selected Topics in Quantum Electronics*, 10:991–997, 2004.

[25] A. Uchida, K. Amano, M. Inoue, K. Hirano, S. Naito, H. Someya, I. Oowada, T. Kurashige, M. Shiki, S. Yoshimori, K. Yoshimura, and P. Davis. Fast physical random bit generation with chaotic semiconductor lasers. *Nature Photonics*, 2:728–732, 2008.

[26] L. Larger, M. C. Soriano, D. Brunner, L. Appeltant, J. M. Gutierrez, L. Pesquera, C. R. Mirasso, and I. Fischer. Photonic information processing beyond Turing: an

optoelectronic implementation of reservoir computing. *Optics Express*, 20(3):3241–3249, 2012.

[27] A. Chraplyvy R. Tkach. Regimes of feedback effects in 1.5-μm distributed feedback lasers. *Journal of Lightwave Technology*, 4(11):1655–1661, 1986.

[28] T. Heil, I. Fischer, W. Elsäßer, and A. Gavrielides. Dynamics of semiconductor lasers subject to delayed optical feedback: The short cavity regime. *Physical Review Letters*, 87(24):243901, 2001.

[29] I. Fischer, T. Heil, and W. Elsäßer. Emission dynamics of semiconductor lasers subject to delayed optical feedback: an experimentalists perspective. In *Nonlinear Laser Dynamics: Concepts, Mathematics, Physics, and Applications International Spring School*, volume 548, pages 218–237. AIP Publishing, 2000.

[30] M. C. Soriano, J. García-Ojalvo, C. R. Mirasso, and I. Fischer. Complex photonics: Dynamics and applications of delay-coupled semiconductors lasers. *Reviews of Modern Physics*, 85:421, 2013.

[31] Laurent Larger. Complexity in electro-optic delay dynamics: modelling, design and applications. *Philosophical Transactions of the Royal Society of London A: Mathematical, Physical and Engineering Sciences*, 371(1999):20120464, 2013.

[32] D. W. Sukow, A. Gavrielides, T. Erneux, B. Mooneyham, K. Lee, J. McKay, and J. Davis. Asymmetric square-waves in mutually-coupled semiconductor lasers with orthogonal optical injection. *Physical Review E*, 81:025206R, 2010.

[33] S. Yanchuk and P. Perlikowski. Delay and periodicity. *Physical Review E*, 79(4):046221, 2009.

[34] J. Mørk, B. Tromborg, and J. Mark. Chaos in semiconductor lasers with optical feedback: theory and experiment. *IEEE Journal of Quantum Electronics*, 28(1):93–108, 1992.

[35] J. Ye, H. Li, and J. G. McInerney. Period-doubling route to chaos in a semiconductor laser with weak optical feedback. *Physical Review A*, 47(3):2249, 1993.

[36] G. C. Dente, P. S. Durkin, K. A. Wilson, and C. E. Moeller. Chaos in the coherence collapse of semiconductor lasers. *IEEE Journal of Quantum Electronics*, 24:2441–2447, 1988.

[37] K. Ikeda and K. Matsumoto. High-dimensional chaotic behavior in systems with time-delayed feedback. *Physica D: Nonlinear Phenomena*, 29(1):223–235, 1987.

[38] J. Mørk, P. Christiansen, and B. Tromborg. Bistability and low-frequency fluctuations in semiconductor lasers with optical feedback: A theoretical analysis. *IEEE Journal of Quantum Electronics*, 24:123–133, 1988.

[39] J. Mørk, J. Mark, and B. Tromborg. Route to chaos and competition between relaxation oscillations for a semiconductor laser with optical feedback. *Physical Review Letters*, 65(16):1999, 1990.

[40] Takuya Sano. Antimode dynamics and chaotic itinerancy in the coherence collapse of semiconductor lasers with optical feedback. *Physical Review A*, 50(3):2719, 1994.

[41] G. H. M. Van Tartwijk, A. M. Levine, and D. Lenstra. Sisyphus effect in semiconductor lasers with optical feedback. *IEEE Journal of Selected Topics in Quantum Electronics*, 1(2):466–472, 1995.

[42] D. Lenstra, B.Verbeek, and A. Den Boef. Coherence collapse in single-mode semiconductor lasers due to optical feedback. *IEEE Journal of Quantum Electronics*, 21:674–679, 1988.

[43] I. Fischer, G. H. M. Van Tartwijk, A. M. Levine, W. Elsässer, E. Göbel, and D. Lenstra. Fast pulsing and chaotic itinerancy with a drift in the coherence collapse of semiconductor lasers. *Physical Review Letters*, 76(2):220, 1996.

[44] T. Heil, I. Fischer, and W. Elsäßer. Coexistence of low-frequency fluctuations and stable emission on a single high-gain mode in semiconductor lasers with external optical feedback. *Physical Review A*, 58(4):R2672, 1998.

[45] M. Peil, M. Jacquot, Y. K. Chembo, L. Larger, and T. Erneux. Routes to chaos and multiple time scale dynamics in broadband bandpass nonlinear delay electro-optic oscillators. *Physical Review E*, 79(2):026208, 2009.

[46] L. Larger and J. M. Dudley. Nonlinear dynamics: Optoelectronic chaos. *Nature*, 465(7294):41–42, 2010.

[47] K. Ikeda, K. Kondo, and O. Akimoto. Successive higher-harmonic bifurcations in systems with delayed feedback. *Physical Review Letters*, 49(20):1467, 1982.

[48] T. Erneux, F. Rogister, A. Gavrielides, and V. Kovanis. Bifurcation to mixed external cavity mode solutions for semiconductor lasers subject to optical feedback. *Optics Communications*, 183(5):467–477, 2000.

[49] T. Erneux, L Larger, M. W. Lee, and J.-P. Goedgebuer. Ikeda hopf bifurcation revisited. *Physica D: Nonlinear Phenomena*, 194(1):49–64, 2004.

[50] J. Sacher, W. Elsässer, and E. O. Göbel. Intermittency in the coherence collapse of a semiconductor laser with external feedback. *Physical Review Letters*, 63(20):2224–2227, 1989.

[51] L. M. Pecora and T. L. Carroll. Synchronization in chaotic systems. *Physical Review Letters*, 64:821–824, Feb 1990.

[52] S. Boccaletti, J. Kurths, G. Osipov, D.L. Valladares, and C.S. Zhou. The synchronization of chaotic systems. *Physics Reports*, 366(1-2):1–101, August 2002.

[53] A. Pikovsky, M. Rosenblum, and J. Kurths. *Synchronization: A universal concept in nonlinear sciences*, volume 12. Cambridge University Press, Cambridge, 2003.

[54] Sebastian M. Wieczorek. Noise synchronisation and stochastic bifurcations in lasers. In Kathy Lüdge, editor, *Nonlinear Laser Dynamics: From Quantum Dots to Cryptography*. Wiley-VCH Verlag GmbH & Co. KGaA, Weinheim, 2011.

[55] K. Klemm and S. Bornholdt. Topology of biological networks and reliability of information processing. *Proceedings of the National Academy of Sciences of the United States of America*, 102(51):18414–18419, 2005.

[56] A. J. Peters, S. X. Chen, and T. Komiyama. Emergence of reproducible spatiotemporal activity during motor learning. *Nature*, 510(7504):263–267, 2014.

[57] D. Brunner, M. C. Soriano, C. R. Mirasso, and I. Fischer. Parallel photonic information processing at gigabyte per second data rates using transient states. *Nature Communications*, 4:1364, 2013.

[58] Edward N. Lorenz. Deterministic nonperiodic flow. *Journal of the Atmospheric Sciences*, 20(2):130–141, 1963.

[59] K. M. Cuomo, A. V. Oppenheim, and S. H. Strogatz. Synchronization of lorenz-based chaotic circuits with applications to communications. *IEEE Transactions on Circuits and systems II: Analog and digital signal processing*, 40(10):626–633, 1993.

[60] A. Uchida, F. Rogister, J. García-Ojalvo, and R. Roy. Synchronization and communication with chaotic laser systems. *Progress in Optics*, 48:203–341, 2005.

[61] E. Klein, N. Gross, E. Kopelowitz, M. Rosenbluh, L. Khaykovich, W. Kinzel, and I. Kanter. Public-channel cryptography based on mutual chaos pass filters. *Physical Review E*, 74(4):046201, 2006.

[62] R. Vicente, C. R. Mirasso, and I. Fischer. Simultaneous bidirectional message transmission in a chaos-based communication scheme. *Optics Letters*, 32(4):403–405, 2007.

[63] K. Myneni, T. A. Barr, B. R. Reed, S. D. Pethel, and N. J. Corron. High-precision ranging using a chaotic laser pulse train. *Applied Physics Letters*, 78(11):1496–1498, 2001.

[64] F. Y. Lin and J. M. Liu. Chaotic radar using nonlinear laser dynamics. *IEEE Journal of Quantum Electronics*, 40(6):815–820, 2004.

[65] K. E. Chlouverakis and M. J. Adams. Optoelectronic realisation of nor logic gate using chaotic two-section lasers. *Electronics Letters*, 41(6):359–360, 2005.

[66] N. F. Rulkov, M. M. Sushchik, L. S. Tsimring, and H. D. I. Abarbanel. Generalized synchronization of chaos in directionally coupled chaotic systems. *Physical Review E*, 51(2):980–994, 1995.

[67] H. D. I. Abarbanel, N. F. Rulkov, and M. M. Sushchik. Generalized synchronization of chaos: The auxiliary system approach. *Physical Review E*, 53:4528–4535, May 1996.

[68] A. Uchida, R. McAllister, R. Meucci, and R. Roy. Generalized Synchronization of Chaos in Identical Systems with Hidden Degrees of Freedom. *Physical Review Letters*, 91(17):174101, 2003.

[69] S. Lepri, G. Giacomelli, A. Politi, and F. T. Arecchi. High-dimensional chaos in delayed dynamical systems. *Physica D: Nonlinear Phenomena*, 70(3):235–249, 1994.

[70] S. Heiligenthal, T. Dahms, S. Yanchuk, T. Jüngling, V. Flunkert, I. Kanter, E. Schöll, and W. Kinzel. Strong and weak chaos in nonlinear networks with time-delayed couplings. *Physical Review Letters*, 107:234102, 2011.

[71] T. Jüngling, M. C. Soriano, and I. Fischer. Determining the sub-lyapunov exponent of delay systems from time series. *Physical Review E*, 91(6):062908, 2015.

[72] J. P. Eckmann and D. Ruelle. Ergodic theory of chaos and strange attractors. *Reviews of Modern Physics*, 57(3):617, 1985.

[73] G. Boffetta, M. Cencini, M. Falcioni, and A. Vulpiani. Predictability: a way to characterize complexity. *Physics Reports*, 356(6):367–474, 2002.

[74] T. Mikami, K. Kanno, K. Aoyama, A. Uchida, T. Ikeguchi, T. Harayama, S. Sunada, K. Arai, K. Yoshimura, and P. Davis. Estimation of entropy rate in a fast physical random-bit generator using a chaotic semiconductor laser with intrinsic noise. *Physical Review E*, 85:016211, 2012.

[75] A. M. Hagerstrom, T. E. Murphy, and R. Roy. Harvesting entropy and quantifying the transition from noise to chaos in a photon-counting feedback loop. *Proceedings of the National Academy of Sciences*, 112(30):9258–9263, 2015.

[76] C. E. Shannon and W. Weaver. *The Mathematical Theory of Communication*. University Illinois Press, Urbana, 1963.

[77] N. Oliver, M. C. Soriano, D. W. Sukow, and I. Fischer. Fast random bit generation using a chaotic laser: Approaching the information theoretic limit. *IEEE Journal of Quantum Electronics*, 49(11):910–918, 2013.

[78] H. Kantz and T. Schreiber. *Nonlinear time series analysis*, volume 7. Cambridge university press, Cambridge, 2004.

[79] Z. F. Mainen and T. J. Sejnowski. Reliability of spike timing in neocortical neurons. *Science*, 268(5216):1503–1506, 1995.

[80] W. Maass, T. Natschläger, and H. Markram. Real-time computing without stable states: A new framework for neural computation based on perturbations. *Neural computation*, 14(11):2531–2560, 2002.

[81] L. Appeltant, M. C. Soriano, G. Van der Sande, J. Danckaert, S. Massar, J. Dambre, B. Schrauwen, C. R. Mirasso, and I. Fischer. Information processing using a single dynamical node as complex system. *Nature Communications*, 2:468, 2011.

[82] Y. Paquot, F. Duport, A. Smerieri, J. Dambre, B. Schrauwen, M. Haelterman, and S. Massar. Optoelectronic reservoir computing. *Scientific Reports*, 2:287, 2012.

[83] A. Uchida, R. McAllister, and R. Roy. Consistency of Nonlinear System Response to Complex Drive Signals. *Physical Review Letters*, 93(24):244102, 2004.

[84] G. Giacomelli, S. Barland, M. Giudici, and A. Politi. Characterizing the response of chaotic systems. *Physical Review Letters*, 104(19):194101, 2010.

[85] K. Kanno and A. Uchida. Consistency and complexity in coupled semiconductor lasers with time-delayed optical feedback. *Physical Review E*, 86(6):066202, 2012.

[86] N. Oliver, T. Jüngling, and I. Fischer. Consistency properties of a chaotic semiconductor laser driven by optical feedback. *Physical Review Letters*, 114(12):123902, 2015.

[87] W.-H. Kye, M. Choi, M. Kurdoglyan, C.-M. Kim, and Y.-J. Park. Synchronization of chaotic oscillators due to common delay time modulation. *Physical Review E*, 70(4):046211, 2004.

[88] T. Yamamoto, I. Oowada, H. Yip, A. Uchida, S. Yoshimori, K. Yoshimura, J. Muramatsu, S.-I. Goto, and P. Davis. Common-chaotic-signal induced synchronization in semiconductor lasers. *Optics Express*, 15(7):3974–80, 2007.

[89] I. Oowada, H. Ariizumi, M. Li, S. Yoshimori, A. Uchida, K. Yoshimura, and P. Davis. Synchronization by injection of common chaotic signal in semiconductor lasers with optical feedback. *Optics Express*, 17(12):10025–10034, 2009.

[90] H. Aida, M. Arahata, H. Okumura, H. Koizumi, A. Uchida, K. Yoshimura, J. Muramatsu, and P. Davis. Experiment on synchronization of semiconductor lasers by common injection of constant-amplitude random-phase light. *Optics Express*, 20(11):11813–11829, 2012.

[91] S. Sunada, K. Arai, K. Yoshimura, and M. Adachi. Optical phase synchronization by injection of common broadband low-coherent light. *Physical Review Letters*, 112:204101, 2014.

[92] X. Porte, M. C. Soriano, and I. Fischer. Similarity properties in the dynamics of delayed-feedback semiconductor lasers. *Physical Review A*, 89:023822, 2014.

[93] D. A. Arroyo-Almanza, A. N. Pisarchik, I. Fischer, C. R. Mirasso, and M. C. Soriano. Spectral properties and synchronization scenarios of two mutually delay-coupled semiconductor lasers. *Optics Commununications*, 301:67–73, 2013.

[94] R. Vicente, J. Daudén, P. Colet, R. Toral, et al. Analysis and characterization of the hyperchaos generated by a semiconductor laser subject to a delayed feedback loop. *IEEE Journal of Quantum Electronics*, 41:541–548, 2005.

[95] F. T. Arecchi, G. Giacomelli, A. Lapucci, and R. Meucci. Two-dimensional representation of a delayed dynamical system. *Physical Review A*, 45(7):R4225–R4228, 1992.

[96] D. W. Sukow, J. R. Gardner, and D. J. Gauthier. Statistics of power-dropout events in semiconductor lasers with time-delayed optical feedback. *Physical Review A*, 56:R3370–R3373, 1997.

[97] T. Heil, I. Fischer, W. Elsäßer, J. Mulet, and C. R Mirasso. Statistical properties of low-frequency fluctuations during single-mode operation in distributed-feedback lasers: experiments and modeling. *Optics Letters*, 24(18):1275–1277, 1999.

[98] Floris Takens. Detecting strange attractors in turbulence. In David Rand and Lai-Sang Young, editors, *Dynamical Systems and Turbulence, Warwick 1980*, volume 898 of *Lecture Notes in Mathematics*, pages 366–381. Springer Berlin Heidelberg, 1981.

[99] T. Sauer, J. A. Yorke, and M. Casdagli. Embedology. *Journal of Statistical Physics*, 65(3-4):579–616, 1991.

[100] V. Flunkert, O. D'Huys, J. Danckaert, I. Fischer, and E. Schöll. Bubbling in delay-coupled lasers. *Physical Review E*, 79:065201, 2009.

[101] R. Lang and K. Kobayashi. External optical feedback effects on semiconductor injection laser properties. *IEEE Journal of Quantum Electronics*, 16(3):347–355, 1980.

[102] B. W. Hakki and T. L. Paoli. Cw degradation at 300 k of GaAs double-heterostructure junction lasers. ii. electronic gain. *Journal of Applied Physics*, 44(9):4113–4119, 1973.

[103] D. W. Sukow and D. J. Gauthier. Entraining power-dropout events in an external-cavity semiconductor laser using weak modulation of the injection current. *IEEE Journal of Quantum Electronics*, 36(2):175–183, 2000.

[104] J. M. Buldú, J. García-Ojalvo, C. R. Mirasso, and M. C. Torrent. Stochastic entrainment of optical power dropouts. *Physical Review E*, 66(2):021106, 2002.

[105] F. Marino, M. Giudici, S. Barland, and S. Balle. Experimental evidence of stochastic resonance in an excitable optical system. *Physical Review Letters*, 88(4):040601, 2002.

[106] W.-S. Lam, P. N. Guzdar, and R. Roy. Effect of spontaneous emission noise and modulation on semiconductor lasers near threshold with optical feedback. *International Journal of Modern Physics B*, 17(22n24):4123–4138, 2003.

[107] T. Inagaki and T. Saito. Consistency in a chaotic spiking oscillator. *IEICE Transactions on Fundamentals of Electronics, Communications and Computer Sciences*, 91(8):2240–2243, 2008.

[108] S. Hata, T. Shimokawa, K. Arai, and H. Nakao. Synchronization of uncoupled oscillators by common gamma impulses: From phase locking to noise-induced synchronization. *Physical Review E*, 82(3):1–12, 2010.

[109] A. Aragoneses, T. Sorrentino, S. Perrone, D. J. Gauthier, M. C. Torrent, and C. Masoller. Experimental and numerical study of the symbolic dynamics of a modulated external-cavity semiconductor laser. *Optics Express*, 22(4):4705–4713, 2014.

[110] J. P. Toomey, D. M. Kane, M. W. Lee, and K. A. Shore. Nonlinear dynamics of semiconductor lasers with feedback and modulation. *Optics Express*, 18(16):16955–16972, 2010.

[111] Kunihiko Kaneko. Globally Coupled Chaos Violates the Law of Large Numbers but Not the Central-Limit Theorem. *Physical Review Letters*, 65(12):1391–1394, 1990.

[112] Sudeshna Sinha. Noisy Uncoupled Chaotic Map Ensembles Violate the Law of Large Numbers. *Physical Review Letters*, 69(23):3306–3309, 1992.

[113] W. Maass and C.M. Bishop. *Pulsed neural networks*. The MIT Press, Massachusetts, 2001.

[114] Toni Pérez and Atsushi Uchida. Reliability and synchronization in a delay-coupled neuronal network with synaptic plasticity. *Physical Review E*, 83(6):061915, June 2011.

[115] N. D. Haynes, M. C. Soriano, D. P. Rosin, I. Fischer, and D. J. Gauthier. Reservoir computing with a single time-delay autonomous boolean node. *Physical Review E*, 91(2):020801, 2015.

[116] K. Ikeda, K. Otsuka, and K. Matsumoto. Maxwell-bloch turbulence. *Progress of Theoretical Physics Supplement*, 99:295–324, 1989.

[117] B. Tromborg and J. Mørk. Nonlinear injection locking dynamics and the onset of coherence collapse in external cavity lasers. *IEEE Journal of Quantum Electronics*, 26(4):642–654, 1990.

[118] A. Hohl, H. J. C. Van der Linden, and R. Roy. Determinism and stochasticity of power-dropout events in semiconductor lasers with optical feedback. *Optics letters*, 20(23):2396–2398, 1995.

[119] A. Torcini, S. Barland, G. Giacomelli, and F. Marin. Low-frequency fluctuations in vertical cavity lasers: experiments versus lang-kobayashi dynamics. *Physical Review A*, 74(6):063801, 2006.

[120] A. Aragoneses, N. Rubido, J. Tiana-Alsina, M. C. Torrent, and C. Masoller. Distinguishing signatures of determinism and stochasticity in spiking complex systems. *Scientific Reports*, 3, 2013.

[121] K. Hicke, X. Porte, and I. Fischer. Characterizing the deterministic nature of individual power dropouts in semiconductor lasers subject to delayed feedback. *Physical Review E*, 88(5):052904, 2013.

[122] Konstantin Hicke. *Synchronization and application of delay-coupled semiconductor lasers*. PhD thesis, Universitat de les Illes Balears, 2014.

[123] L. Larger, J.-P. Goedgebuer, and F. Delorme. Optical encryption system using hyperchaos generated by an optoelectronic wavelength oscillator. *Physical Review E*, 57(6):6618, 1998.

[124] K. Ikeda. Multiple-valued stationary state and its instability of the transmitted light by a ring cavity system. *Optics Communications*, 30(2):257–261, 1979.

[125] A. Neyer and E. Voges. Dynamics of electrooptic bistable devices with delayed feedback. *IEEE Journal of Quantum Electronics*, 18(12):2009–2015, 1982.

[126] V. S. Udaltsov, L. Larger, J.-P. Goedgebuer, M. W. Lee, E. Genin, and W. T Rhodes. Bandpass chaotic dynamics of electronic oscillator operating with delayed nonlinear feedback. *IEEE Transactions on Circuits and Systems I: Fundamental Theory and Applications*, 49(7):1006–1009, 2002.

[127] Y. K. Chembo, P. Colet, L. Larger, and N. Gastaud. Chaotic breathers in delayed electro-optical systems. *Physical Review Letters*, 95(20):203903, 2005.

[128] L. Larger, J.-P. Goedgebuer, and V. Udaltsov. Ikeda-based nonlinear delayed dynamics for application to secure optical transmission systems using chaos. *Comptes Rendus Physique*, 5(6):669–681, 2004.

[129] L. Illing and D. J. Gauthier. Hopf bifurcations in time-delay systems with band-limited feedback. *Physica D: Nonlinear Phenomena*, 210(3):180–202, 2005.

[130] K. E. Callan, L. Illing, Z. Gao, D. J. Gauthier, and E. Schöll. Broadband chaos generated by an optoelectronic oscillator. *Physical Review Letters*, 104(11):113901, 2010.

[131] T. E. Murphy, A. B. Cohen, B. Ravoori, K. R. B. Schmitt, A. V. Setty, F. Sorrentino, C. R. S. Williams, E. Ott, and R. Roy. Complex dynamics and synchronization of

delayed-feedback nonlinear oscillators. *Philosophical Transactions of the Royal Society of London A: Mathematical, Physical and Engineering Sciences*, 368(1911):343–366, 2010.

[132] S. Heiligenthal, T. Jüngling, O. D'Huys, D. A. Arroyo-Almanza, M. C. Soriano, I. Fischer, I. Kanter, and W. Kinzel. Strong and weak chaos in networks of semiconductor lasers with time-delayed couplings. *Physical Review E*, 88:012902, 2013.

[133] G. Giacomelli, F. Marino, M. A. Zaks, and S. Yanchuk. Coarsening in a bistable system with long-delayed feedback. *Europhysics Letters*, 99(5):58005, 2012.

[134] M. Hermans, M.C. Soriano, J. Dambre, P. Bienstman, and I. Fischer. Photonic delay systems as machine learning implementations. *Journal of Machine Learning Research*, to appear, 2015.

[135] S. Ortín, M. C. Soriano, L. Pesquera, D. Brunner, D. San-Martín, I. Fischer, C. R. Mirasso, and J. M. Gutiérrez. A unified framework for reservoir computing and extreme learning machines based on a single time-delayed neuron. *Scientific Reports*, 5:14945, 2015.

[136] F. Heismann, S. K. Korotky, and J. J. Veselka. Lithium niobate integrated optics: Selected contemporary devices and system applications. *Optical Fiber Telecommunications III B*, pages 377–462, 1997.

[137] A. Boyer de la Giroday. *Chaotic semiconductor lasers for random number generation [Diploma Thesis]*. Université Libre de Bruxelles, 2007.

[138] T. E. Murphy and R. Roy. Chaotic lasers: The world's fastest dice. *Nature Photonics*, 2(12):714–715, 2008.

[139] A. Rukhin, J. Soto, J. Nechvatal, M. Smid, E. Barker, S. Leigh, M. Levenson, M. Vangel, D. Banks, A. Heckert, J. Dray, and S. Vo. A statistical test suite for random and pseudorandom number generators for cryptographic applications. *NIST Special Publication*, pages 800–22, Revision 1a, 2010.

[140] M. Matsumoto and T. Nishimura. Mersenne twister: a 623-dimensionally equidistributed uniform pseudo-random number generator. *ACM Transactions on Modeling and Computer Simulation (TOMACS)*, 8(1):3–30, 1998.

[141] J. F. Dynes, Z. L. Yuan, A. W. Sharpe, and A. J. Shields. A high speed, postprocessing free, quantum random number generator. *Applied Physics Letters*, 93:031109, 2008.

[142] A. R. Dixon, Z. L. Yuan, J. F. Dynes, A. W. Sharpe, and A. J. Shields. Gigahertz decoy quantum key distribution with 1Mbit/s secure key rate. *Optics Express*, 16(23):18790–19797, 2008.

[143] C. Gabriel, C. Wittman, D. Sych, R. Dong, W. Mauerer, U. L. Anderson, C. Marquardt, and G. Leuchs. A generator for unique quantum random numbers based on vacuum states. *Nature Photonics*, 4:711–715, 2010.

[144] M. Isida and H. Ikeda. Random number generator. *Annals of the Institute of Statistical Mathematics*, 8(1):119–126, 1956.

[145] C. R. S. Williams, J. C. Salevan, X. Li, R. Roy, and T. E. Murphy. Fast physical random number generator using amplified spontaneous emission. *Optics Express*, 18(23):23584–97, 2010.

[146] H. Guo, W. Tang, Y. Liu, and W. Wei. Truly random number generation based on measurement of phase noise of a laser. *Physical Review E*, 81:051137, 2010.

[147] X. Li, B. Cohen, T. E. Murphy, and R. Roy. Scalable parallel physical random number generator based on a superluminescent led. *Optics Letters*, 36:1020–1022, 2011.

[148] Apostolos Argyris, Evangelos Pikasis, Stavros Deligiannidis, and Dimitris Syvridis. Sub-tb/s physical random bit generators based on direct detection of amplified spontaneous emission signals. *Journal of Lightwave Technology*, 30(9):1329–1334, 2012.

[149] L. Li, A. Wang, P. Li, H. Xu, L. Wang, and Y. Wang. Random bit generator using delayed self-difference of filtered amplified spontaneous emission. *IEEE Photonics Journal*, 6(1), 2014.

[150] W. Timothy Holman, J. Alvin Connelly, and Ahmad B. Dowlatabadi. An integrated analog/digital random noise source. *IEEE Transactions on Circuits and Systems I: Fundamental Theory and Applications*, 44(6):521–528, 1997.

[151] G. M. Bernstein and M. A. Lieberman. Secure random number generation using chaotic circuits. *IEEE Transactions on Circuits and Systems*, 37(9):1157–1164, 1990.

[152] M. Sciamanna and K. A. Shore. Physics and applications of laser diode chaos. *Nature Photonics*, 9(3):151–162, 2015.

[153] Y. Akizawa, T. Yamazaki, A. Uchida, T. Harayama, S. Sunada, K. Arai, K. Yoshimura, and P. Davis. Fast random number generation with bandwidth-enhanced chaotic semiconductor lasers at 8 x 50 Gb/s. *IEEE Photonics Technology Letters*, 24(12):1042–1044, 2012.

[154] I. Reidler, Y. Aviad, M. Rosenbluh, and I. Kanter. Ultrahigh-speed random number generation based on a chaotic semiconductor laser. *Physical Review Letters*, 103:024102, 2009.

[155] R. M. Nguimdo, G. Verschaffelt, J. Danckaert, X. Leijtens, J. Bolk, and G. Van der Sande. Fast random bits generation based on a single chaotic semiconductor ring laser. *Optics Express*, 20(27):28603–28613, 2012.

[156] K. Hirano, T. Yamazaki, S. Morikatsu, H. Okumura, H. Aida, A. Uchida, S. Yoshimori, K. Yoshimura, T. Harayama, and P. Davis. Fast random bit generation with bandwidth-enhanced chaos in semiconductor lasers. *Optics Express*, 18(6):5512–5524, 2010.

[157] X.-Z. Li and S.-C. Chan. Random bit generation using an optically injected semiconductor laser in chaos with oversampling. *Optics Letters*, 37(11):2163–5, 2012.

[158] A. Argyris, S. Deligiannidis, E. Pikasis, A. Bogris, and D. Syvridis. Implementation of 140 Gb/s true random bit generator based on a chaotic photonic integrated circuit. *Optics Express*, 18(18):18763–18768, 2010.

[159] T. Harayama, S. Sunada, K.i Yoshimura, P. Davis, K. Tsuzuki, and A. Uchida. Fast nondeterministic random-bit generation using on-chip chaos lasers. *Physical Review A*, 83(3):031803, March 2011.

[160] R. Takahashi, Y. Akizawa, A. Uchida, T. Harayama, K. Tsuzuki, S. Sunada, K. Arai, K. Yoshimura, and P. Davis. Fast physical random bit generation with photonic integrated circuits with different external cavity lengths for chaos generation. *Optics Express*, 22(10):11727–11740, 2014.

[161] T. Heil, A. Uchida, P. Davis, and T. Aida. TE-TM dynamics in a semiconductor laser subject to polarization-rotated optical feedback. *Physical Review A*, 68:033811, 2003.

[162] N. Oliver, M. C. Soriano, D. W. Sukow, and I. Fischer. Dynamics of a semiconductor laser with polarization-rotated feedback and its utilization for random bit generation. *Optics Letters*, 36(23):4632–4634, 2011.

[163] M. C. Soriano, P. Colet, and C. R. Mirasso. Security implications of open-and closed-loop receivers in all-optical chaos-based communications. *IEEE Photonics Technology Letters*, 21(7):426–428, 2009.

[164] K. Otsuka and J-L. Chern. High-speed picosecond pulse generation in semiconductor lasers with incoherent optical feedback. *Optics Letters*, 16:1759–1761, 1991.

[165] X. Porte, O. D'Huys, T. Jüngling, D. Brunner, M. C. Soriano, and I. Fischer. Auto-correlation properties of chaotic delay dynamical systems: A study on semiconductor lasers. *Physical Review E*, 90:052911, 2014.

[166] C. Bracikowski, R. F. Fox, and R. Roy. Amplification of intrinsic noise in a chaotic multimode laser system. *Physical Review A*, 45(1):403, 1992.

[167] S. Sunada, T. Harayama, P. Davis, K. Tsuzuki, K.-I. Arai, K. Yoshimura, and A. Uchida. Noise amplification by chaotic dynamics in a delayed feedback laser system and its application to nondeterministic random bit generation. *Chaos*, 22(4):047513, 2012.

[168] I. Kanter, Y. Aviad, I. Reidler, E. Cohen, and M. Rosenbluh. An optical ultrafast random bit generator. *Nature Photonics*, 4:58–61, 2010.

[169] K. Hirano, K. Amano, A. Uchida, S. Naito, M. Inoue, S. Yoshimori, K. Yoshimura, and P. Davis. Characteristics of fast physical random bit generation using chaotic semiconductor lasers. *IEEE Journal of Quantum Electronics*, 45(11):1367–1379, 2009.

[170] H. Nyquist. Certain topics in telegraph transmission theory. *Transactions of the American Institute of Electrical Engineers*, 47:617644, 1928.

[171] C. E. Shannon. Communication in the presence of noise. *Proceedings of the Institute of Radio Engineers*, 37:10–21, 1949.

[172] H. Li, A. Hohl, A. Gavrielides, H. Hou, and K. D. Choquette. Stable polarization self-modulation in vertical-cavity surface-emitting lasers. *Applied Physics Letters*, 72(19):2355–2357, 1998.

[173] L. Khaykovich, T. Galfsky, Z. Shotan, and N. Gross. Te-tm coupled mode dynamics in a semiconductor laser subject to feedback with variably rotated polarization. *Optics Communications*, 282(10):2059–2061, 2009.

[174] J. Zhang, Y. Wang, M. Liu, L. Xue, P. Li, A. Wang, and M. Zhang. A robust random number generator based on differential comparison of chaotic laser signals. *Optics Express*, 20(7):7496–7506, 2012.

[175] Georges Marsaglia. Diehard: A battery of tests of randomness (1996). *See http://stat. fsu. edu/˜geo/diehard. html.*

[176] John Walker. Ent: A pseudorandom number sequence test program. *Software and documentation available at/www.fourmilab.ch/random/S*, 2008.

[177] K. Yoshimura, J. Muramatsu, P. Davis, T. Harayama, H. Okumura, S. Morikatsu, H. Aida, and A. Uchida. Secure key distribution using correlated randomness in lasers driven by common random light. *Physical Review Letters*, 108:070602, 2012.

[178] N. Gisin, G. Ribordy, W.Tittel, and H. Zbinden. Quantum cryptography. *Review of Modern Physics*, 74:145–195, Mar 2002.

[179] B. Sanguinetti, A. Martin, H. Zbinden, and N. Gisin. Quantum random number generation on a mobile phone. *Physical Review X*, 4:031056, Sep 2014.